Monitoring civil infrastructure using satellite radar interferometry

Ling Chang

Monitoring civil infrastructure using satellite radar interferometry

Proefschrift

ter verkrijging van de graad van doctor
aan de Technische Universiteit Delft,
op gezag van de Rector Magnificus prof. ir. K.C.A.M. Luyben,
voorzitter van het College voor Promoties,
in het openbaar te verdedigen op woensdag 01 Juli 2015 om 10:00 uur

door

Ling Chang

Master of Engineering in Geodesy and Survey Engineering, Tongji University
geboren te Jinzhong, Shanxi, China.

Dit proefschrift is goedgekeurd door de promotor:

Prof. dr. ir. R.F. Hanssen

Samenstelling promotiecommissie:

Rector Magnificus,	voorzitter
Prof. dr. ir. R.F. Hanssen,	Technische Universiteit Delft, promotor
Prof .dr. ir. R.P.B.J. Dollevoet,	Technische Universiteit Delft
Prof. dr. ir. D.A. Hordijk,	Technische Universiteit Delft
Prof. dr .ir. P.J.M. van Oosterom,	Technische Universiteit Delft
Prof. Dr.-Ing. W. Niemeier,	Technische Universität Braunschweig, Germany
Dr. D. Geudtner,	European Space Agency
Dr. ir. C.C.J.M. Tiberius,	Technische Universiteit Delft

Ling Chang
Monitoring Civil Infrastructure using Satellite Radar Interferometry

Department of Geoscience and Remote Sensing
Delft University of Technology

Keywords: Satellite Radar Interferometry, Infrastructure, Kinematic Time Series Modeling

ISBN 978-94-6186-489-5

Type set by the author with the LaTeX Documentation System
Printed by Optima Grafische Communicatie, the Netherlands

An electronic version of this dissertation is available at
http://repository.tudelft.nl/.

To mum

謹以此書獻給我最親愛的母親

Contents

Acknowledgement

Without the help and support from many people, this thesis would not have been possible. I would like to thank everybody who supported me, but there are a few people I would like to thank especially.

First and foremost I would like to express my sincere gratitude to my promotor and advisor Ramon Hanssen for his tireless guidance and scientific support. I have benefited from his valuable advice. I am also grateful to Andy Hooper for sharing the details of his StaMPS software. He was really kind to discuss the research with me and always gave me valuable suggestions and constructive comments.

I have learned a lot from inspiring discussions with Shizhuo Liu, a scientist whom I appreciate highly for his earnestness and modesty. I really appreciate it that he encouraged me to pursue my PhD study. He and his wife Sijia Rong helped me to get used to life in Delft and invited me to celebrate Christmas and Spring Festival. I acknowledge Miguel Caro Cuenca, Freek van Leijen and Sami Samiei-Esfahany, who were all like a detailed answer sheet related to radar interferometric techniques and shared all their knowledge selflessly. Whenever I had questions for them, they would not hesitate to answer to me. Thanks also to Junchao Shi, Yanqing Hou, Jiangjun Ran and Jinhu Wang, I appreciate that they gave me many useful suggestions on my work. I am also glad that I could share my ideas with them.

I count myself lucky to have had the opportunity to work in our radar group. I enjoyed a very joyful working environment with the positive influence and encouragement from my other colleagues Joana Esteves Martins, Prabu Dheenathayalan, Mahmut Arikan, Manu Delgado Blasco, Qiang Wang, Anneleen Oyen, Pooja Mahapatra, Lorenzo Iannini, Ramses Molijn (Ramses also helped me with the Dutch translation) and Ali Mousivand. Their comments and feedback on my work, computer support, and script sharing were very valuable to me, and they helped me to understand more about European-Asian cultures in general. Peter Teunissen helped me 'remotely' on the stochastic model for arc phase, and Christian Tiberius, Sandra Verhagen and Hans van der Marel were instrumental through their probability and statistics course.

All members of the doctoral committee, Rolf Dollevoet, Dick Hordijk, Peter van Oosterom, Wolfgang Niemeier, Dirk Geudtner and Christian Tiberius, provided valuable reviews on my thesis.

My MSc supervisor Jicang Wu at Tongji university guided me to this challenging 'radar interferometry road', and I am grateful to keep on collaborating with my colleagues Lei Zhang at Hongkong Polytechnic University, and Mi Jiang at Hohai University.

With this opportunity, I would like to thank the China Scholarship Council (CSC) for providing the four-year funding for my PhD study. Under this financial support, I could totally fling myself into this PhD study. I would also like to thank the Dragon cooperation programme between ESA and the Ministry of Science and Technology of China, to allow me to have the opportunities for academic exchange with both Euro-

pean and Chinese scientists. Within the Dragon framework, I acknowledge Tao Li from Wuhan University, Jingfa Zhang from the Institute of Crustal Dynamics, Xiaoli Ding from Hongkong Polytechnic University, and Zhenhong Li from Newcastle University.

Finally, I would like to express my sincerest gratitude to my mother, for her early guidance and later support. Her understanding and constant encouragement are my spiritual pillars that I can always rely on. I am happy that we made the cover of this thesis together.

Ling Chang
Delft, May 2015

Summary

Satellite radar interferometry (InSAR) is a precise and efficient technique to monitor deformation on Earth with millimeter precision. Most InSAR applications focus on geophysical phenomena, such as earthquakes, volcanoes, or subsidence. Monitoring civil infrastructure with InSAR is relatively new, with potential for operational applications, but currently not exploited to full advantage. Here we investigate how to optimally assess and monitor the structural health of civil infrastructure using InSAR, and develop methodology to improve its capability for operational monitoring.

InSAR kinematic time series analysis involves the processing of extremely large datasets to estimate the relative movements of points on the infrastructure. The estimated movements may expose strain in the structure, potentially revealing structural health problems. However, the optimal mathematical model relating the satellite observations to the kinematic parameters of interest is unknown. We propose multiple hypothesis testing as a means to identify the most probable mathematical model. For each target, the null-hypothesis of 'steady-state' motion is considered as default, which is tested against a multitude of potential temporal models, built based on a library of canonical functions. If the null hypothesis is sustained, there is no (significant) anomaly in the data. If the null hypothesis is rejected, we test the entire library of potential alternative models with different physically realistic parameters against the null hypothesis using the B-method of testing. Finally, using test-ratios, we select the most likely model for each target, update the quality description of the estimates, while avoiding overfitting.

InSAR processing strategies are designed and implemented for structural health assessment of railway infrastructure and buildings. The Qinghai-Tibet railway, at 5000 m altitude, is suspected to be affected by dynamic changes in permafrost environments. Using medium resolution SAR data, we apply an 'all-pixel' approach based on statistical similarity to tackle geometric decorrelation and maximize the density of InSAR measurement points over the track. Seasonal changes in deformation are detected, most likely due to freezing and thawing of the permafrost's active layer. To explore the capability of railway infrastructure monitoring using multi-track high-resolution SAR data, we estimate the 3D temporal behavior of the Betuwe railway, the Netherlands, in a track-fixed reference system in the transversal, longitudinal, and normal direction using 248 TerraSAR-X images acquired from ascending and descending orbits. For building monitoring, we study a shopping mall in Heerlen, the Netherlands. Due to a developing sinkhole below, the building lost its structural support, leading to a sudden evacuation and a near-collapse. Using consecutive InSAR data time series acquired by four different SAR satellites between 1992 and 2011, we find significant precursory motion. We integrate these InSAR data time series and improve the precision of geolocation of the InSAR measurement points using additional lidar-based data. The detected localized strain appears to be related to an upward migrating cavity. The analysis demonstrates the feasibility of an early detection of anomalous processes

in the underground.

This study reveals the high potential of structural health monitoring using observations from satellites, either for forensic analysis—investigating the behavior of a structure after a failure manifested itself—or for preventive monitoring—to identify anomalies in behavior that may be indicative for impending structural failure.

Samenvatting

Satelliet radar interferometrie (InSAR) wordt gebruikt voor het monitoren van deformaties op aarde, met millimeter precisie. De meeste toepassingen concentreren zich op geofysische verschijnselen, zoals aardbevingen, vulkanen, of bodemdaling. Het monitoren van civiele infrastructuur met InSAR heeft een grote potentie, maar deze wordt nog nauwelijks operationeel benut. In deze studie onderzoeken we hoe informatie over de status van constructies (*structural health*) kan worden verzameld met behulp van InSAR, en ontwikkelen we een methodologie om haar monitoringscapabiliteit significant te verbeteren.

Kinematische tijdsreeksanalyse met InSAR behelst het verwerken van extreem grote datasets om de relatieve bewegingen van (punten op) infrastructuur te schatten. Deze bewegingen kunnen het gevolg zijn van spanningen in de constructie en daarmee mogelijk constructie-technische problemen aan het licht brengen. Echter, het mathematische model, dat de satellietwaarnemingen relateert aan de specifieke kinematische parameters, is onbekend. Om het meest waarschijnlijke model te bepalen gebruiken we het 'meervoudig toetsen van hypotheses'. Voor elk punt hanteren we de nulhypothese 'eenparige beweging', welke wordt getoetst tegen een groot aantal alternatieve kinematische modellen, geconstrueerd op basis van een verzameling van kernfuncties. Wanneer de nulhypothese wordt verworpen testen we de gehele collectie van potentiële alternatieve modellen met verschillende fysisch-realistische parameters tegen de nulhypothese, waarbij gebruik wordt gemaakt van de B-methode van toetsen. Gebruikmakend van toets-quotiënten, selecteren we hierdoor (i) het meest waarschijnlijke model voor elk punt, en verbeteren we (ii) de kwaliteitsbeschrijving van de schattingen, terwijl we onrealistische *overfitting* van het model vermijden.

De ontwikkelde InSAR verwerkingsstrategieën zijn toegepast in drie case-studies om informatie over de *structural health* van rail-infrastructuur en gebouwen te verkrijgen. Voor de 5000 m hoge Qinghai-Tibet spoorweg bestond het vermoeden dat deze onderhevig kon zijn aan dynamische veranderingen door de onderliggende permafrost. Met behulp van SAR data met middelhoge resolutie passen we een '*all-pixel*' benadering toe, gebaseerd op statistische eenduidigheid, om geometrische decorrelatie te verminderen en de dichtheid van de InSAR meetpunten op het spoor te maximaliseren. Hieruit bevestigen we seizoensgebonden deformatie, waarschijnlijk door het bevriezen en ontdooien van de actieve laag van de permafrost. Daarnaast bestuderen we de monitoringscapabiliteit voor complexe rail-infra (Betuweroute) met 248 hoge-resolutie SAR beelden vanuit dalende en klimmende satellietbanen. We schatten hieruit 3D deformaties op millimeter-niveau in een spoor-vast referentiesysteem, en beschrijven de haalbare precisie en betrouwbaarheid. Tot slot analyseren we spanningen in gebouwen bij winkelcentrum *'t Loon* in Heerlen. Dit gebouw verloor haar stabiliteit en moest plotseling werden ontruimd, naar later bleek door een zich ontwikkelend *sinkhole* eronder. Gebruikmakend van opeenvolgende InSAR tijdreeksen van vier verschillende satellieten tussen 1992 en 2011 zien we substantiële beweging

voorafgaand aan deze gebeurtenis. De gedetecteerde lokale spanning lijkt gerelateerd te zijn aan een opwaarts migrerende holte. Hieruit blijkt dat vroegtijdige detectie van processen in de ondergrond in principe mogelijk is met InSAR.

De ontwikkelde methodes in deze studie vergroten de potentie voor *structural health assessment* door het monitoren van infrastructuur met behulp van satellietobservaties, zowel voor forensische analyse (onderzoek naar het gedrag van een constructie nadat zich een calamiteit heeft voorgedaan) als voor preventieve controle (het vroegtijdig detecteren van dynamische afwijkingen in een constructie ter voorkoming van een calamiteit).

List of Publications

The following publications are related to this thesis:

Peer-reviewed journals

Chang, L. and Hanssen, R.F. (2014). Detection of cavity migration and sinkhole risk using radar interferometric time series. *Remote Sensing of Environment*, 147:56–64.

Chang, L., Dollevoet, R.P.B.J., and Hanssen, R.F. (2014). Railway infrastructure monitoring using satellite radar data. *International Journal of Railway Technology*, volume 2.

Chang, L. and Hanssen, R.F. (2015). Detection of permafrost sensitivity of the Qinghai–Tibet railway using satellite radar interferometry. *International Journal of Remote Sensing*, 36(3):691–700.

Chang, L. and Hanssen, R.F. (2015). A probabilistic approach to InSAR time series postprocessing. *IEEE Transactions on Geoscience and Remote Sensing*, in review.

Jiang, M., Ding, X., Hanssen, R.F., Malhotra, R. and Chang, L. (2015). Fast statistically homogeneous pixel selection for covariance matrix estimation for multitemporal InSAR. *IEEE Transactions on Geoscience and Remote Sensing*, 53(3): 1213-1224.

Conference proceedings

Chang, L. and Hanssen, R.F. (2011). Near real-time deformation monitoring based on Persistent Scatterer Interferometry. *Proceedings of ESA FRINGE 2011 Workshop*, Frascati, Italy, September 2011.

Chang, L. and Hanssen, R.F. (2012). Near real-time, semi-recursive, deformation monitoring of infrastructure using satellite radar interferometry. *Proceedings of 2012 IEEE International Geoscience and Remote Sensing Symposium (IGARSS)*, 1876-1879, Munich, Germany, July 2012.

Chang, L., Dheenathayalan, P. and Hanssen R.F. (2013). Precise geolocation of persistent scatterers aided and validated by a lidar DSM. *Proceedings of ESA Living Planet Symposium 2013*, Edinburgh, UK, September 2013.

Chang, L., Dollevoet, R.P.B.J., and Hanssen, R.F. (2014). Satellite monitoring of railway infrastructure. *Proceedings of the Second International Conference on Railway Technology: Research, Development and Maintenance*, Ajaccio, Corsica, France, April 2014.

Shi, J. and Chang, L. (2011) Surface deformation of Alpine terrain derived by PSInSAR technique on the Slachen glacier. *Proceedings of ESA FRINGE 2011 Workshop*, Frascati, Italy, September 2011.

OTHER

Conference abstracts and presentations

Chang, L. and Hanssen, R.F. (2011). Near real-time, semi-recursive deformation monitoring of infrastructure using satellite radar interferometry. *The Joint International Symposium on Deformation Monitoring*, Hong Kong, November 2011.

Chang, L. and Hanssen, R.F. (2012). Detection of cavity migration risks using radar interferometric time series. *American Geophysical Union (AGU), Fall Meeting*, San Francisco, December 2012.

Chang, L. and Hanssen, R.F. (2013). Deformation monitoring of the Qinghai-Tibet railway in relation to permafrost. *The 2013 Dragon Symposium*, Palermo, Sicily, Italy, May 2013.

Chang, L. and Hanssen, R.F. (2014). InSAR deformation modeling using test ratios and the B-method of testing. *The 2014 Dragon Symposium*, Chengdu, P.R. China, May 2014.

Chang, L. and Hanssen, R.F. (2015). A probabilistic approach for InSAR time series post-processing. *ESA FRINGE 2015 Workshop*, Frascati, Italy, March 2015.

Outreach

ter Voorde, M. (2011). Waarom verzakte winkelcentrum *'t Loon*?, Kennislink, web publication.

van Velden, F. (2011). Verzakking *'t Loon* blijkt omvangrijker, Cobauw, `http://www.cobouw.nl/nieuws/algemeen/2011/12/06/verzakking-t-loon-blijkt-omvangrijker`.

Television broadcast, Sinkhole risico's, Studio Max Live, 02 April 2013.

Television broadcast, Labyrint: Nederland van Onderen, 01 February 2012, `https://www.youtube.com/watch?v=m55ZjmtO6X0`.

Heinsman, E., Bodemverzakkingen in Limburg blootgelegd door nieuwe satelliet, De Kennis van Nu, Television Broadcast, 06 April 2014.

Nomenclature

List of acronyms

AHN	Actual Height data of Netherlands
ALOS	Advanced Land Observing Satellite
ASAR	Advanced Synthetic Aperture Radar
ASTER	Advanced Spaceborne Thermal Emission and Reflection Radiometer
BLUE	Best Linear Unbiased Estimation
BLUP	Best Linear Unbiased Prediction
COSMO-SkyMed	Constellation of small Satellites for the Mediterranean basin Observation
DEM	Digital Elevation Model
DEOS	Delft institute for Earth Observation and Space Systems
DePSI	Delft implementation of Persistent Scatterer Interferometry
DIA	Detection, Identification and Adaption
DInSAR	Differential Interferometric SAR
DLR	German Aerospace Center
DORIS	Delft Object-oriented Radar Interferometric Software
DS	Distributed Scatterer
Envisat	Environmental Satellite
ERS	European Remote-Sensing Satellite
ESA	European Space Agency
FFT	Fast Fourier Transform
GPS	Global Positioning System
LiDAR	Light Detection And Ranging
LOS	Line-Of-Sight
LSE	Least Squares Estimation
MDV	Minimally Detectable Value
MDB	Minimal Detectable Bias
MHT	Multiple Hypotheses Testing
NRT	Near Real-Time
OMT	Overall Model Test
PDF/pdf	Probability Density Function
PS	Persistent Scatterer
PSI	Persistent Scatterer Interferometry
Radar	Radio Detection And Ranging
Radarsat	Canada's Radar Earth Observation Satellite
RAR	Real Aperture Radar
RCS	Radar Cross Section
RMSE	Root Mean Squared Error
SAR	Synthetic Aperture Radar
SHM	Structural Health Monitoring
SLC	Single Look Complex

SNAPHU	Statistical cost, Network flow Algorithm for Phase Unwrapping
SNR	Signal to Noise Ratio
SRTM	Shuttle Radar Topography Mission
STC	Spatial-Temporal Consistency
SYM	Symmetry
StaMPS	Stanford Method for Persistent Scatterers
VCE	Variance Component Estimation
TerraSAR-X	German Radar Earth Observation Satellite
3D	Three-Dimensional

List of symbols

cm	centimeter
dB	decibel
km	kilometer
m	meter
rad	radians
y	year

a	phase ambiguity
A	design matrix; amplitude
B	baseline
$B_\perp$	perpendicular baseline
$B_{\perp,c}$	critical perpendicular baseline
B_t	temporal baseline
C	specification matrix of alternative hypothesis
$D\{.\}$	dispersion
D_a	amplitude dispersion index
$\exp\{.\}$	exponential function
$E\{.\}$	expectation
H	height
$\mathbb{H}$	criterion matrix
H_0	null hypothesis
H_a	alternative hypothesis for binary hypothesis testing
H_j	alternative hypothesis for multiple hypotheses testing
H_{sat}	elevation of satellite
I	identity matrix
$\text{Im}\{.\}$	imaginary part
j	imaginary unit; number of alternative hypothesis
K	kelvin; number of interferograms; critical value
m	number of observations
$\max\{.\}$	maximum operator
n	number of unknowns
$P(.)$	probability density function
$P_A^\perp$	orthogonal projector
Q_{yy}	covariance matrix of observations

$\mathrm{Re}\{.\}$	real part
R_g	ground resolution
R_{yy}	cofactor matrix of observations
T	satellite repeat cycle
$\underline{T}_q$	test statistic of dimension q
$\underline{\mathbf{T}}_q$	test statistic ratio of dimension q
$W\{.\}$	wrapping operator
v	velocity
x	unknown parameters
$\underline{y}$	observations
$\underline{z}$	complex number
$\mathcal{Z}$	set of integers
$\{.\}^{-1}$	inversion
$\{.\}^{T}$	transposition
$\hat{.}$	estimated value
$\tilde{.}$	predicted value

α	level of significance
η	temperature related parameter
β	level of false rejection of null hypothesis; height-to-phase conversion factor
δ_{ij}	Kronecker delta function of two integer variables i and j
ΔT	temperature difference
$\chi^2(q,\lambda)$	χ^2-distribution with dimension q and noncentrality parameter λ
$\underline{\hat{e}}$	estimated error
γ	coherence; power of test
γ_s	the azimuth of the track
γ_t	temporal correlation; the cant of the track
Γ	success rate of the decision
κ	exponential magnitude
λ	radar wavelength; noncentraility parameter
∇	vector of model imperfections
ψ	SLC phase
ϕ	interferometric phase
$\phi^k_{p,q}$	arc phase between point p and q in interferogram k
ϕ^k_p	wrapped interferometric phase of point p in interferogram k
ϕ_{atmo}	atmospheric phase
ϕ_{defo}	deformation phase
ϕ_{noise}	phase noise
ϕ_{orb}	orbital phase
ϕ_{scat}	scattering phase
ϕ_{topo}	topographic phase
ϕ^w	wrapped phase
ρ	slant range between ground target and satellite
σ	standard deviation

θ	look angle
θ_{inc}	incidence angle
ϖ	linear expansion coefficient

1
Introduction

1.1. Motivation

Monitoring civil infrastructure using satellite radar technology is feasible, but currently not exploited to full advantage. In this work, we develop and demonstrate methodology to improve its applicability for operational infrastructure monitoring.

1.2. Background

Civil infrastructure, such as buildings, railways, roads, bridges, dikes, dams, pipelines and quays, forms the backbone of urbanized societies and is critical for sustainable economic growth. Structural stability, or health, of civil infrastructure is therefore of vital importance in modern life. Not only can failure of critical infrastructure lead to human casualties and direct economic damage, it can also lead to ecological disasters and be disruptive for societies at large. Clear examples include flooding disasters due to failing water defense infrastructure, e.g. Wilnis peat dike (van Baars, 2005), New Orleans (Kates et al., 2006) and the Elbe river (Kreibich et al., 2005), disasters due to failure of high-speed railway infrastructure, such as the 1998 crash of the Eschede high-speed train in Germany (Milne et al., 2003), or the recent collapses of inferior factory buildings in Bangladesh (Manik et al., 2013).

Natural hazards, inferior construction, or bad foundation of structures are potential causes of failure, see Fig. 1.1. However, an even more prominent problem in today's developed society is *aging* (Chang et al., 2003). Civil infrastructure begins to deteriorate once it is built and used, and most structures in the western world were built between 1950 and 1975. Therefore, they have now reached a critical age. The accompanied degradation decreases the reliability of the infrastructure. In 2013, the American Society of Civil Engineers reported that a large portion of America's infrastructure exhibits significant deterioration, and that the infrastructure condition and capacity are of great concern, with a significant risk of failure. The investment required to solve these problems amounts up to 3.6 trillion USD by 2020 (ASCE, 2014). Only for dams, 262 million USD was spent on rehabilitation for 150 dams in 26 states in 2014 (Kohler, 2014). Similarly, in China, Europe, India, and many other countries, civil infrastructure in-service is deteriorating fast, or even defective already.

Consequently, there is a vital need for systematic monitoring of structural safety. Particularly, this involves the fast detection of first indications of structural health problems, such as strain or deformation, and the consecutive monitoring of such anomalies. This facilitates precautionary measures, timely warnings and effective mitigation systems to minimize economic loss and casualties.

1

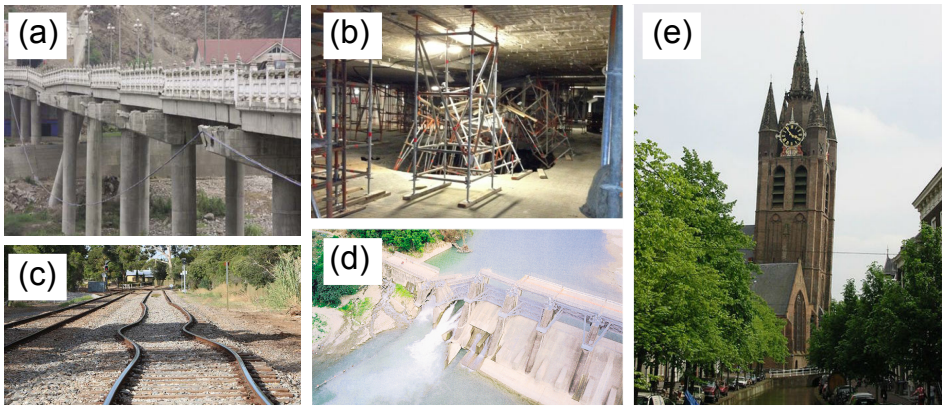

Figure 1.1: (a) A bridge in Beichuan County, China, damaged by the 2008 Wenchuan earthquake (Wang, 2008). (b) The 2011 collapse-sinkhole at the shopping mall *'t Loon* caused by subsurface cavity migration. (c) The buckling rail lines in Australia due to extreme heat (telegraph.co.uk). (d) The Shigan dam damaged by the 1999 Chi-Chi, Taiwan, earthquake (Shin and Teng, 2001). (e) The tilting Old Church of Delft, the Netherlands, susceptible to groundwater variation and aging.

Conventional methods for structural monitoring of civil infrastructure use in-situ measurement devices, such as strain gauges (Choi et al., 2008), accelerometers (Lima et al., 2008), laser interferometers (Nassif et al., 2005), electronic distance measurement instruments and GPS technology (Lovse et al., 1995; Lepadatu and Tiberius, 2014). However, these methods are costly, sometimes weather dependent (Cheng et al., 2002), and can only be applied on a limited scale, either in space or time. Moreover, they are usually only used at locations where structural deformation is expected, requiring a-priori knowledge that may not be available everywhere. To complement these conventional methods, we propose a spaceborne approach using Synthetic Aperture Radar Interferometry (InSAR), which we will refer to in the sequel as radar interferometry to be concise.

InSAR is a powerful technique which can remotely measure sub-centimeter-scale deformation over spans of days to years based on satellite SAR data analysis. A typical SAR intensity map represents the radar reflectivity of the imaged area. The strength of the returned radar echoes is strongly related to physical (i.e., surface roughness and slope) and electrical (i.e., dielectric constant, absorption) characteristics of the surface. Since Goldstein et al. (1988) used the phase information of SAR data in a first application of interferometry using a spaceborne platform (the SEASAT mission in a 3-day repeat-pass mode), the InSAR technique has matured through a series of Earth monitoring satellites. The launch of the ERS-1 satellite (European Space Agency, ESA) in 1991 is the starting point for this epoch, overlapped by JERS-1 (Japan Aerospace Exploration Agency, JAXA) in 1992, ERS-2 (ESA) and Radarsat-1 (Canadian Space Agency, CSA) in 1995, Envisat (ESA) in 2002, ALOS-1 (JAXA) in 2006, and now followed by Radarsat-2 (2007, Canadian Space Agency, CSA), four COSMO-SkyMed satellites

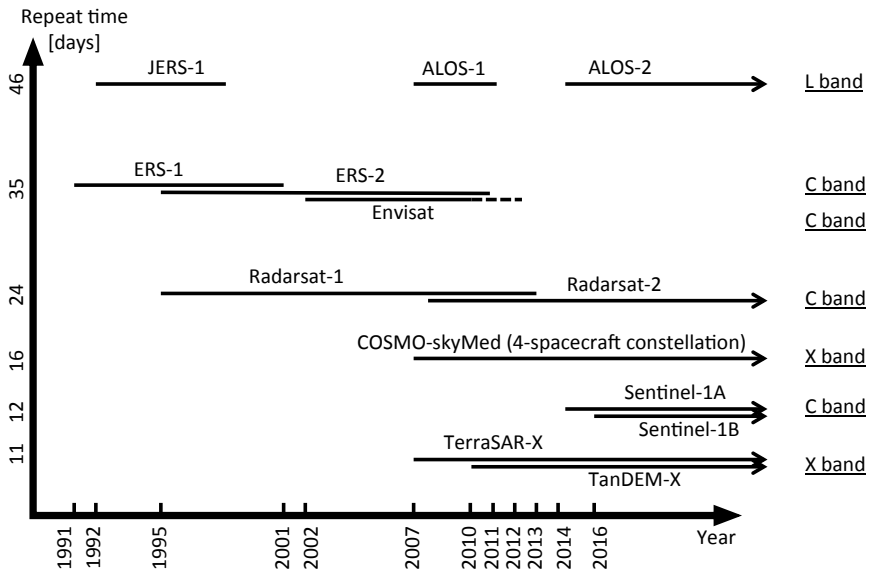

Figure 1.2: Radar satellite missions with their launch dates and key design parameters: wavelength, resolution and satellite repeat period. The dashed line for Envisat indicates the time period when it was not interferometrically usable anymore and eventually lost contact.

(2007, Italian Space Agency, ASI), TerraSAR-X (2007, German Aerospace Center, DLR), TanDEM-X (2010, DLR), ALOS-2 (2014, JAXA), Sentinel-1A (2014, ESA) and Sentinel-1B (2016, ESA), see Fig. 1.2. These satellites deliver SAR images with a repeat interval ranging from one day to more than one month, and have been widely applied in monitoring 'natural' geophysical processes such as glacier movements (Mohr and Madsen, 1996), earthquakes (Massonnet et al., 1993; Hanssen et al., 2000; Feigl et al., 2002; Ćakir et al., 2003; Fielding et al., 2013), volcanoes (Massonnet et al., 1995; Amelung et al., 2000; Stevens et al., 2001; Usai et al., 2003; Hooper et al., 2004; Sigmundsson et al., 2010; Takada and Fukushima, 2013), and subsidence (Amelung et al., 1999; Ketelaar, 2004; Sousa et al., 2008; Caro Cuenca and Hanssen, 2008; Caro Cuenca et al., 2013). Yet, only lately they have been successfully deployed for structural health monitoring of infrastructure, especially in the urban environment (Arikan and Hanssen, 2008; Chen et al., 2012; Chang and Hanssen, 2011, 2014; Chang et al., 2014).

In the past two decades, diverse InSAR data processing methods have been developed for three-dimensional terrain height estimation (DEM generation) and mapping of surface deformation. The conventional method estimates the elevation or deformation using two SAR images (Bamler and Hartl, 1998; Massonnet and Feigl, 1998). Using this method, the measurement quality can be significantly degraded by temporal and spatial decorrelation (Bamler and Hanssen, 1997; Ferretti et al., 1999b; Ciuc et al., 2002) and atmospheric disturbances (Hanssen, 2001). Moreover, phase unwrap-

ping (the estimation of the 2π-ambiguities in the phase measurements) becomes more difficult with decreasing coherence (that is the decrease in the degree of correlation between two SAR images) (Eineder and Holzner, 1999; van Leijen et al., 2006; Kampes and Adam, 2006). Following the conventional two-pass InSAR method, advanced methods wherein (i) the errors are estimated and removed, (ii) all coherent points are recognized and used for spatial and temporal unwrapping, and (iii) the deformation histories of all coherent points are archived, were proposed. These so-called *multi-epoch methods* use a stack of radar images which is analyzed to identify all temporally coherent points by using an optimal image combination that is capable of utilizing all archived images over a certain study area. Then the long-term deformation time series of those coherent points are estimated. These multi-epoch methods are classified in terms of the image combinations (such as a *single master* image network and the temporal *daisy chain* network) or in terms of the types of scatterers (i.e. persistent scatterers and distributed scatterers). Multi-epoch methods include persistent scatterer interferometry (PSI) (Ferretti et al., 1999a), small baseline permanent scatterers (SBAS) (Berardino et al., 2002; Mora et al., 2002; Lanari, 2003; Tizzani et al., 2007; Lanari et al., 2010) and SqueeSAR (Ferretti et al., 2011). Yet, to primarily concentrate on an efficient and systematic methodology for monitoring civil infrastructure and detecting anomalies both in space and time, for an enormous amount of targets, all InSAR methods are considered to be potentially useful.

1.3. Problem statement

For effective civil infrastructure monitoring, InSAR methods should have some specific capabilities. First, it is necessary to be able to detect unusual changes in the spatio-temporal behavior of infrastructure, as these could be indicative for potential structural failure or weakening. If such anomalies are detected, the method needs to assess when and where this change happens, accompanied by proper quality metrics, such as precision and reliability. Then, this information can be linked to the possible driving mechanisms. There is currently no standard methodology to reach these objectives.

In general, the InSAR observations include the contributions of relative positions of the scatterers, deformation (kinematic time series), atmosphere and noise, which can be parameterized based on assumptions on their expected behavior over time or in space. Examples include assumptions of spatial smoothness of the atmospheric signal, or temporal smoothness of the deformation signal. Although there are several classes of problems where some of these assumptions seem to be applicable, as successfully reported for many InSAR applications (Hooper, 2006; van Leijen and Hanssen, 2007; Tizzani et al., 2007; Perski et al., 2008; Hanssen and van Leijen, 2008; Hooper, 2008; Lanari et al., 2010; Lagios et al., 2013), in its origin the dependency on such assumptions makes the techniques sub-optimal. For instance, the kinematic component is often parameterized as a linear function of time, which may be sufficient to facilitate phase unwrapping efficiently (Teunissen, 2006, 2003; Caro Cuenca, 2012), but it is hardly always the case for every single point since no single assumption will satisfy all points. Moreover, this strategy does not exploit the extremely rich information content in the data in an optimal and efficient way.

Considering the intrinsic uncertainty in resolving the 2π phase ambiguities, the

mathematical estimation of the InSAR parameters is essentially an ill-posed problem. It requires the inversion of a system of non-linear equation, where every new observation introduces at least three additional unknowns. There is no unique solution, and therefore the obtained solution is dependent on the assumptions mentioned above. Furthermore, noise in the data, or a single missing data point, may lead to deviations in the estimated phase ambiguities, which may subsequently cause significant changes in the estimated kinematic parameters. Finally, different processing methodologies, or different settings/parameterizations in the estimation procedure, may lead to different results. In terms of achieving public acceptance of InSAR as a viable and reliable geodetic technique, such problems in the repeatability or reliability of the results are of concern, especially in critical conditions affecting public safety. Thus, there is a strong need to homogenize and standardize geodetic InSAR data processing.

1.4. Research objectives

Given the recent developments in InSAR and the aforementioned problems, we can state that the monitoring of civil infrastructure with InSAR is feasible, but currently not exploited to full advantage. In this work, our objective is to develop and demonstrate methodology to improve the capability for operational infrastructure monitoring. The main research question is:

How to optimally assess and monitor structural health of civil infrastructure using satellite radar interferometry?

To address this main challenge, four specific research questions are considered.

1. *How to design the optimal functional and stochastic model?*

   This first research question focuses on the parameterization of kinematic time series for every single InSAR measurement point. The functional model refers to the (linearized) relationship between the InSAR measurements (including kinematic time series) and the unknown parameters. The stochastic model expressed in the (co)variance structure describes the precision of the InSAR measurements. To design the optimal functional and stochastic model, we use the Gauss-Markov model to describe the functional and stochastic relations (Gauss, 1809; Koch, 1999). The research question is aimed at finding a generic approach to find the most probable model description.

2. *How to detect spatio-temporal anomalies efficiently and precisely?*

   When the optimal functional and stochastic model for all points are well-designed, we should detect spatio-temporal anomalies with a predefined probability of detection.

3. *How to optimize InSAR data processing to monitor civil infrastructure?*

   The kinematic time series are estimated by InSAR data processing. To compute the precise estimates (displacements) for the kinematic time series, we should improve current InSAR data processing. We will specifically aim at (i) reducing the noise due to geometric decorrelation for distributed targets; (ii) decomposing

the satellite line-of-sight deformation measurements to a local Cartesian coordinate system, analyzing how observational errors propagate into the estimates, and detecting spatio-temporal changes in geometry; (iii) improving the geolocation for all points, by using additional information.

4. *How to evaluate the quality of the obtained results?*

   The quality estimates and parameter estimates are mutually dependent. To evaluate the quality of the obtained results, we should compute the precision of the estimates and evaluate the reliability of the model, and perform cross-validation when additional information is available.

1.5. Research limitations

To narrow down the scope, this study will neither address the problem of finding coherent points (Jiang, 2014; Jiang et al., 2015), nor the densification of persistent scatterer networks (Mahapatra et al., 2014). It focuses on point scatterers, rather than distributed scatterers (Samiei-Esfahany and Hanssen, 2011; Goel, 2014), but could nevertheless be applied to distributed scatterers equally well. Rather than focusing on the direct interpretation of the detected deformation signals, we attempt to facilitate the interpretation by domain experts (see e.g. chapter 4). Finally, we do neither address PSI data processing techniques (Kampes, 2005; van Leijen, 2014), nor the precise 3D positioning (Perissin, 2006; Dheenathayalan et al., 2014), but rather focus on post-processing techniques, using the output of standard InSAR time series processing chains.

1.6. Methodology and outline

The current chapter briefly reviews the background of the study, and addresses the research objectives. The main problem is formulated to reach the objectives which are subsequently divided into four specific research questions.

Chapter 2 provides an overview of radar interferometry, introducing the existing techniques, particularly conventional InSAR and PSI. It serves as a general reference for SAR data processing and discusses the physical aspects of signal propagation and scattering. A theoretical framework consisting of a functional and stochastic model is also presented in chapter 2.

Chapters 3 to 6 are written based on manuscripts that have been published in scientific journals, or have been submitted to journals.

Chapter 3 is concerned with finding the optimal kinematic model for each InSAR measurement point. It applies concepts of hypothesis testing and translates the methodology developed in the *Delft School* for geodesy and surveying to the domain of radar remote sensing. It is demonstrated how to detect potentially hazardous situations from millions of InSAR measurement points. This chapter has been submitted to the *IEEE Transactions on Geoscience and Remote Sensing* in February 2015.

Chapters 4 and 5 focus on two domains of structural health assessment of infrastructure: railways (Chap. 4) and buildings (Chap. 5).

Chapter 4 starts with the detection of ground motion of the Qinghai-Tibet railway in relation to potential permafrost thawing using medium-resolution SAR data. This

demonstrates the advantage of using remote sensing data for structural health assessment at inaccessible regions, such as the high altitudes of the Himalaya's. The chapter then continues with the assessment of differential 3D motion for the Betuwe railway in the Netherlands, using multi-track high-resolution TerraSAR-X images. The chapter is based on two publications, in the *International Journal of Remote Sensing* in November 2014 and the *International Journal of Railway Technology* in August 2014.

Chapter 5 is an example of *forensic* research using remote sensing, applying the PSI time series of four SAR satellites over the site of a shopping mall in Heerlen, the Netherlands. This building experienced a near-collapse, which appeared to be due to a developing sinkhole, related to early mining activities. The chapter further covers the interpretation of the driving mechanisms and the probability of precursory anomaly detection. This chapter is extended from the material published in *Remote Sensing of Environment* in April 2014. Conclusions and recommendations for future research are given in Chapter 6.

2
InSAR Review

SAR Interferometry (InSAR) including multi-epoch processing techniques such as Persistent Scatterer Interferometry (PSI) are among the rapidly developing new technologies for Earth observation from space since the late 20th century. In this chapter brief reviews of conventional InSAR and PSI are presented in section 2.1 and 2.2, followed by the discussion on the functional and stochastic model in section 2.3 and 2.4, respectively.

2.1. Synthetic aperture radar interferometry

A synthetic aperture radar (SAR) operates at microwave frequencies and uses the phase information in the radar's along-track spectrum to discriminate scatterers within the antenna beam (Wiley, 1954). It can create two-dimensional images at a wide scale with SAR sensors mounted on an aircraft, or spacecraft. Compared with optical instruments such as the ones on the LandSAT, SPOT and IKONOS satellites whose images are merely acquired in daytime and would be impacted by clouds, SAR sensors utilize radio wave signals which can penetrate the atmosphere including clouds, all-day to obtain images with a resolution up to meters.

2.1.1. Observables

A satellite SAR system operates using a side-looking geometry and illuminates a swath parallel to the satellite's nadir track by transmitting a series of radar pulses from a fixed antenna (Elachi, 1987), see Fig. 2.1a. In a single radar acquisition/image, when two surface objects have the same slant distance to the sensor, it is not possible to separate them. The synthetic aperture radar techniques resolves this problem by combining overlapping radar pulse returns from different azimuth positions. This way, the slant distances to the two objects will differ, and a high-resolution image can be computed. However, this technique still yields a two-dimensional projection of the Earth's surface. The third dimension—resolving points at different elevations—requires another SAR image which is acquired at the same time from a different orbital track or acquired at separated time but imaging the same area. This SAR post-processing method is called SAR Interferometry (InSAR): a form of multiplicative interferometry (Bamler and Hartl, 1998). It can potentially measure sub-centimeter-scale changes in position over time spans of days to years. The two SAR images are called the master image and slave image. The slave image must be coregistered and resampled w.r.t. the geometry of the master image. The interferometric phase is derived from the pixel by pixel multiplication with the conjugate complex of a pixel, in the master and slave image, which yields

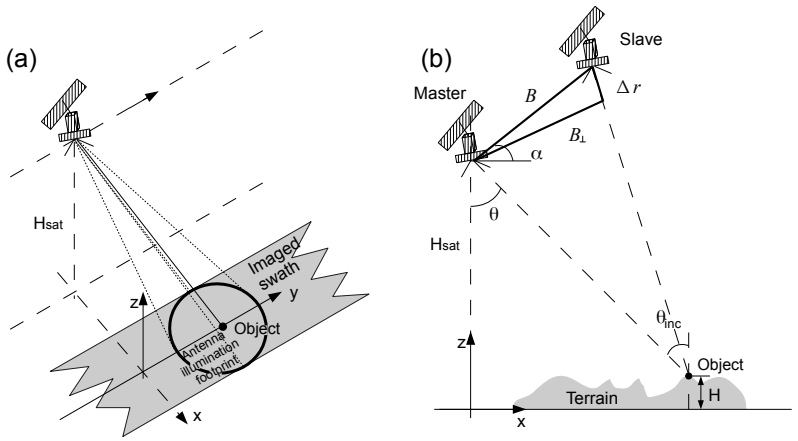

Figure 2.1: (a) SAR and (b) repeat-pass InSAR imaging geometry, adapted from Bamler and Hartl [1998]. (a) The satellite at height H_{sat} moves along the azimuth direction for y axis and the direction of the main lobe of microwave pulse is nominated as the range direction for x axis. The area circled by black indicates the footprint of a single pulse. (b) Two SAR sensors, master and slave are at a distance by a baseline B. The perpendicular baseline $B_\perp$ is defined by the effective distance between master and slave sensors, measured perpendicular to the look direction. The angle between B and horizontal plane is defined as α. The look angle θ is the angle with which the radar looks at the surface. The incidence angle θ_{inc} is defined w.r.t. to the ellipsoid. The height of the object is H w.r.t. a reference surface.

a value $\phi^w \in [-\pi,\ \pi)$ [rad] that we refer to as the 'wrapped', or relative, interferometric phase. If we would have been able to observe the 'absolute' phase $\phi \in \mathbb{R}$ ($\mathbb{R}$ is the set of real numbers), it would be directly related to the slant range difference Δr between master and slave (see Fig. 2.1b), as in[1]

$$E\{\phi\} = -\frac{4\pi}{\lambda}\Delta r, \tag{2.1}$$

where $E\{.\}$ expresses the expectation operator. However, the absolute interferometric phase ϕ cannot straightforwardly be measured, due to the fact that the interferometric observed phase ϕ^w, that we measure, is a relative phase, modulo 2π radians, expressed as $W\{\phi\} = \text{mod}\{\phi+\pi,\ 2\pi\} - \pi$, where $W\{.\}$ is the wrapping operator.

The absolute interferometric phase ϕ can be decomposed into four components that are surface topography, temporal displacement, atmospheric delay and noise,

$$\phi^w = W\{\phi\} = W\{\phi_{\text{topo}} + \phi_{\text{defo}} + \phi_{\text{atmo}} + \phi_{\text{noise}}\}, \tag{2.2}$$

where,

[1] Note that Eq. (2.1) holds for the repeat-pass configuration where the two SAR images are acquired at different times.

$\phi_{\text{topo}} = -\frac{4\pi}{\lambda}\frac{B_\perp}{\rho \sin\theta} H$	the topographic phase caused by the surface geometry, ρ is the slant range, H is the height above a reference surface
$\phi_{\text{defo}} = -\frac{4\pi}{\lambda}\Delta r$	the kinematic phase duo to surface or object displacement
ϕ_{atmo}	the phase contribution from atmospheric signal delay
ϕ_{noise}	other random additive noise.

From Eq. (2.2) it is obvious that for each pixel, there is only one observation, with four (or five, including phase ambiguities) unknown constituents. Thus, a single interferogram cannot solve this estimation problem. A typical interferogram is shown in Fig. 2.2 which depicts the west of the Netherlands (Rotterdam area) using TerraSAR-X stripmap mode data. The phase is wrapped in the $[-\pi, \pi)$ interval. It is impossible to interpret this unambiguously in topographic or kinematic, or atmospheric contributions, due to too many unknowns including phase ambiguities. Phase unwrapping is needed to estimate the number of 'absolute' phase ambiguities, to obtain a continuous interferometric phase map.

The forward problem for wrapping the absolute phase to the range $[-\pi, \pi)$ is straightforward, whereas the inverse problem is difficult due to its inherent non-uniqueness and non-linearity (Ghiglia and Pritt, 1998). For example, Fig. 2.3 shows one-dimensional phase unwrapping in four cases: (a) regardless of aliasing and noise, when the discrete wrapped phase is well-sampled, it is possible to reconstruct the continuous unwrapped phase; (b) when the wrapped phase is undersampled, the unwrapping fails; (c) when the wrapped phase is affected by Gaussian noise, residues occur, those are unwrapping errors. Residues are the evidence of phase discontinuities, indicating the magnitude of incorrect multiples of 2π; (d) when both undersampling and Gaussian noise occur, the phase unwrapping result is far away from the true absolute phase. To unwrap an interferogram in two dimensions, the problem becomes more complex. Various algorithms have been proposed, such as the Branch-cut method (Arfken, 1985; Goldstein et al., 1988; Ching et al., 1992), the Least-squares method (Hunt, 1979; Ghiglia and Romero, 1994; Pritt, 1996) and Minimal cost flow methods (Costantini, 1996). All algorithms hold two general heuristic assumptions to constrain this inverse problem,

1. the gradients between wrapped phase and unwrapped phase are identical;
2. the absolute phase difference for adjacent pixels is smaller than π (half a fringe cycle).

In order to address the non-uniqueness, or rank defect in Eq. (2.2), an extension of InSAR techniques was proposed. In Differential InSAR (DInSAR), two interferograms are generated from three or more SAR images taken at different times. Gabriel et al. (1989) first reported its application to map the surface deformation of agricultural fields over a large area in California to centimeter-level accuracy using SEASAT data. In such an approach, two interferograms were required, one of which is a so-called topographic interferogram that is assumed to only contain the signature of topography, whilst the other one is a deformation interferogram measuring both topography and deformation. The phase differences in the topographic interferogram were scaled to match the imaging geometry of the deformation interferogram and were subtracted from each other, yielding a differential interferogram. Massonnet and

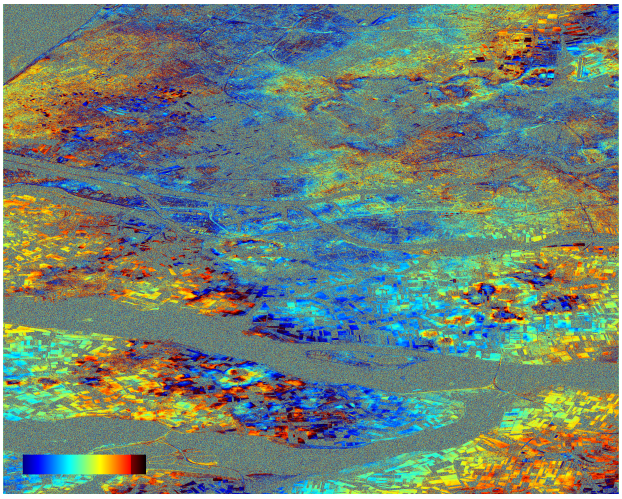

Figure 2.2: Interferogram over the west of the Netherlands (Rotterdam area) in radar coordinates. It is generated by two TerraSAR-X stripmap mode SLC images which were acquired on 04 May and 15 May, 2012 from descending orbit, respectively. The crop area is 28×49 km with a multilook of factor 5×10. The colors show the interferometric phase ranging from $-\pi$ (blue) to $+\pi$ (red). This interferogram mainly shows the effects of atmospheric delay differences.

Adragna (1993) detected the 1992 Landers earthquake surface deformation signature using ERS-1 satellite repeat-pass SAR data after removing the topographic phase component using a reference Digital Elevation model (DEM). Zebker et al. (1994b) developed the three-pass method and performed an application on the Landers earthquake in 1992, which showed good agreements with independent Global Positioning System (GPS) and Electronic Distance Measurement (EDM) data.

2.1.2. Limitations of conventional InSAR

InSAR is one of the most reliable technologies for 3D topographic mapping and Earth deformation monitoring. However, the generated interferograms may include 'decorrelated areas', where the quality of the phase observations is mediocre or even insufficient due to temporal decorrelation effect. In addition, error sources such as those introduced by orbital inaccuracies and atmospheric delays are an impediment to the precise determination of surface deformation. Here we address the three main shortcomings of (conventional) InSAR techniques.

Spatial decorrelation Spatial or geometric decorrelation (Zebker and Villasenor, 1992), between two SAR images, is brought about by their different viewing angles which degrades the coherence of the interferometric phase, for distributed scatterers. The different viewing angles are caused by different squint angles and non-zero perpendicular baselines $B_\perp$ (see Fig. 2.1b for definition) from two platform positions. It leads to a spectral shift between the two observations and alters the coherent sum of wavelets in a resolution pixel so that the two measurements are not exactly the same. As the baseline B increases, the spatial decorrelation increases as well. The critical baseline is the minimum value of $B_\perp$ at which the backscatter signal from each pixel is completely decorrelated. Gatelli et al. (1994) and Zebker et al. (1994a) separately proposed the formula to calculate the critical baseline,

$$B_{\perp,c} = \frac{\rho\lambda}{2R_g \cos\theta_{\text{inc}}}, \tag{2.3}$$

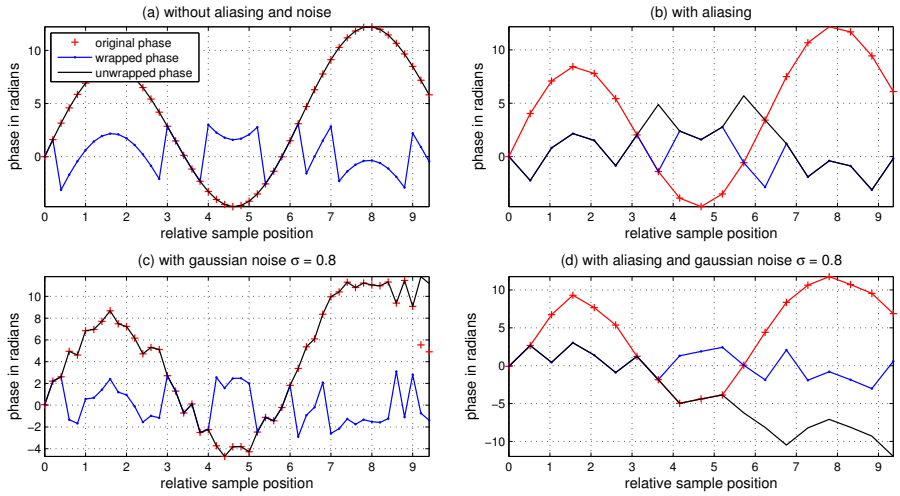

Figure 2.3: Reconstruction of absolute phase from wrapped phase.

where ρ represents the slant distance between the sensor and the target, R_g is the ground resolution and θ_{inc} indicates the local incidence angle and equals to $\theta_{\text{inc}} - \varsigma$ where θ_{inc} represents the incidence angle for the ellipsoid and ς represents the topographic slope. Additionally, a change of squint angle is characterized by a change in the SAR Doppler centroid frequencies between two images, and also affects the geometrical distortion. Spatial correlation can be improved by means of bandpass filtering in range and azimuth directions. Gatelli et al. (1994) showed that range filtering can considerably improve the correlation at the cost of spatial resolution, while azimuth filtering (Schwabisch and Geudtner, 1995) is performed whenever the difference of the SAR Doppler centroid frequencies between two images is larger than half the processed azimuth bandwidth.

Temporal decorrelation Every resolution cell in a SAR image is generally composed of a collection of many small scatterers, and each of them reflects with its individual amplitude and phase. The phase of a pixel is the vector sum of individual phases of all these scatterers. When the phase of an individual scatterer is uniformly distributed between $-\pi$ and π, and all these individual scatterers are mutually uncorrelated (Madsen, 1986), a change of the backscatter characteristics, such as the distribution of scatterers within a common pixel or their electrical characteristics, over the acquisition time period between two SAR images, affects the coherence of the interferogram which is referred to as temporal decorrelation. Especially in vegetated areas and snow-clad mountains, where the scatterer characteristics or the position of scatterer changes over time, the InSAR measurements are severely affected by temporal decorrelation. Moreover, temporal changes are complicated to be modeled in advance and predicted. For instance, the vegetation growth for a certain crop may be modeled as it is based on a natural systematic process, but the unexpected human interference or a natural hazard immediately leads to inadequate modeling. Another example is that in snow-clad

mountain areas, complete decorrelation may dramatically reduce when snow melts away.

Zebker and Villasenor (1992) first presented an approximation of temporal decorrelation assuming that temporal changes are merely caused by the separate motions of scatterers, expressed as

$$\gamma_t = \exp\left\{-\frac{1}{2}(\frac{4\pi}{\lambda})^2\sigma_\phi^2\right\}, \tag{2.4}$$

where γ_t denotes the temporal decorrelation, and σ_ϕ^2 is the phase variance of the motions. These motions were then specified as Brownian motion[2] by Rocca (2007). He assumed that the motion of individual scatterer is Brownian motion which implies that the phase variance σ_ϕ^2 linearly increases with the time period nT (T is satellite repeat cycle, n is the number of repeat cycles), that is $\sigma_\phi^2 = \sigma_{\mathrm{Bd}}^2 nT$. Then the temporal decorrelation is formulated as

$$\gamma_t(nT) = \exp\left\{-\frac{nT}{\tau}\right\}, \tag{2.5}$$

where $\tau = 2/\sigma^2$ and $\sigma = \sigma_{\mathrm{Bd}}/\sqrt{\mathrm{day}}\frac{4\pi}{\lambda}\mathrm{rad}$ where $\sigma_{\mathrm{Bd}}/\sqrt{\mathrm{day}}$ is a standard deviation in a day which is a function of its corresponding coherence value.

With Eqs. (2.4) and (2.5), we can estimate the temporal decorrelation as a function of the phase variance.

Atmospheric inhomogeneities As a radar signal travels through the atmosphere, it is delayed introducing a variable phase over the image, as in Eq. (2.2) (Hanssen, 2001). The atmospheric phase variation is contributed by (i) turbulent mixing that results from turbulent processes in the atmosphere, which is largely uncorrelated with topography; and (ii) a change in the vertical stratification of the troposphere between the lowest and highest elevations in the area, which is highly correlated with topography. The atmospheric phase variation is spatially and temporally correlated. Since the time interval between two acquisitions is typically in the order of one week or more, the atmospheric phase at the two SAR acquisitions is generally decorrelated in time. A widely used approach for reducing the atmospheric phase influence is to combine information from a stack of interferograms using multi-epoch InSAR techniques (which will be discussed in section 2.2) at the expense of losing information on short-term variation in the temporal nature of deformation covering the time period of the SAR acquisitions within the stack (Sandwell and Price, 1998; Sandwell and Sichoix, 2000).

In short, even if SAR data are acquired successfully, error sources limit the number of effective repeat-pass interferograms.

2.2. Multi-epoch InSAR techniques: Persistent scatterer interferometry

Although there are many techniques for InSAR data time series, such as SBAS (Berardino et al., 2002; Mora et al., 2002; Lanari, 2003; Tizzani et al., 2007; Lanari et al.,

[2]Brownian motion is a Wiener stochastic process with stationary independent increments in time. It is a normal distributed variable with zero expectation and time-dependent variance (Hida, 1980).

2010) and SqueeSAR (Ferretti et al., 2011), we will only briefly discuss the concept of PSI here, as an example of multi-epoch InSAR techniques.

PSI (Persistent scatterer interferometry) is a multi-epoch InSAR analysis technique, aimed to overcome spatial and temporal decorrelation and atmospheric error signal in conventional InSAR, first reported by Ferretti et al. (2000b). The concept of the PSI technique is based on discriminating (pointwise) coherent scatterers from incoherent ones so as to analyze the observations of those coherent scatterers that are physically interpretable in a stack of interferograms. Those consistently coherent scatterers often have high-amplitude echoes to the satellite, and are relatively stable ground targets which hold minimal spatial and temporal decorrelation throughout the whole stack. The atmospheric influence for those scatterers can be estimated under the assumption that the atmospheric phase is spatially correlated and temporally uncorrelated. Since the degree of decorrelation for a pixel in an interferogram is related to the distribution of scattering centers that contribute to that pixel, the decorrelation turns out to be zero when the phase of a pixel results from only one stable point scatterer. However, such pixels do not exist in reality. Pixels are either dominated by pointwise scatterers (i.e. PS) which exhibit less decorrelation than the others, or dispersed with many distributed scatterers which are homogeneous in space. PSI considers the pointwise coherent scatterers. PSI is widely applied in urban areas where a large number of man-made structures with strong scattering characteristics is dominant and where the deformation rate is assumed to be constant. In the following the generic PSI processing procedure is addressed based on the *DePSI* methodology (Kampes and Hanssen, 2004a; Marinkovic et al., 2006; van Leijen, 2014).

2.2.1. PSI processing procedure

During PSI processing, we analyze a stack of interferograms, typically consisting of two dozen or more SAR images. The way to generate all these interferograms is as the same as the way in conventional repeat-pass InSAR, which basically follows the obligatory steps: 1) reading the master image and the associated orbital data, and cropping the area of interest; 2) reading the slave image and the associated orbital data, and cropping the same area; 3) corregistering the slave image to the master grid; 4) resampling the slave image; 5) generating the interferogram by multiplying the master image by the complex conjugate of the slave image, pixel by pixel. We will not elaborate the processing procedure for the interferogram generation in this section, as the detail can refer to the literature (Hanssen, 2001; Kampes, 1999).

As the processing procedure for PSI can be subdivided in a number of subsequent steps, here we address these steps in the order of processing. We will limit ourselves to the processing of single-master stacks, producing m interferograms from $m+1$ SAR images.

Single master selection The PSI processing procedure starts by computing interferograms. The master image is selected by maximizing the stack coherence of a batch of interferograms (Kampes, 2005),

$$\gamma^k = \frac{1}{m}\sum_{k=0}^{m} g(B_\perp^k, B_\perp^{\text{cri}}) \times g(B_t^k, B_t^{\text{cri}}) \times g(f_{\text{dc}}^k, f_{\text{dc}}^{\text{cri}}), \tag{2.6}$$

where

$$g(x,c) = \begin{cases} 1-|x|/c, & \text{if } |x| < c \\ 0, & \text{otherwise,} \end{cases} \tag{2.7}$$

and $B_{\perp}^{k}$ is the perpendicular baseline between master and slave in the interferogram k, B_{t}^{k} is the temporal baseline [y] (in years) and f_{dc}^{k} is the Doppler baseline (the mean Doppler centroid frequency difference). m is the total number of interferograms. The divisor c in Eq. (2.7) can be considered as a 'critical baseline', indicating the value above which total decorrelation would occur for distributed targets. $B_{\perp}^{c}$ can derived by Eq. (2.3).

Persistent Scatterer Candidates (PSc) selection A preliminary estimation is performed using a set of constantly coherent pixels, or first order Persistent Scatterer Candidates (PS1c's), this step is aiming to construct an unwrapping network and estimate the atmospheric phase at these pixel positions in all interferograms in order to separate the atmospheric phase from other effects. This step is performed by a sequence of filters at a network of first order PSc's (PS1c's) (Ferretti et al., 2001; Kampes and Hanssen, 2004a). To determine whether the pixels are constantly coherent and then build a robust PS1c network, the phase-based PS selection cannot be straightforwardly used because the phase still contains unknown signals and the wrapped phase follows the uniform distribution as in Eq. (2.21). Thus, as an alternative, the amplitude-based PS selection using normalized amplitude dispersion (Ferretti et al., 2001) is treated as an alternative method based on the assumption that a high and nearly constant amplitude value has a corresponding low phase dispersion. Its formula shows

$$D_a = \frac{\sigma_a}{\mu_a} \approx \widehat{\sigma}_{\phi}, \tag{2.8}$$

where σ_a denotes the standard deviation of the amplitude and μ_a denotes the mean value of the amplitude. Ferretti et al. (2001) numerically simulated the phase stability estimation, showing that the amplitude dispersion is low when $\sigma_{\phi} < 0.25$ [rad]. When D_a exceeds the critical threshold (e.g. > 0.4), there will be no linear relationship between D_a and σ_{ϕ}. Therefore, PS1c's are empirically detected if D_a is below a given threshold (e.g. between 0.25 and 0.4). Fig. 2.4 illustrates the behavior of the complex numbers for 131 generated interferograms using TerraSAR-X data acquired between April 2009 and August 2013 for a PS and a non-PS during the PS1c selection. This demonstrates that the assumption that the stable phase corresponds to a low amplitude dispersion. Fig. 2.4a shows that the angles (or phases) of the PS orientate in a small range $(-\pi/2,\ +\pi/2)$, while the angles of the non-PS distribute randomly in 2π range as shown in Fig. 2.4b. The amplitude values for the PS are greater and stable with a lower dispersion in time, from their similar lengths in Fig. 2.4a, while the amplitude values for non-PS are distinctly varying with the time, as shown in Fig. 2.4b.

Adam et al. (2004) suggested another method for PSc selection using the signal-to-clutter ratio (SCR). It is estimated by calculating the ratio of the intensity (magnitude) of a signal s over its neighboring clutter c. The relationship between the SCR and the phase standard dispersion can be defined as

$$\widehat{\sigma}_{\phi} = \frac{1}{\sqrt{2 \cdot s^2/c^2}} = \frac{1}{\sqrt{2 \cdot \mathrm{SCR}}}. \tag{2.9}$$

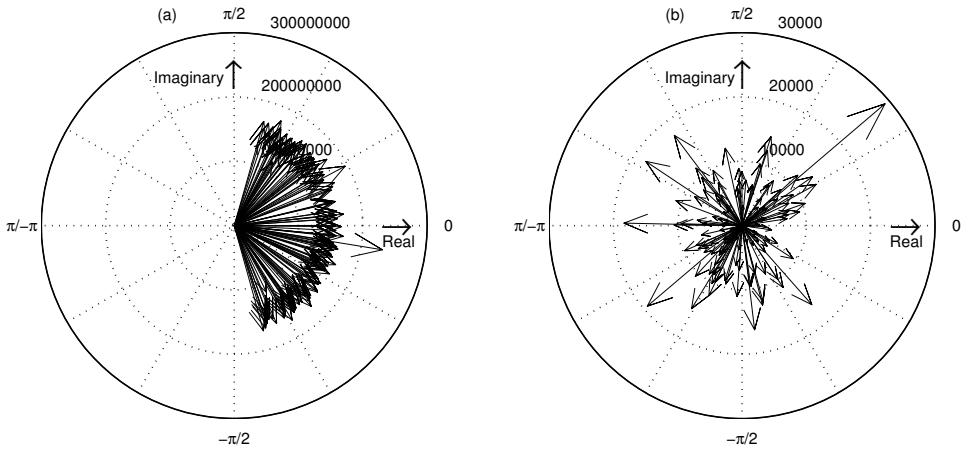

Figure 2.4: Illustration of the complex numbers (phase and amplitude) using TerraSAR-X data acquired between April 2009 and August 2013 from descending orbits for a PS (a) and a non-PS (b).

It is evident that $\widehat{\sigma}_\phi$ is inversely proportional to SCR, for instance, the phase standard deviation needs to be lower than 0.5 [rad], the SCR is 2 at least. Different from the computation for amplitude dispersion index, see Eq. (2.8), the SCR estimation can start with a single SAR image, and a point who bears high SCR over the full time period is selected as a PS1c.

To tackle with the difficulty that insufficient coherent points can be identified in a largely decorrelated environment, Hooper et al. (2004) proposed an alternative approach to analyze spatial phase stability. Under the assumption that the deformation of adjacent PSc's is spatially correlated, the phase stability of a certain temporally coherent point p is formulated as

$$|\gamma_p| = \frac{1}{m}\left|\sum_{k=1}^{m} \exp\left\{j(\phi_p^k - \overline{\phi}_p^k - \Delta\widehat{\phi}_{p,e}^k)\right\}\right|, \tag{2.10}$$

where m is the number of interferograms, ϕ_p^k represents the interferometric phase observable p in the kth interferogram and $\overline{\phi}_p^k$ is the mean phase of all PSc's lying in a circular patch centered at p, and $\Delta\widehat{\phi}_{p,e}^k$ is the estimation of the DEM (Digital Elevation Model) error. The DEM error represents the residual topographic height after subtracting an an a-priori DEM. It can be either due to inaccuracies in the DEM, or due to the position of actual scatterers relative to the DEM, e.g., related to the elevation of a building. Considering efficiency, PSc's are initially identified by defining a threshold in the normalized amplitude dispersion. Then with an iterative algorithm, the points with higher γ_p are considered as PSc.

Network construction and phase unwrapping After selecting the PS1c's that satisfy a certain criterion, e.g. amplitude dispersion index, a reference network is established by connecting these PS1c's based on e.g. Delaunay triangulation or a spider network (Kampes, 2005). An 'arc' is defined as the spatial phase difference between two con-

necting PS1c's. It is first computed and used as input for the processing. The maximum length of an arc is defined beforehand so as to reduce or even eliminate the atmospheric signals between two linking PS1c's, typically between 0.5 and 2 km (van Leijen, 2014). In the stage of phase unwrapping, the arcs are first unwrapped in time and then integrated in space. Variance component estimation (VCE) (details in section 3.4) is employed to produce the proper weights for the arc observations. Whenever the arc estimation is calculated via the Least-squares, the variance is calculated when the residuals between observables and estimations approach to minimum (Teunissen, 1988).

Orbital and atmospheric phase screen estimation Orbital inaccuracies affect the interferograms in the forms of a smooth spatial signal, and result in erroneous baseline vector estimation, which influences the estimation of the topographic phase in the PSI processing (Bahr and Hanssen, 2012). A first order approach to eliminate this effect is the subtraction of a linear plane (or phase ramp) in both range and azimuth direction. Any other spatial long wavelength signal, such as a large scale deformation due to tectonic movements or tides, are inevitably subtracted as well by this approach. Even though it is efficient for most cases and easy to implement, it still remains a bias since the orbital component is not rigorously linear. More robust approaches in terms of the measurement of phase differences or gradients between two given pixels, proposed by e.g. Kohlhase et al. (2003), are applied by modification of satellite trajectories. Another approach regardless of prior unwrapping is the gridsearch method (Bahr and Hanssen, 2012). This approach is based on an integral transform of the wrapped interferogram. For all the approaches, the orbital correction is relative and independent for every interferogram. Therefore, orbital error estimation for a single interferogram refers to the estimation of baseline errors, and its residual error can propagate to the estimated height ambiguity or to the reference phase (Hanssen, 2001). Considering that the phase of every PS1c is unwrapped at the stage of network construction and phase unwrapping, the phase ramp estimation can be formed as

$$\Phi^k_{\mathrm{p,unw}} = \mathrm{az}_p \cdot s^k_{\mathrm{az}} + \mathrm{rg}_p \cdot s^k_{\mathrm{rg}} + c, \tag{2.11}$$

where $\Phi^k_{\mathrm{p,unw}}$ is the unwrapped arc phase of PS1c p in the kth interferogram (Caro Cuenca, 2012). az_p and rg_p denote the azimuth and range coordinates in the design matrix, respectively. The parameters s^k_{az}, s^k_{rg} represent the slopes in azimuth and range direction, and c is a constant all arcs are calculated w.r.t. a common reference PS. The unknowns s^k_{az}, s^k_{rg} and c can be estimated by the Least squares estimation.

Atmospheric signal in the master and slave images limits the application of conventional InSAR but can be estimated in PSI processing by window-based filter. We assume that the phase due to the atmospheric delay is uncorrelated in time as long as the minimum temporal baseline is larger than one day, but correlated in space. Hence, we perform high pass filter (HP) in time, and low pass filter (LP) in space, for the unwrapped residual of every PSc. The unwrapped residual at position p in the kth interferogram includes non-linear displacement and unmodeled noise, which is denoted as e^k_p. Since the master atmospheric phase prevails in all interferograms, and it cannot pass the temporal filtering, we first perform the temporal filtering on (Ferretti et al.,

2000b)

$$e_p^{k\prime} = e_p^k - \bar{e}_p, \tag{2.12}$$

where $\bar{e}_p$ represents the master atmospheric phase which is the temporal mean phase residual. Then we perform the spatial filtering, which can be written as, cf. Ferretti et al. (2000b)

$$\hat{\phi}_{p,\text{atmo}}^k = \left[\left[e_p^{k\prime}\right]_{\text{HP-time}}\right]_{\text{LP-space}} + \left[\bar{e}_p\right]_{\text{LP-space}}, \tag{2.13}$$

where $\hat{\phi}_{p,\text{atmo}}^k$ is the estimated atmospheric phase at position p in the kth interferogram. HP-time and LP-space represent the filtering operators: high pass filter in time and low pass filter in space.

PS network densification The orbital ramp and atmospheric signal are estimated and separated based on the aforementioned methods, for the PS1c's network. A full atmospheric phase screen (APS) is then interpolated and separated from all other PSc's (termed as second order PSc's (PS2c's)). An Ordinary Kriging method (Wackernagel, 1995) can be used to compute the APS, which is able to smoothly interpolate the atmosphere phase for all PSc's and drop the noise part by estimating the nugget in variogram estimation (Caro Cuenca, 2012).

The PS2c's intensify the density of the PS1c network (or the arcs) by connecting other PSc's (PS1c's and PS2c's) by means of a region growing approach, which is referred to as the PS network densification (Kampes, 2005). These newly built arcs are first unwrapped in time and then used to determine the contribution of every phase component (i.e. as in Eq. (2.2)). In order to guarantee the quality of results for this network, we need to remove the specious PSc's (which are noise but have been falsely identified as the coherent points) in the network using spatial-temporal consistency (STC) (Samiei-Esfahany et al., 2008).

Geocoding Geocoding is applied to convert the SAR image coordinates to a unified geodetic reference system for all PS, for instance WGS84, by using a set of Doppler, range and ellipsoid equations (Schwäbisch and Geudtner, 1995). The geolocation error caused by SAR system timing offsets in slant range and azimuth will be propagated to the unified geodetic reference system. This error may result from (i) the geolocation error of the reference PS point, as all PS heights are relative heights w.r.t. a certain reference PS point for *Doris* and *DePSI* processing, thereby we should consider the error of the reference point; or (ii) the processing errors. For instance, every PS height can be estimated based on a Digital Elevation Model (DEM) e.g. derived from the Shuttle Radar Topography Mission (SRTM) (van Zyl, 2001), or GTOPO30 data (Miliaresis and Argialas, 1999). Since the spatial resolutions of these DEM data may be lower than the spatial resolution of SAR image, the height estimation is then biased, and the geolocation error for every PS is introduced.

WGS84 is the InSAR reference frame during the projection from the slant unwrapped phase to elevation, an error in the vertical direction (i.e. the PS height estimation error) causes a horizontal deviation $e_{\text{hor}}[m]$ of approximately calculated as

$$e_{\text{hor}} = \frac{H}{\tan(\theta_{\text{inc}})}, \tag{2.14}$$

where θ_{inc} is the local incidence angle. The horizontal deviation is inversely proportional to the local incidence angle. For instance, given TerraSAR-X data with a look angle of 21.6°, this horizontal deviation scales up to $2.5 \times H$.

Moreover, inaccuracies in the orbital state vectors, radar system time errors, atmospheric delay, solid Earth tides, tectonic drift, or improper interpolation degrade the precision of geocoding. Scharroo and Visser (1998), and Doornbos and Scharroo (2004) reported that the accuracy of along-track and radial components of ERS orbits are 4 cm and 15 cm respectively, depending on the gravity model used during data processing. For Envisat, the accuracy of the best orbit products provided by the DORIS (Doppler Orbitography and Radiopositioning Integrated by Satellite) system, is estimated to be 3 cm in the radial component and 10 cm in 3D (Otten and Dow, 2004). For the GPS-based orbits of ALOS, the deviations are between 2 to 15 cm in 3D (Nakamura et al., 2007). Regarding TerraSAR-X, the orbital accuracy has reached to the 2 cm level (Yoon et al., 2009; Eineder et al., 2011). Consequently, the effect of orbital errors on geocoding needs to be taken into account in the condition of lacking of precise orbit data.

2.2.2. Limitations of PSI

PSI is a well-established technique that uses all available SAR images to estimate the kinematic (deformation) time series for consistently coherent points (PS), in a wide area. It allows us to semi-continuously monitor the kinematic behavior of individual features, such as buildings and dams, with sub-centimeter accuracy. However, PSI still has several limits because of the system setting of radar satellite (e.g. the satellite repeat time) and the dependency on some rather harsh assumptions needed for PSI processing (e.g. kinematic time series are assumed as a linear function of time). Here we address the four main limits of PSI.

Temporal sampling limit is the first limit of PSI. The capability of temporal sampling is dependent on the capability of the satellite repeat time (Crosetto et al., 2010). The sparse temporal sampling degrades the temporal 'resolution' and the quality of parameter estimators (e.g. kinematic parameter in Eq. (2.16)). An abrupt surface deformation occurring in the time interval between two SAR acquisitions, is undetectable. Moreover, suppose the kinematic behavior is a linear function of time with one parameter: the linear deformation rate. Since the true deformation cannot be retrieved unambiguously when the deformation phase between two adjacent acquisitions is larger than π, the deformation of $\lambda/4$ is the maximum value per repeat time interval T [days]. Therefore, the absolute maximum detectable deformation rate is related to the satellite repeat time interval T [days] and radar wavelength λ, formed as (Kampes, 2005)

$$v_{\max} = \frac{\lambda/4}{T/365}, \tag{2.15}$$

which implies that the PSI technique would be insensitive to measure the significant kinematic behavior with a $> v_{\max}$ deformation rate.

Spatial sampling limit is the second limit of PSI. (i) It is in fact that the PSI technique is merely focused on the PS points. The density of the PS points is relatively higher in urban areas, while it is much lower in rural areas where there are few high reflectivity ground objects. (ii) In PSI processing, the identification of coherent points

is required prior to the PS selection. When a spatial estimation window is used to calculate the coherence, it is suboptimal to detect anomalous changes of a single scatterer since the coherence value is treated as an indicator for all points within the spatial estimation window. When applying the temporal estimation window, a single scatterer that changed would be removed from the coherent points selection due to the decrease of its coherence value.

The third limit is related to the capability of the line-of-sight (LOS) measurements. The observed deformation from a satellite is the projection of 3D deformation in the LOS direction. With the lack of external information, the decomposition from the LOS measurements to the 3D coordinates such as the North-East-Up coordinate system is an ill-posed problem as there is no unique solution.

The fourth limit is related to the robustness against anomalies in the time series, e.g., unwrapping errors or sudden displacements. (i) It is rather laborious to manually check the kinematic time series of a tremendous amount of PS in order to find the anomalous PS among them. (ii) As a new-acquired data is introduced into the existed InSAR image stack, the parameter estimators can be readjusted by a batch processing. However, such a batch processing strategy does not aim at the fast anomaly detection, which is an essential goal for infrastructure monitoring.

Basically, these four limits can be overcome to some extent. The temporal and spatial sampling can be improved by using high-resolution and short-wavelength SAR data acquired by satellites having short repeat orbit cycles, such as TerraSAR-X and Cosmo-SkyMed. The reliable 3D decomposition of the LOS measurements can be produced when the multi-track SAR data covering a same area are available. The case studies to show the improvement in the PSI results by using TerraSAR-X data compared with Envisat data, and to show the reliable 3D decomposition using both ascending and descending orbit data will be presented in chapter 4. The approach to detect the anomaly based on hypothesis testing will be discussed in chapter 3. The theory of short arc and its characteristics will be presented in the section 2.4.3.

So far the advantage and disadvantage of recent InSAR techniques and multi-epoch InSAR processing procedure for the exploration of surface kinematic (deformation) time series are revisited. The following sections review a generic Gauss-markov model for multi-epoch InSAR batch data processing in the fundamentally mathematical view.

2.3. Functional model for multi-epoch processing

The interferometric phase observation of the kth interferogram of an InSAR stack can be considered as the sum of seven terms (Hanssen, 2001), if we subdivide the noise component of Eq. (2.2),

$$\phi^k = \phi^k_{\text{topo}} + \phi^k_{\text{defo}} + \phi^k_{\text{atmo}} + \phi^k_{\text{orb}} + \phi^k_{\text{scat}} - 2\pi a + \phi^k_{\text{noise}}, \tag{2.16}$$

where the topographic phase ϕ^k_{topo} is a function of the perpendicular baseline $B^k_\perp$, radar wavelength λ, incidence angle θ^k_{inc}, the slant range ρ^k between the satellite sensor and a ground target, and the height H above a reference surface. The latter can be written

as

$$\phi^k_{\text{topo}} = -\frac{4\pi B^k_\perp}{\lambda \rho^k \sin\theta^k_{\text{inc}}} H, \tag{2.17}$$

let $\beta^k = -\frac{4\pi B^k_\perp}{\lambda \rho^k \sin\theta^k_{\text{inc}}}$ be the height-to-phase conversion factor for the following part.

The component ϕ^k_{defo} denotes the phase change due to the deformation relative to a postulated reference point in the direction of the radar line of sight. It can be modeled for every point in terms of its kinematic behavior. The potential deformation models will be discussed in section 3.1.

The third and fourth terms ϕ^k_{atmo} and ϕ^k_{orb} in Eq. (2.16) are the phase contributions due to the atmospheric delay and orbital error, respectively. The atmospheric delay in meters (delay is often expressed in meters in this context) is referred to as S, $\phi^k_{\text{atmo}} = -\frac{4\pi}{\lambda} \cdot S$. The orbital error can be well calculated by Eq. (2.11) within a small area (≤ 30 km). The fifth term ϕ^k_{scat} is the phase change due to a change in the ground scatterer characteristics. a indicates the integer number of phase ambiguity. The last term ϕ^k_{noise} represents the unmodeled noise caused by e.g. thermal noise, quantization noise and phase noise due to coregistration errors. In the case of undulating terrain, the dominant part of the topographic phase ϕ_{topo} can be removed either using an external DEM derived from e.g. SRTM or GTOPO30, or using the estimated topographic phase map by two SAR images with a significant perpendicular baseline, assuming that no deformation occurred during their time interval. After removing the main part of topography, Eq. (2.16) changes to,

$$\phi^k = \beta^k \cdot \Delta H + \phi^k_{\text{defo}} - \frac{4\pi}{\lambda} \cdot S + \phi^k_{\text{orb}} + \phi^k_{\text{scat}} - 2\pi a + \phi^k_{\text{noise}}, \tag{2.18}$$

where ΔH is a residual height due to the inaccuracy of the reference DEM. In most cases of both conventional InSAR and PSI, the unmodeled term ϕ^k_{scat} is considered as rms of the deformation (Zebker and Villasenor, 1992) and joins into the noise part in Eq. (2.18). The orbital error is usually accounted for in the noise. Then the remaining parameters of interest, ΔH, v, S and a are estimated.

It is noted that ϕ^k in Eqs. (2.16) and (2.18) are the relative phase observation per arc (w.r.t. the phase of the reference point). To simplify the functional model as in Eq. (2.18), it can be split into real- and integer- unknown parameter vectors $b = [\Delta H \; v \; S]^T$ and a, respectively, expressed as

$$E\{\underline{\phi}\}_{m\times 1} = \underbrace{\begin{bmatrix} A_1 & -2\pi \end{bmatrix}_{m\times n}}_{A} \underbrace{\begin{bmatrix} b \\ a \end{bmatrix}_{n\times 1}}_{X}, \tag{2.19}$$

where m is the number of observations and n is the number of unknown parameters. The stochastic characteristics of the observables $\underline{\phi}$ will be presented in section 2.4.

2.4. Stochastic characteristics for SAR data

2.4.1. Characteristics of scatterers within a SAR resolution element

A response element (also refers to a pixel) on the ground in a SAR image to the arriving radar pulse, comprises numerous small ground elements or scatterers (Krul, 1982). Therefore, it is impossible to determine the response of every individual scatterer in a response element. In practice, we measure the response of a response element in the form of a sum of all scatterers within the response element, which is expressed as a complex number

$$z = \sum_{i=1}^{n} \underline{\varrho}_i = |z| e^{j\psi}, \tag{2.20}$$

where n is the number of small scatterers, $\underline{\varrho}_i$ represents the observed complex number of the ith scatterer, $|z|$ is its amplitude, ψ is its phase and j is the imaginary unit ($j = \sqrt{-1}$). Note that the notation of a SAR phase: ψ is different from the interferometric phase ϕ, such as in Eq. (2.16). A SAR resolution element could be dominated by distributed scatterers that meet with Gaussian (or Rayleigh) scattering distribution, or point(-wise) scatterer that overpowers the contribution of the others in the resolution element (Hanssen, 2001; Bamler and Hartl, 1998).

The distributed scatterers are those that include many random small scatterers within a resolution cell. It is essential that no single scatterer is dominant compared to the others in a resolution cell, and it is assumed there are many mutually uncorrelated scatterers within the element. This assumption holds mainly for natural scatterers such as soil surfaces and agricultural fields. The phase of each individual distributed scatterer ϕ is uniformly distributed between $-\pi$ and π. Its probability density function is shown as

$$\text{pdf}(\psi) = \begin{cases} \frac{1}{2\pi}, & -\pi \le \psi < \pi \\ 0, & \text{otherwise.} \end{cases} \tag{2.21}$$

A point scatterer is considered to be a deterministic signal contaminated by clutter which includes the random circular Gaussian noise of the distributed scatterers.

We can decompose the complex value $z = |z| e^{j\psi}$ into a real, $\text{Re}\{z\}$, and an imaginary part, $\text{Im}\{z\}$, as in

$$z = \underbrace{(|z|\cos\psi + e_r)}_{\text{Re}\{z\}} + j \underbrace{(|z|\sin\psi + e_i)}_{\text{Im}\{z\}}. \tag{2.22}$$

It represents a total return signal from a SAR resolution element. The decorrelation and thermal noise introduce the zero-mean Gaussian variables e_r and e_i into the real and imaginary parts.

In terms of the Circular Gaussian statistics, the generic probability density function (PDF) of a zero-mean, complex circular Gaussian variable z (or the joint PDF of its real and imaginary components) is described as (Dainty, 1975; Davenport and Root, 1987)

$$\text{pdf}(z) = \text{pdf}(\text{Re}\{z\}, \text{Im}\{z\}) = \frac{1}{2\pi\sigma^2} e^{\frac{(\text{Re}\{z\})^2 + (\text{Im}\{z\})^2}{2\sigma^2}}, \tag{2.23}$$

where

$$\sigma^2 = \sigma_z^2 = \sigma_{\text{Re}\{z\}}^2 = \sigma_{\text{Im}\{z\}}^2. \tag{2.24}$$

The joint PDF for the amplitude a ($a = |z|$) and phase ψ is derived as (Hanssen, 2001)

$$\text{pdf}(a,\psi) = \begin{cases} \frac{a}{2\pi\sigma^2} e^{-\frac{a}{2\sigma^2}}, & a \geq 0 \text{ and } -\pi \leq \psi < \pi \\ 0, & \text{otherwise.} \end{cases} \tag{2.25}$$

Since the phase delay due to the propagation of the signal is independent of the scattering amplitude, therefore a and ψ are supposed uncorrelated which suggests that $\text{pdf}(a,\psi) = \text{pdf}(a) \cdot \text{pdf}(\psi)$. The marginal PDF of a is straightforwardly found by integrating ψ out in the range $[-\pi, \pi)$ it is shown as

$$\text{pdf}(a) = \begin{cases} \frac{a}{\sigma^2} e^{-\frac{a}{2\sigma^2}}, & a \geq 0 \\ 0, & \text{otherwise.} \end{cases} \tag{2.26}$$

The amplitude of scatterers is characterized by the Rayleigh distribution (Papoulis, 1968) based on Eq. (2.26).

2.4.2. PDF of an interferometric resolution element

The complex interferogram Z is produced by the complex multiplication of two SAR SLC images

$$Z = z_1 z_2^*, \tag{2.27}$$

where $z_1 = |z_1| e^{j\psi_1}$, $z_2 = |z_2| e^{j\psi_2}$ and the asterisk * means the complex conjugate. The amplitude and phase of Z are defined as $|Z| = |z_1 \cdot {z_2}^*|$ and $\phi = \text{angle}\{z_1 \cdot {z_2}^*\}$. Even though the PDF of the phase follows a uniform distribution as in Eq. (2.21), the PDF of the interferometric phase which is the complex product of two circular Gaussian signals is not necessarily uniform, when two signals have some degree of correlation. Suppose there are two circular Gaussian signals z_1 and z_2 from the two SAR images acquired at different times t_1 and t_2, and having same zero expectation $E\{z_1\} = E\{z_2\} = 0$ and an identical variance $E\{z_1^2\} = E\{z_2^2\}$, the joint PDF of these two is formed as (Just and Bamler, 1994; Bamler and Hartl, 1998)

$$\text{pdf}\{z_1, z_2\} = \frac{1}{\pi^2 |C_z|} \exp\left\{ - \begin{bmatrix} {z_1}^* & {z_2}^* \end{bmatrix} C_z^{-1} \begin{bmatrix} z_1 \\ z_2 \end{bmatrix} \right\}, \tag{2.28}$$

here the complex covariance matrix is denoted as C_z and built as

$$C_z = E\left\{ \begin{bmatrix} z_1 \\ z_2 \end{bmatrix} \begin{bmatrix} {z_1}^* & {z_2}^* \end{bmatrix} \right\} = \begin{bmatrix} E\{|z_1|^2\} & \gamma \sqrt{E\{|z_1|^2\} E\{|z_2|^2\}} \\ \gamma^* \sqrt{E\{|z_1|^2\} E\{|z_2|^2\}} & E\{|z_2|^2\} \end{bmatrix}, \tag{2.29}$$

where the complex coherence γ is computed by

$$\gamma = \frac{E\{z_1 \cdot {z_2}^*\}}{\sqrt{E\{|z_1|^2\} E\{|z_2|^2\}}}, \ (0 \leq |\gamma| \leq 1). \tag{2.30}$$

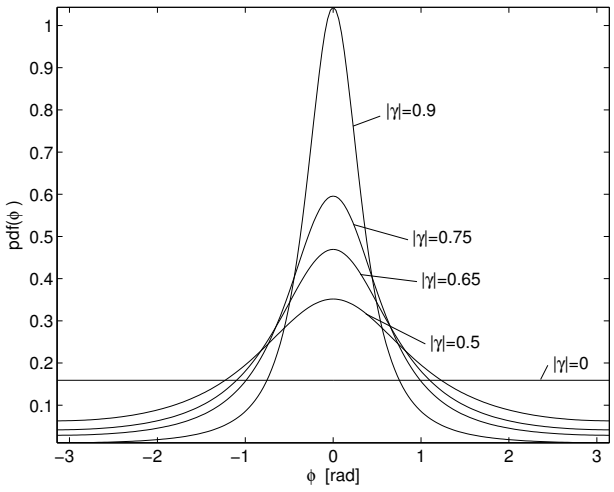

Figure 2.5: The probability density functions for the interferometric phase for coherence levels $|\gamma|$= 0, 0.5, 0.6, 0.75, 0.9. The tallest curve corresponds to the highest coherence.

Just and Bamler (1994), and Tough et al. (1995) derived the PDF of phase in a single-look case,

$$\begin{aligned}\mathrm{pdf}(\phi) = &\frac{1-|\gamma|^2}{2\pi}\,\frac{1}{1-|\gamma|^2\cos^2\left(\phi-\phi_0\right)} \\ &\times\left\{1+\frac{|\gamma|\cos\left(\phi-\phi_0\right)\arccos\left[-|\gamma|\cos\left(\phi-\phi_0\right)\right]}{\sqrt{\left[1-|\gamma|^2\cos^2\left(\phi-\phi_0\right)\right]}}\right\},\end{aligned} \tag{2.31}$$

where ϕ_0 is the maximum likelihood estimator (or the expectation) of the interferometric phase ϕ (Rodriguez and Martin, 1992).

Fig. 2.5 depicts the PDF distributions of the interferometric phase related to corresponding coherence values in a single-look case, based on Eq. (2.31). All of these are periodic with 2π. It shows that the PDF distribution reduces to a uniform distribution on $[-\pi,\ \pi)$ for totally decorrelated signals ($|\gamma|$ = 0, e.g. water area) and approaches a Dirac delta function $\delta(\phi)$ for completely correlated signals ($|\gamma|$ = 1).

The phase variance can be obtained by (Box et al., 1994)

$$\sigma_\phi^2 = \int_{-\pi}^{+\pi}\left[\phi - E\left\{\phi\right\}\right]^2 \mathrm{pdf}(\phi)\,d\phi. \tag{2.32}$$

In the special case that a point scatterer whose $|\gamma|$ is rather close to 1, its phase variance is found by (Bendat and Piersol, 1986; Rodriguez and Martin, 1992; Just and Bamler, 1994)

$$\sigma_\phi^2 = \frac{1-\gamma^2}{2\gamma^2 L} \quad [\mathrm{rad}^2], \tag{2.33}$$

where L is the number of multi-looks.

2.4.3. Characteristics of the arc phase

The interferometric phase is defined as the phase difference between two SAR images. The noise in each SAR image is propagated into the interferometric phase in the form of atmospheric inhomogeneities, orbital error, and temporal and spatial decorrelation. Aiming to reduce the effect of unavoidable noise, the arc phase is the double difference phase between two positions in an interferometric image. Whenever the atmosphere difference between the two positions whose distance is e.g. less than ≤ 1 km, the arc phase is mainly composed of the phase difference due to the height difference and relative deformation difference regardless of the impact of atmospheric delay (Ferretti et al., 2000c). In this case, the arc phase is specified as 'short arc phase'. This section is concerned on the short arc phase.

Functional model for short arc phase

The arc phase between pixel positions p and q from the kth interferogram can be written as

$$\phi_{p,q}^{k} = W\left\{\phi_{p}^{k} - \phi_{q}^{k}\right\} = \text{angle}\left\{Z_{p}^{k} \cdot Z_{q}^{k*}\right\}, \tag{2.34}$$

where $W\{.\}$ is the wrapping operator, ϕ_p^k and ϕ_q^k are the wrapped phases of p and q. Z_p^k and Z_q^k are the interferometric complex values for pixels p and q in interferogram k. When the distance between p and q is rather short so that their atmospheric phase difference is negligible, the corresponding unwrapped arc phase (that is the short arc phase) can hence be decomposed into

$$\phi_{p,q}^{k,\text{unw}} = \beta^{k} \cdot \Delta H_{p,q}^{k} - \frac{4\pi}{\lambda} \cdot D_{p,q}^{k} - 2\pi a + \phi_{\text{noise}}^{k}, \tag{2.35}$$

where $\Delta H_{p,q}^k$ and $D_{p,q}^k$ represent the relative height difference and relative displacement of p w.r.t. q. ϕ_{noise}^k is unmodeled noise, a is the integer cycle ambiguity of arc phase, $a \in \mathcal{Z}$ ($\mathcal{Z}$ is the set of integers). In case of monitoring the deformation of certain buildings and civil infrastructure, the change of the short arc phase for individual structure in one satellite repeat cycle, is assumed to be less than π. It implies that the phase is free from phase ambiguities (that is $a = 0$), and the relative movement is detectable in wrapped domain. It is noted that all points may move in concert, but this is not of practical interest (Chang and Hanssen, 2012).

Stochastic model for the arc phase

Theoretically, the (co)variance matrix for the arc phase is required to be derived from its PDF. According to the functional model of the arc phase (see Eq. (2.34)), the joint PDF of two interferometric phases needs to be obtained first. For every Single Look Complex (SLC) SAR image, the real and imaginary parts of a complex number are obtained first. The interferometric phase for a certain pixel acquired at t_1 and t_2 can be calculated by

$$\underline{\phi}(t_1, t_2) = W\{\underline{\psi}(t_1) - \underline{\psi}(t_2)\}, \quad \psi \in [-\pi, +\pi). \tag{2.36}$$

It is complex to directly derive the PDF of arc phase from the observed interferometric phase which is bounded in 2π module. For simplicity, the interferometric phase is

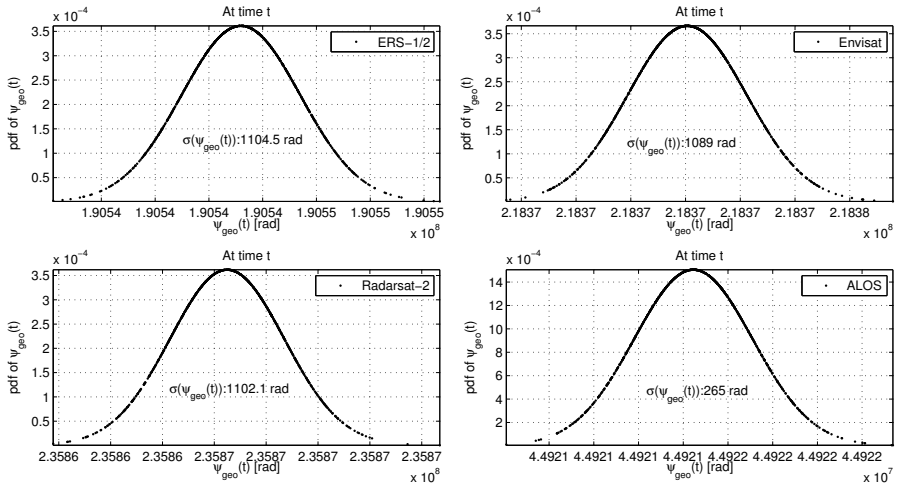

Figure 2.6: PDF of the geo-part of the phase for the ERS-1/2 satellite with 5.66 cm wavelength and 790 km altitude, Envisat satellite with 5.62 cm wavelength and 800 km altitude, Radarsat-2 satellite with 5.55 cm wavelength and 798 km high and ALOS (PALSAR) satellite with 23.62 cm wavelength and 700 km altitude.

supposed to be unwrapped, and the unwrapped phase at the acquisition time t for position p is denoted as $\underline{\psi}(t,p)$. Hence a random vector is defined as

$$\underline{u} = [\underline{\psi}(t_1,p), \underline{\psi}(t_1,q), \underline{\psi}(t_2,p), \underline{\psi}(t_2,q)]^T, \tag{2.37}$$

which is used to attempt to derive its joint PDF $f_{\underline{u}(u)}$.

The individual phase of a pixel in the SAR image at time t for a certain pixel is given by $\underline{\psi}(t) = \underline{\psi}_{\text{geo}}(t) + \underline{\psi}_{\text{scat}}(t)$. Here the geo-part of the phase $\underline{\psi}_{\text{geo}}(t)$ is the phase related to the distance between the satellite and the surface target. According to the geometry of a single-pass satellite, the slant range between sensor and surface object is denoted as ρ while the wavelength is λ. The absolute geo-part of the phase $\underline{\psi}_{\text{geo}}(t)$ at time t is defined as

$$\underline{\psi}_{\text{geo}}(t) = -\frac{2\cdot 2\pi}{\lambda}\rho. \tag{2.38}$$

Fig. 2.6 illustrates the PDF distribution of geo-part of the phase for ERS-1/2, Envisat, Radarsat-2 and ALOS satellites. It demonstrates that the PDF of $\underline{\psi}_{\text{geo}}(t)$ is rather wide which leads to a large-value variance.

The second component for SLC phase, $\underline{\psi}_{\text{scat}}(t)$ is the random observable following uniform distribution and its PDF is reformed from Eq. (2.21)

$$\text{pdf}(\psi_{\text{scat}}(t)) = \begin{cases} \frac{1}{2\pi}, & -\pi \le \psi_{\text{scat}}(t) < \pi \\ 0, & \text{otherwise.} \end{cases} \tag{2.39}$$

Let $d = [1,-1,-1,1]$ be the differencing operator. The double difference phase (or arc phase) is written as $\underline{u}_{\text{DD}} = d \cdot \underline{u}$. The dispersion $D\{\underline{u}\}$ can be described by a symmetric

positive-definite covariance matrix as

$$D\{\underline{u}\} = Q_{\mathrm{uu}} = \begin{bmatrix} \sigma^2_{\psi(t_1,p)} & \sigma_{\psi(t_1,p),\psi(t_1,q)} & \sigma_{\psi(t_1,p),\psi(t_2,p)} & \sigma_{\psi(t_1,p),\psi(t_2,q)} \\ & \sigma^2_{\psi(t_1,q)} & \sigma_{\psi(t_2,p),\psi(t_1,q)} & \sigma_{\psi(t_1,q),\psi(t_2,q)} \\ \mathrm{SYM} & & \sigma^2_{\psi(t_2,p)} & \sigma_{\psi(t_2,p),\psi(t_2,q)} \\ & & & \sigma^2_{\psi(t_2,q)} \end{bmatrix}, \quad (2.40)$$

where $\sigma^2_{\psi(t_1,p)}$, $\sigma^2_{\psi(t_2,p)}$, $\sigma^2_{\psi(t_1,q)}$ and $\sigma^2_{\psi(t_2,q)}$ are the total phase variances for p and q at t_1 and t_2, respectively. $\sigma_{\psi(t_1,p),\psi(t_2,q)}$ and $\sigma_{\psi(t_2,p),\psi(t_1,q)}$ are supposed to be zero under the assumption that the signals echoed from p and q at different times are uncorrelated. $\sigma_{\psi(t_1,p),\psi(t_2,p)}$ and $\sigma_{\psi(t_1,q),\psi(t_2,q)}$ are the temporally-induced covariances for the interferometric phase p and q respectively, which are proportional to the coherence. They are simplified to $\sigma_{\phi(t_1,t_2,p)}$ and $\sigma_{\phi(t_1,t_2,q)}$ for the following equation Eq. (2.41). $\sigma_{\psi(t_1,p),\psi(t_1,q)}$ and $\sigma_{\psi(t_2,p),\psi(t_2,q)}$ are the spatial covariances between p and q at the same time t_1 or t_2, reformulated as $\sigma_{s(t_1,p,q)}$ and $\sigma_{s(t_2,p,q)}$, which are correlated via the atmospheric and orbital errors. $\sigma_{s(t_1,p,q)}$ and $\sigma_{s(t_2,p,q)}$ decay as the distance increases (Hanssen, 2004). It is noted that if there is no a-priori information about the weather condition, we suggest $\sigma_{s(t_1,p,q)} = \sigma_{s(t_2,p,q)}$. Then Eq. (2.40) can be rewritten as

$$D\{\underline{u}\} = Q_{\mathrm{uu}} = \begin{bmatrix} \sigma^2_{\psi(t_1,p)} & \sigma_{s(t_1,p,q)} & \sigma_{\phi(t_1,t_2,p)} & 0 \\ & \sigma^2_{\psi(t_1,q)} & 0 & \sigma_{\phi(t_1,t_2,q)} \\ \mathrm{SYM} & & \sigma^2_{\psi(t_2,p)} & \sigma_{s(t_2,p,q)} \\ & & & \sigma^2_{\psi(t_2,q)} \end{bmatrix}. \quad (2.41)$$

In line with the propagation law of variances and covariances, the arc phase variance of $\underline{u}_{\mathrm{DD}}$ can be derived as

$$\begin{aligned} \sigma^2_{u_{\mathrm{DD}}} &= d \cdot Q_{\mathrm{uu}} \cdot d^T \\ &= \sigma^2_{\psi(t_1,p)} + \sigma^2_{\psi(t_1,q)} + \sigma^2_{\psi(t_2,p)} + \sigma^2_{\psi(t_2,q)} \\ &\quad - 2(\sigma_{s(t_1,p,q)} + \sigma_{\phi(t_1,t_2,p)} + \sigma_{\phi(t_1,t_2,q)} + \sigma_{s(t_2,p,q)}). \end{aligned} \quad (2.42)$$

Due to the motion of small scatterers within a resolution cell, the phase variance, i.e. $\sigma_{\phi(t_1,t_2,p)}$ and $\sigma_{\phi(t_1,t_2,q)}$, exponentially decays with time and approaches to the linear decrease with time for point(-wise) scatterers. Rocca (2007) assumed that this motion can be modeled as Brownian motion. Even in the case that there are many sub-scatterers (distributed scatterers) within one resolution cell so that the observed reflectivity is their summation, their PDF is characterized by the same exponential decay with time, provided that each element is affected by independent Brownian motion.

Overall, all the elements in (co)variance matrix contain all errors and are likely to be large numbers, but the arc phase variance $\sigma^2_{u_{\mathrm{DD}}}$ decreases significantly as long as all the elements in the (co)variance have large numbers. In this respect, the precision of estimations improves. In general, there is no a-priori PDF knowledge of $\underline{u}$ under the assumption that the observable is one representation out of the random variables, and the initial (co)variance matrix should be defined at the very beginning by the empirical methods based on the scatterers' signatures.

2.5. Summary

In this chapter we reviewed the traditional InSAR and PSI techniques. We discussed the limitations of InSAR that mainly result from decorrelation and atmospheric inhomogeneities. To overcome these limitations, we resort to the PSI technique which can reduce the influences of temporal and spatial decorrelation, and remove the atmospheric delay signal. The PSI technique only focuses on monitoring the kinematic behavior of the stable point-like scatterers (PS). We introduced the generic PSI processing procedure, and described every component (e.g. height and kinematic time series) that contributes to the PSI functional model. Particularly, for kinematic time series, a linear deformation model as a function of time is normally used and has been successfully applied in many studies (Hooper et al., 2004; van Leijen and Hanssen, 2007; Caro Cuenca, 2012; Chang and Hanssen, 2014). But this assumption cannot be applied to all PS points as some of them may behave nonlinearly in time. Chapter 3 will discuss how to build and decide on the optimal functional model, and evaluate the associated stochastic model. We described the stochastic characteristics of a SAR resolution element, an interferometric resolution element, and an arc phase. The mathematical (functional and stochastic) model will be used in our InSAR applications, as in chapters 4 and 5.

3
Kinematic Time Series Modeling

Perhaps the most relevant component of the InSAR functional model (see chapter 2) is the kinematic component, often referred to as the deformation. The parameterization of the kinematic behavior of InSAR measurement points is the main subject of this chapter. It is standard practice to parameterize the kinematic behavior, in first order, as a linear function of time. This so-called steady-state approach leads to the well-known PSI point maps representing relative deformation velocities. However, it is unlikely that all objects behave in this purely linear way. Ideally, the kinematic parameterization should be optimized for each individual measurement point in the area of interest. We introduce an easily expandable canonical library of kinematic models in section 3.1 and test these against the default linear model. In order to find the most probable kinematic model and assign likelihoods to the results for each point, a probabilistic method based on multiple hypotheses testing and the B-method of testing is proposed, see sections 3.2 – 3.4. The quality of the results and the setting for the test parameters are discussed in section 3.5 and 3.6, followed by the test on a simulated and real data in section 3.7. The method is applied here in a 'post-processing' mode, i.e., it is applied on the final results of PSI processing.

3.1. Kinematic model components

To build the deformation model for InSAR measurements is rather different from the traditional procedure for standard geodetic networks. In the processing of geodetic networks, such as triangulation networks, the mathematical model can be a-priori designed and surveyors can check whether the observations fit to the model (Baarda, 1968, 1976, 1977). If they do not fit, e.g. due to measurement errors, parts of the network can be re-surveyed until the observations fit the predefined model. Besides, for a standard geodetic network with a known mathematical model, all quality metrics are predefined as well, which facilitates the potential rejection of the null hypothesis (Baarda, 1979). For the deformation observations yielded from InSAR processing, where one actually still needs to establish the appropriate mathematical model and the observations are fixed, re-surveying ('going back' in time) is not possible any more (Hanssen and Kampes, 2000; Hanssen, 2001). Therefore, the mathematical model is largely dependent on the observations, thus not predictable, and small changes in the observations may lead to significantly different parameter estimates. In first order approach the observed kinematic, or deformation, phase is usually linked linearly to an unknown constant velocity, as in

$$E\{\phi^k_{\text{defo}}\} = -\frac{4\pi}{\lambda} \cdot t^k \cdot v, \tag{3.1}$$

where t^k is the temporal baseline for the kth epoch w.r.t. the master acquisition and v is the deformation rate. When the deformation includes a non-linear component, ϕ^k_{defo} can be separated into two terms (Ferretti et al., 2000b),

$$E\{\phi^k_{\text{defo}}\} = -\frac{4\pi}{\lambda} \cdot (t^k \cdot v + \mu^k), \tag{3.2}$$

where μ^k represents the residual (non-linear) motion. The term μ^k can be formulated using various functions related to e.g. temperature differences, seasonal changes or abrupt movements due to, e.g., instantaneous events such as earthquakes or construction failures. Moreover, even though it is often conveniently assumed that phase unwrapping is flawless, in reality there are many InSAR points that are still affected by unwrapping errors, which influence the estimated kinematic parameters.

In the following we establish a so-called *library of canonical functions*. These canonical functions serve as basic building-blocks that can be used to build any type of kinematic behavior. As any library, it is easily expandable with new functions, should a certain case-study require this. We prefer physically realistic canonical functions over purely mathematical constructs, such as polynomial functions, which may fit the observed data well, but do not improve insight in the physical behavior of measurement points on Earth. Subsequently, we introduce the canonical functions for the temperature-dependent model, the piecewise linear (breakpoint) model, the exponential model, the (Heaviside) step-function, and the (Kronecker-delta) outlier model.

3.1.1. Temperature-dependent model

A change in temperature may result in a change in volume for buildings and infrastructure. Volume change, known as thermal dilation, causes strain and subsequently deformation. Such deformation, driven by a change in temperature, has been reported in C-band and X-band PSI studies, e.g. by Ferretti et al. (2005), Adam et al. (2008) and Monserrat et al. (2011). Thermal dilation effects are expected to become significant for structures longer than some tens of meters, depending on the materials and the temperature differences (Tipler and Mosca, 2007).

Temperature-correlated effects can be observed for some soil types as well. Warmer periods in summer may lead to lower ground water tables due to increased evaporation, while colder periods in winter cause rising ground water tables (Morishita and Hanssen, 2013, 2015).

It is possible to parameterize these effects in two ways. If temperature records are available for the satellite acquisition times, an (equivalent) thermal expansion coefficient can be estimated, and one parameter would suffice in the model. Without temperature records, one has to rely on sinusoidal functions to describe the behavior, where two or three parameters are needed.

The thermal dilation, ΔL_T, of an object or ground target is proportional to the temperature differences, as in,

$$\mu^k(\eta) = \Delta L_T = \varpi \cdot L_{\text{LOS}} \cdot \Delta T^k = \Delta T^k \cdot \eta, \tag{3.3}$$

where ϖ is the linear expansion coefficient of the material $[K^{-1}]$, and ΔT^k represents the temperature difference between the kth and the reference (or master) acquisition.

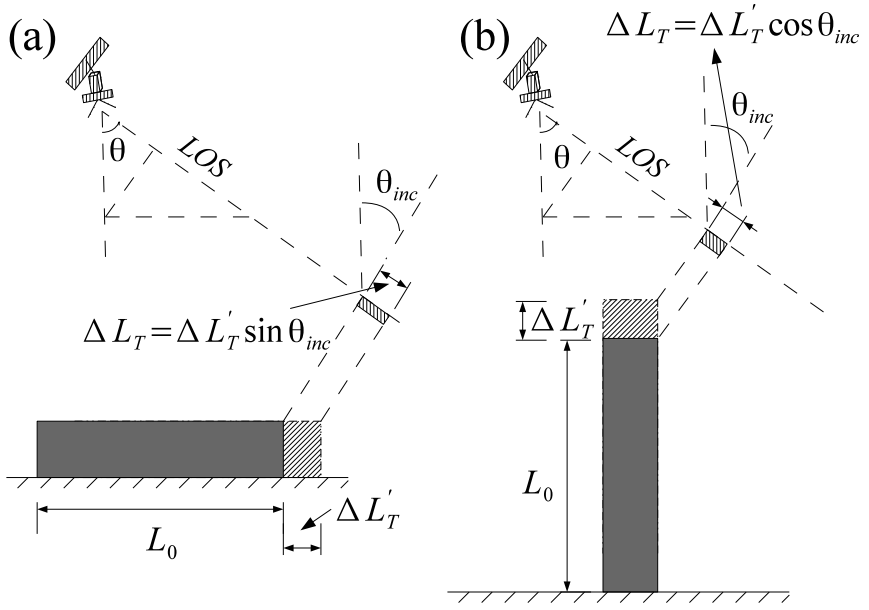

Figure 3.1: Thermal expansion sketch for horizontal expansion/contraction (e.g. an elongated building) (a) and vertical expansion/contraction (e.g. a high-rise building) (b)

A change in temperature ΔT^k leads to a dilation of ΔL_T for an object of length L_{LOS}. The thermal expansion coefficient of the object $\eta = \varpi \cdot L_{\text{LOS}}$ $[m \cdot K]$ where L_{LOS} is the projection of the actual length L_0 in LOS direction. Fig. 3.1 depicts the horizontal and vertical thermal expansion for an elongated and a high-rise building. Suppose a thermal expansion coefficient $\varpi = 1.2 \cdot 10^{-5}$ for steel-reinforced concrete and an annual temperature range of 25 K, a 50 m high building shows a range of about 14 mm of oscillation when observed from an incidence angle of 25 degrees.

When temperature records are not available, a periodic (sinusoidal) function can be considered as a sub-optimal substitute. Though sinusoidal functions are inherently non-linear, they can be re-written in a linear way as (Kampes, 2005; van Leijen and Hanssen, 2008), (cf. appendix B)

$$\mu^k(s,c) = -\frac{4\pi}{\lambda} \cdot (\sin(2\pi t) \cdot s + (\cos(2\pi t) - 1) \cdot c), \tag{3.4}$$

where the coefficients s and c represent the seasonal periodic deformation in LOS direction, with amplitude $A = \sqrt{s^2 + c^2}$, and time offset w.r.t. the master image time $t_0 = -\text{sgn}(c) \cdot \arccos(s/A)/2\pi$. Note that the period of the sinusoidal function is empirically assumed to be one year (to have a complete seasonal cycle). If this assumption cannot be made, the period should be introduced as a third unknown parameter. In contrast to the temperature-dependent model, for which the time lag between a temperature change and the associated deformation of the construction can be short, the

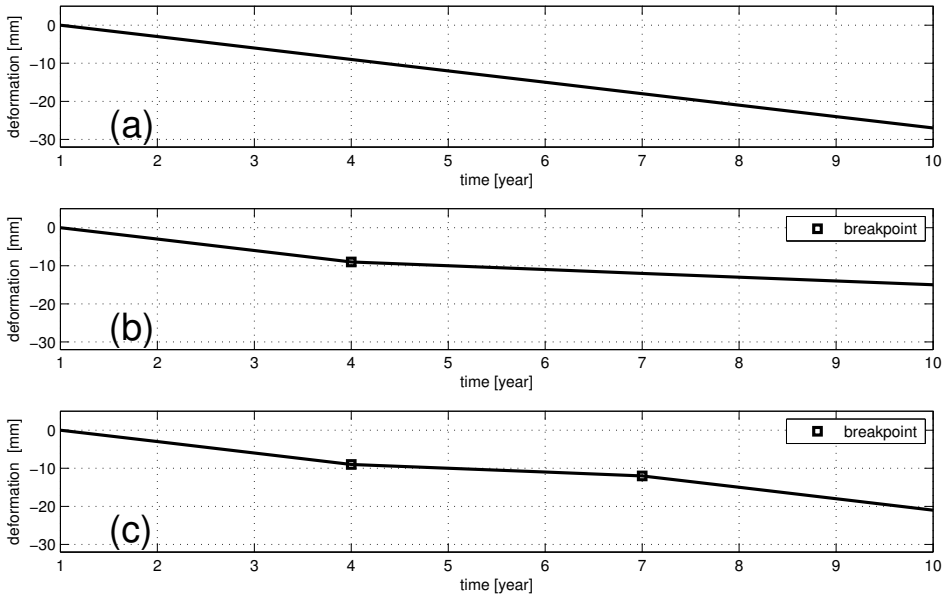

Figure 3.2: Sketch for (a) the linear deformation model, (b) the one breakpoint model, and (c) the double breakpoint model

sinusoidal model would suffice for the deformation caused by the seasonal temperature variation and not the day-to-day variability, which will have a much slower response (or a larger time lag).

3.1.2. Piecewise linear (breakpoint) model

For some cases, e.g. when ground motion is directly coupled to production volumes of water or hydrocarbons, the kinematic behavior should be modeled as a concatenation of several different linear functions for specific time spans (Ketelaar, 2009). Every linear function has a consistent deformation rate in its time span, as in

$$\mu^k(v_k) = t^k \cdot v_k, \tag{3.5}$$

where v_k is the deformation velocity specially for the time t^k. If v_k's are all same, Eq. (3.5) equals to Eq. (3.1), see Fig. 3.2a.

In practice, the single and double break-point models are most common. For instance, one breakpoint can be fixed at the moment of the start of oil or gas extraction, provided that the displacement before and after that moment are both linear. The single break-point model, as shown in Fig. 3.2b, can be expressed as

$$\begin{aligned} \mu^i(v_1) &= t^i \cdot v_1, \quad i \in [1,\ j] \\ \mu^i(v_2) &= t^i \cdot v_2, \quad i \in [j+1,\ K], \end{aligned} \tag{3.6}$$

where v_1 and v_2 are the unknown parameters at the time ranges $[1,\ j]$ and $[j+1,\ K]$, respectively. The temporal location of the breakpoint j can be based on a priori information, or can be found by sequentially evaluating all possible positions.

When the deformation profile can be characterized by three concatenating deformation time spans, the double breakpoint model can be used, shown in Fig. 3.2c, which is expressed as

$$\begin{aligned} \mu^i(v_1) &= t^i \cdot v_1, \quad i \in [1,\ j] \\ \mu^i(v_2) &= t^i \cdot v_2, \quad i \in [j+1,\ k] \\ \mu^i(v_3) &= t^i \cdot v_3, \quad i \in [k+1,\ K], \end{aligned} \tag{3.7}$$

where v_1, v_2 and v_3 are the unknown parameters at the time ranges $[1,\ j]$, $[j+1,\ k]$ and $[k+1,\ K]$. The temporal locations of the breakpoints j and k are either given, or need to be estimated from the data. For instance, in the case of deformation monitoring over a volcano, the temporal behavior for pre-eruption, co-eruption and post-eruption may be varying over every particular phase of the volcanic eruption. The deformation rates for pre-eruption and post-eruption are likely to be smaller than the co-eruptive phase, e.g., Lanari et al. (2010). Based on a priori knowledge about e.g. the date of eruption of a volcano, the three stages can be determined.

3.1.3. Exponential model

For postseismic deformation (relaxation) (Savage et al., 2003), landslides (Montgomery et al., 1998), or soil settlement or compaction (Verruijt and Van Baars, 2007), an exponential kinematic function may be the optimal parameterization,

$$\mu^k(\kappa, \beta) = (1 - \exp(-\frac{t^k}{\beta})) \cdot \kappa, \tag{3.8}$$

where κ scales the function, and the sign determines whether the function is increasing or decreasing. The *characteristic* time β in temporal factor $\exp(-\frac{t^k}{\beta})$ is associated with the decreasing relaxation in time. Fig. 3.3 shows the exponential function graph when $\kappa = [-4,\ -2,\ +2,\ +4]$ and $\beta = [-3,\ -2,\ +2,\ +3]$. When κ and β are both positive or negative, the exponential function has an increasing trend.

The exponential function is non-linear, thereby this function needs to be linearized by a Taylor expansion (Goodwillie, 2003) in order to estimate the parameters (Teunissen, 1989). Such nonlinear least squares estimation is prone to a biased estimation, that is $E\{\underline{\hat{x}}\} \neq x$, when the likelihood of the sum of second- and higher-order terms of Taylor expansion in the nonlinear model is not negligible. Therefore, in some cases, the piecewise linear model can be considered as an alternative approach.

3.1.4. Step model

Under the assumption that the deformation rate is constant and there are only one or more *jumps* occurring due to some instantaneous events, the (Heaviside) step function is introduced. This is a discontinuous function whose value is zero for negative arguments and one for positive arguments, as in (Weisstein, 2008)

$$\mathscr{H}(t - t_{k-1}) = \begin{cases} 0, & t < t_k \\ 1, & t \geq t_k. \end{cases} \tag{3.9}$$

Since $\mathscr{H}(t - t_{k-1})$ can only be either 0 or 1, the Heaviside step function are more or less

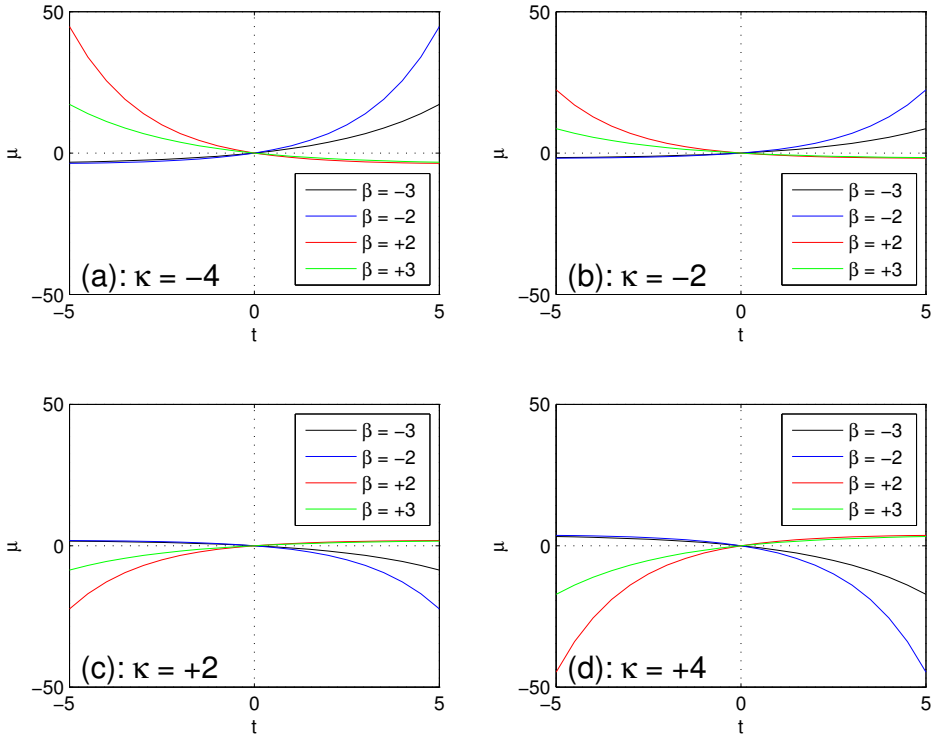

Figure 3.3: Exponential function graph demonstrating the influence of the parameters κ and β in the canonical exponential function, cf. Eq. (3.8), for $\kappa = [-4, -2, +2, +4]$, $\beta = [-3, -2, +2, +3]$ and t is an arbitrary time unit ranging between -5 and 5. As a rule-of-thumb, when κ and β have the same sign, the function is increasing, otherwise decreasing. When both are negative, there is acceleration, while when both are positive, there is deceleration.

considered as scales, the offset needs to be defined for a deformation model, then the Heaviside step model for InSAR is built as

$$\mu^k(\Delta_k, t_k) = \Delta_k \mathscr{H}(t_k - \tau_k), \tag{3.10}$$

where Heaviside step function $\mathscr{H}(t_k - \tau_k)$ is centered at step knot τ_k, The offset Δ_k could occur between $[t_{k-1},\ t_k)$, while τ_k is initialized to be zero. In Fig. 3.4, we show an example for the step function when the offset $\Delta_k = -2$ mm occurs at t_{k-1}. When there are more jumps, at several epochs, the deformation is modeled as a summation of Heaviside step functions, shown as

$$\sum_{k \in I_\Delta} \Delta_k(\mathbf{x}) \mathscr{H}(t - \tau_k(\mathbf{x})) = \Delta_1(\mathbf{x}) \mathscr{H}(t - \tau_1(\mathbf{x})) + \ldots + \Delta_m(\mathbf{x}) \mathscr{H}(t - \tau_m(\mathbf{x})), \tag{3.11}$$

where I_Δ denotes a set of indices of step knots, m is the number of acquisitions. Note that it is impossible to have a step function at every epoch, as this would yield an underdetermined model of observation equations.

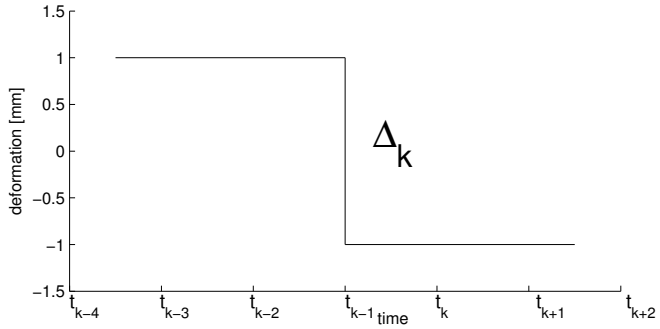

Figure 3.4: Step function for an offset $\Delta_k = -2$ mm at time t_{k-1}

3.1.5. Outlier model

When a single anomalous change/jump is observed in the time series, the Kronecker delta function (Kaplan, 1952) can be used in the mathematical model, shown as

$$\mu^k(D_k) = D_k \cdot \delta_{\mathrm{kl}}, \tag{3.12}$$

where the Kronecker delta $\delta_{\mathrm{kl}} = \begin{cases} 1, & k = l \in [1,\ m] \\ 0, & k \neq l \end{cases}$. D_k represents the offset at the kth acquisition and l represents the time of the offset happens. Note that apart from real 'instantaneous' offsets due to actual physical events, the outlier model will also detect ambiguity errors of an integer amount of phase cycles.

3.1.6. Library of canonical deformation models

Until now, a set of physically realistic models for the non-linear part in Eq. (3.2) has been presented as well as the linear model in Eq. (3.1). In InSAR data processing, the deformation (kinematic) model for every point at position $\mathbf{x} = \mathbf{x}(x, y)$ can be regarded as unique and uncorrelated to other points, even though there are also many deformation phenomena that are strongly correlated in space. We consider these models as canonical functions that fill a library, which can be queried for every point at position $\mathbf{x} = \mathbf{x}(x, y)$

$$\begin{array}{lll} M_1(v(\mathbf{x})) & = t \cdot v(\mathbf{x}), & O(m/2) \\ M_2(\eta(\mathbf{x})) & = \Delta T \cdot \eta(\mathbf{x}), & O(1) \\ M_3(s(\mathbf{x}), c(\mathbf{x})) & = \sin(2\pi t)s(\mathbf{x}) + (\cos(2\pi t) - 1)c(\mathbf{x}), & O(1) \\ M_4(\kappa(\mathbf{x}), \beta(\mathbf{x})) & = (1 - \exp(-\frac{t}{\beta(\mathbf{x})})) \cdot \kappa(\mathbf{x}), & O(1) \\ M_5(D_i(\mathbf{x})) & = D_i(\mathbf{x})\delta_{ij},\ i,\ j \in [1,\ m], & O(m) \\ M_6(\Delta_i(\mathbf{x})) & = \Delta_i(\mathbf{x})\mathscr{H}(t - \tau_i(\mathbf{x})),\ i \in [1,\ m-1], & O(m), \end{array} \tag{3.13}$$

where m is the number of observations (the number of SAR images minus one), and $O(.)$ denotes the order of magnitude. Here the library holds six canonical functions, but this number can be easily extended when other information on the processes is available, or when a specific kinematic signature is searched for. The piece-wise linear model is considered to be a special case for the linear model (M_1). Regarding the temperature-dependent component, one could either use the seasonal-related M_3 (see

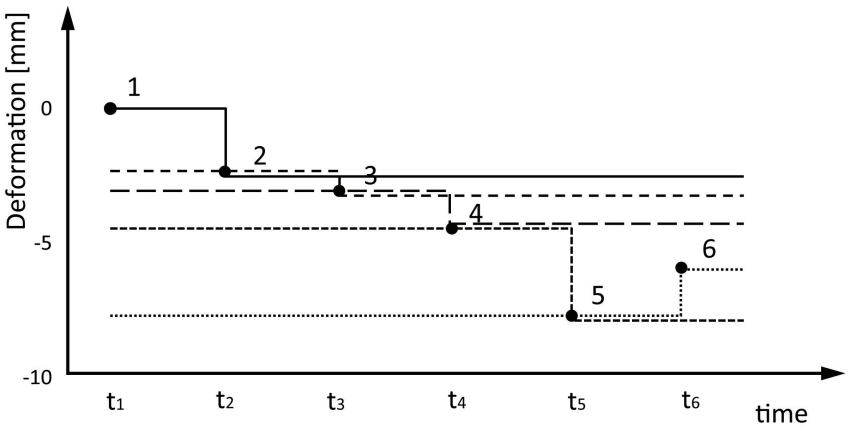

Figure 3.5: Schematic view for evaluating step functions at different epochs. The numbers 1 – 6 indicate the deformation at each epoch. The step knot searching starts from the second acquisition time to the final acquisition time sequentially, marked in different line styles. Every possible step knot location is considered in the testing.

appendix B for its definition) or temperature-related M_2. The library is independent of a specific data set. The most probable deformation model can then be constructed using a combination of the canonical functions. Then the total amount of possible combinations can be easily in the order of hundreds. To determine the most probable model, multiple hypotheses testing will be used. We first set a null hypothesis H_0 and define all possible alternative hypotheses H_j's as

$$\begin{aligned} H_0 &: \quad M_1 \\ H_1 &: \quad M_1 + M_2 \\ &\vdots \quad\quad \vdots \\ H_{m+3} &: \quad M_2 + M_4 + M_5 + M_6 + \ldots + M_{m+3} \\ &\vdots \quad\quad \vdots . \end{aligned} \tag{3.14}$$

Note that for the Kronecker delta function M_5 and Heaviside step function M_6, there could be more than one occurrence in the time series. Theoretically, there could be many. However, with only m observations, it is not possible to test for more than m unknown parameters, practically, there should still be redundancy. For this reason, we only test for one or maximally two Kronecker delta or Heaviside step functions in every time series. To solve the offset D_k and Δ_i, we use an epoch-by-epoch progressive search method. Fig. 3.5 illustrates the search method for one step knot. The step knot is sequentially tested for each epoch except the first acquired time in order to settle the offset's location. This search method works for Kronecker delta model as well.

3.2. Multiple hypotheses testing

Without loss of generality, the mathematical expressions for H_0 and all H_j's, $\forall j$ are expressed as linear systems of observation equations

$$\begin{aligned} H_0: \quad & \underset{m\times 1}{E\{\underline{y}\}} = \underset{m\times n}{A}\,\underset{n\times 1}{x}; && \underset{m\times m}{D\{\underline{y}\}} = \underset{m\times m}{Q_{yy}} = \sigma^2 R_{yy} \\ H_j: \quad & \underset{m\times 1}{E\{\underline{y}\}} = \underset{m\times n}{A}\,\underset{n\times 1}{x} + \underset{m\times q}{C_j}\,\underset{q\times 1}{\nabla_j}, \nabla_j \neq 0; && \underset{m\times m}{D\{\underline{y}\}} = \underset{m\times m}{Q_{yy}} = \sigma^2 R_{yy}, \end{aligned} \tag{3.15}$$

where A is the design matrix, m is the number of observations $\underline{y}$, and x is the unknown vector of parameters. A certain alternative hypothesis is defined by a specification matrix C_j and an additional new vector of unknown parameters ∇_j of length q. The observation equations for H_0 and H_j can be expressed as $H_0: \ \underline{y} = Ax + \underline{e}_0$, and $H_j: \ \underline{y} = Ax + C_j\nabla_j + \underline{e}_j$, respectively. Here $\underline{e}_0$ and $\underline{e}_j$ represent the residuals between the default/alternative model and the observations. The variance of unit weight and the cofactor matrix of the (co)variance matrix Q_{yy} are referred to as σ^2 and R_{yy}, respectively. As $j > 1$ (there may be several, or hundreds, of alternative hypotheses), it is not a binary decision problem (one alternative H_a against one null hypothesis H_0), see appendix A.1, where the rejection of H_0 would directly lead to sustaining H_a at a requested level of significance. As each point may behave in many different ways, requiring a huge amount of alternative hypotheses, the criteria to decide whether to sustain a particular alternative hypothesis will vary for different problems. Consequently, the most probable model can only be found if the appropriate alternative hypothesis is proposed and tested. In other words, if the most probable alternative hypothesis is not part of the test procedure, it cannot be found. Although this statement may sound trivial, it stresses the fact that one should ensure that the functions describing the behavior are included in the canonical library, see section 3.1.6.

In multiple hypotheses testing, the test for every alternative hypothesis follows a test statistic $\underline{T}_q$ with a *Chi-squared* distribution $\chi^2(q,\lambda)$. Here q is the degree of freedom or dimension, which is determined by the number of additional parameters, and λ indicates the level of noncentrality. There may be more than one test statistic that lead to the rejection of H_0 but the most probable model eventually needs to be determined in line with a uniform test criterion.

The test statistics of alternative hypotheses are defined by their dimensions q. Two cases can be distinguished in terms of q: the case of uniform dimension, and the case of nonuniform dimension.

3.2.1. Case 1: Uniform dimension

When all alternative hypotheses have the same dimension, $q_i = q_j, i, j \in [1,\ m-n]$, all their test statistics $\underline{T}^j_{q_j}$'s have a χ^2-distribution with identical q but different noncentrality parameters λ as in

$$H_0: \quad \underline{T}_0 \sim \chi^2(q,0); \qquad H_j: \quad \underline{T}^j_q \sim \chi^2(q,\lambda_j), \forall j, \tag{3.16}$$

where $\lambda_j = \nabla_j^T C_j^T Q_{yy}^{-1} Q_{\hat{e}_0\hat{e}_0} Q_{yy}^{-1} C_j \nabla_j$ and $Q_{\hat{e}_0\hat{e}_0} = Q_{yy} - A(A^T Q_{yy}^{-1} A)^{-1} A^T$. Here $\underline{T}_q^j$ can be generally expressed as (Teunissen et al., 2005)

$$\begin{aligned}\underline{T}_q^j &= \underline{\hat{e}}_0^T Q_{yy}^{-1} \underline{\hat{e}}_0 - \underline{\hat{e}}_j^T Q_{yy}^{-1} \underline{\hat{e}}_j \\ &= \underline{\hat{e}}_0^T \underbrace{Q_{yy}^{-1} C_j (C_j^T Q_{yy}^{-1} Q_{\hat{e}_0\hat{e}_0} Q_{yy}^{-1} C_j)^{-1} C_j^T Q_{yy}^{-1}}_{L^j} \underline{\hat{e}}_0,\end{aligned} \tag{3.17}$$

where $\underline{\hat{e}}_0$ is the residual between the functional model and the observations under the null hypothesis, which is equal to $(I_m - A(A^T Q_{yy}^{-1} A)^{-1} A^T Q_{yy}^{-1})\underline{y} = P_{A_0}^{\perp}\underline{y}$. Note that I_m is the $m \times m$ identity matrix and the matrices $P_{A_0}^{\perp} = I_m - P_{A_0}$ and $P_{A_0} = A(A^T Q_{yy}^{-1} A)^{-1} A^T Q_{yy}^{-1}$, are both orthogonal projectors. We indicate the term $Q_{yy}^{-1} C_j (C_j^T Q_{yy}^{-1} Q_{\hat{e}_0\hat{e}_0} Q_{yy}^{-1} C_j)^{-1} C_j^T Q_{yy}^{-1}$ by the $m \times m$ symmetric matrix L^j. This matrix is special, since it needs to be computed only once for every alternative hypothesis, but then can be used from memory when evaluating every single point. The value for the test statistic $\underline{T}_q^j$ is always non-negative, since $\underline{\hat{e}}_0^T Q_{yy}^{-1} \underline{\hat{e}}_0$ is larger than (or equal to) $\underline{\hat{e}}_j^T Q_{yy}^{-1} \underline{\hat{e}}_j$. (When more additional parameters are added in Eq. (3.15), the model will always fit better to the data, and hence the sum of the squared residues will be smaller). If $\underline{T}_q^j$ is greater than the predefined critical value $\chi_\alpha^2(q,0)$ (given the level of significance α), H_0 will be rejected. A special case of Eq. (3.17) occurs when $q = m - n$. In that case, $\underline{\hat{e}}_j = 0$, since there is no redundancy in the system, and the right hand side of Eq. (3.17) reduces to

$$\underline{T}_{\text{q=m-n}}^j = \underline{\hat{e}}_0^T Q_{yy}^{-1} \underline{\hat{e}}_0, \tag{3.18}$$

which is a general test for the correctness of the null hypothesis, termed the Overall Model Test (also mentioned in appendix A.2). In literature, the test statistic $\underline{T}_{\text{q=m-n}}^j/(m-n)$ is sometimes used instead of $\underline{T}_{\text{q=m-n}}^j$ and denoted as the $\underline{\hat{\sigma}}^2$-test statistic as in

$$\underline{\hat{\sigma}}^2 = \frac{T_{\text{q=m-n}}^j}{m-n} = \frac{\underline{\hat{e}}_0^T R_{yy}^{-1} \underline{\hat{e}}_0}{m-n}, \tag{3.19}$$

where $\underline{\hat{\sigma}}^2$ is an unbiased estimation of the variance of unit weight σ^2 as $E\{\underline{\hat{\sigma}}^2\} = \sigma^2$. The distribution of $\underline{\hat{\sigma}}^2$ under H_0 and H_j is defined as

$$H_0: \quad \underline{\hat{\sigma}}^2 \sim F(m-n, \infty, 0); \qquad H_j: \quad \underline{\hat{\sigma}}^2 \sim F(m-n, \infty, \lambda), \tag{3.20}$$

where $F(m-n,\infty,0)$ is the central F-distribution. Here $E\{\underline{e}_0\} = E\{\underline{e}_j\} = 0$ causes the infinity for the second parameter of the F-distribution.

Another special case is the w-test when all tests are one dimensional ($q = 1$). Conventionally, this is widely used in geodesy to test for the presence of one or more blunders in the observations or the model misspecifications for H_0. In InSAR, however, there are no manual observations, and therefore 'blunders' are not possible. Nevertheless, it is possible that e.g. a phase unwrapping error occurs in one observation. In this case, the w-test can be used. The corresponding test statistic $\underline{T}_{q=1}^j$ is given by

$$\underline{T}_{q=1}^j = \frac{(c_j^T Q_{yy}^{-1} \underline{\hat{e}}_0)^2}{c_j^T Q_{yy}^{-1} Q_{\hat{e}_0\hat{e}_0} Q_{yy}^{-1} c_j}, \tag{3.21}$$

here the $m \times q$ matrix C_j is reduced to the $m \times 1$ vector c_j. When the (co)variance matrix Q_{yy} is diagonal and c_j is formed by a canonical unit vector, Eq. (3.21) simplifies to

$$\underline{T}^j_{q=1} = \frac{\hat{\underline{e}}_i}{\sigma_{\hat{e}_i}}, \tag{3.22}$$

which equals the residual of the ith observation divided by its standard deviation. If this test is subsequently evaluated for every observation, we refer to this testing sequence as *data snooping*.

Finally, to determine the best hypothesis from the library when the dimensions are all $q = q_B$ for instance, the best alternative hypothesis H_B is chosen based on the following inequality,

$$\underline{T}^B_{q_B} > \underline{T}^j_{q_B}, \ \forall j. \tag{3.23}$$

When $\underline{T}^B_{q_B}$ is the largest one among all the others, H_B is the best alternative model.

3.2.2. Case 2: Nonuniform dimension

A situation in which all possible alternative hypotheses have the same dimension would be rare in reality. The most common situation is that alternative hypotheses have different dimensions, i.e. $q_i \neq q_j, i, j \in [1, m-n]$. In this case, the criterion of Eq. (3.23) fails to determine the optimal alternative hypothesis, since the test statistics χ^2 have different distributions (cf. Fig. 3.6a). A way to normalize the test statistic is to divide it by its critical value $\chi^2_{\alpha_j}(q_j)$, with a specific level of significance α_j and a known Q_{yy}, expressed as a ratio (de Heus et al., 1994)

$$\underline{\mathbf{T}}^j_{q_j} = \underline{T}^j_{q_j} / \chi^2_{\alpha_j}(q_j). \tag{3.24}$$

Whenever the ratio $\underline{\mathbf{T}}^j_{q_j} > 1$, $\underline{T}^j_{q_j}$ exceeds the critical value and subsequently the null hypothesis H_0 will be rejected. When the ratio $\underline{\mathbf{T}}^j_{q_j} \leq 1$, alternative hypothesis H_j is not more probable than the null hypothesis H_0 and thus discarded.

The probability density function of the test ratio with different degrees of freedom ($q = 1,2,3,4$), given $\alpha = 1\%$ and $\alpha = 10\%$, is shown in Figs. 3.6b and 3.6c, respectively. These curves stem from the fact that the χ^2-distribution is a special case of the Gamma distribution (Γ-distribution), i.e., the distribution $\underline{T}_q \sim \chi^2(q,0)$ is equal to the distribution $\underline{T}_q \sim \Gamma(q/2, 1/2)$. This implies that the multiplication of $\underline{T} \sim \chi^2(q,0)$ with a factor $C = 1/\chi^2_\alpha(q) > 0$, yields the Gamma function $\underline{\mathbf{T}}_q = C\underline{T} \sim \Gamma(q/2, 2C)$ (Davis, 1970; Abramowitz and Stegun, 1970). Note that, cf. Figs. 3.6b and 3.6c, for increasing α, the intersection of different PDFs shifts to the right, possibly beyond the value one.

3.3. The B-method of testing

The critical value $\chi^2_{\alpha_j}(q_j)$ in Eq. (3.24) depends on the choice of the level of significance α_j and the dimension q_j. The level of significance refers to the Type-I error: the rejection of H_0 when in fact H_0 is true (Teunissen, 2003). However, when the aim is to compare different alternative hypotheses, we want to make sure that the probability

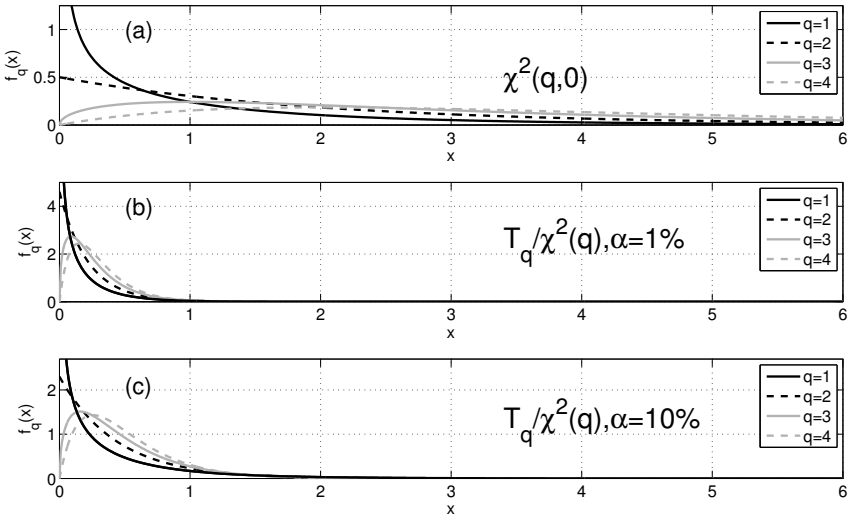

Figure 3.6: Central χ^2-distribution (a), and the probability density function of the test ratio $\underline{T}_q/\chi^2_\alpha(q)$ (b) and (c), with the different dimensions (or the degrees of freedom): $q = 1, 2, 3, 4$.

of accepting a particular alternative hypothesis, knowing that it is true, is identical for any alternative hypothesis. This probability is commonly referred to as the power, γ, of the test. The essence of the B-method of testing (Baarda, 1968) is to fix the (reference) power of the test γ_0, and calculate the (reference) noncentrality parameter λ_0, given the level of significance α_j and the dimension q_j, as in

$$\lambda_0 = \lambda(\gamma_0, \alpha_j, q_j), \forall j. \tag{3.25}$$

Thus, the constant values for the noncentrality parameter λ_0 and the power γ_0 for all tests assure that any particular alternative hypothesis H_j can be selected with the same probability, irrespective its dimension q_j.

Furthermore, we can determine the minimal absolute value $|\nabla_j|$ (details in section 3.5) to make the additional parameter vector ∇_j detectable, with a discriminatory power γ. This value is found via the concept of *internal reliability* for a given level of significance α, power γ and the dimension q by

$$\nabla^T C^T Q_{yy}^{-1} Q_{\hat{e}_0 \hat{e}_0} Q_{yy}^{-1} C \nabla = \underset{1\times 1}{\lambda}(\gamma, \alpha, q). \tag{3.26}$$

If the new parameter vector ∇ is known, the discriminatory power (power of test) γ can be computed straightforwardly via the noncentrality parameter λ. Since the power γ is the likelihood of correctly rejecting H_0 in favor of H_j, a large value for ∇ yields a large power, making it easy to detect, while a small value for ∇ yields a low discriminatory power.

For InSAR deformation modeling, the objective is to compare various alternative hypotheses H_j, with the same discriminatory power γ. Once $\gamma = \gamma_0$ and α_0 is fixed, the corresponding noncentrality parameter $\lambda_0 = \lambda(\alpha_0, q, \gamma_0)$ can be obtained for a certain

dimension q. Such test statistic ratio can be performed for all hypotheses, and the most probable (or optimal) alternative hypothesis is assumed to reject H_0 most strongly and has the largest ratio value. In other words, H_B is the most probable alternative hypothesis if and only if

$$\underline{\mathbf{T}}^B_{q_B} = \max_j \{\underline{\mathbf{T}}^j_{q_j}\}. \tag{3.27}$$

3.4. Detection-Identification-Adaptation (DIA) procedure

To enable multiple hypotheses testing, the Detection-Identification-Adaptation (DIA) procedure (Teunissen, 1990) is applied. The formulation of the DIA procedure consists of:

1. Detection: Determine whether the default 'steady state' deformation model H_0 can be sustained or not.

   As the first phase of the DIA procedure, the Overall Model Test (OMT) Eq. (3.18) is applied on the null hypothesis H_0 of 'steady-state mode' (constant velocity). The specification matrix C_j is not taken into account since the model misspecifications or observation outliers are still unknown. The OMT is to detect possible disturbances, errors, and anomalies in the observed data for the null hypothesis, and consequently decide to either sustain or reject the null hypothesis. However, in case of rejection, the OMT cannot determine its cause.

2. Identification for the optimal model

   Rejection can be the result of large observation errors, an inappropriate functional model, or poor specification of the observations' noise signature in the stochastic model Q_{yy}. A physically realistic alternative parameterization of the kinematic behavior can be designed. A-priori information on the problem at hand, or a flexible and expandable library of model functions can be used to build many alternative functional models, to later decide on the most probable alternative model by searching the maximum test ratio as in Eq. (3.24).

   As Eq. (3.24) includes the (co)variance matrix Q_{yy}, one needs to know the stochastic model of the observations. In practice, however, incomplete knowledge of the stochastic model $D\{\underline{y}\} = Q_{yy}$ of the observation occurs in most cases. Therefore, if no other information is available, we start to build the covariance matrix Q_{yy} with a simple model consisting of a variance of unit weight σ^2 and cofactor matrix R_{yy}=I. Fig. 3.7a shows the relationship between temporal coherence γ and the standard deviation σ based on Eq. (2.33) (multi-look $L = 1$), for pointwise coherent points. Since the temporal coherence can be computed by

$$|\hat{\gamma}| = \frac{|\sum_{i=1}^m \underline{Y}^{(i)} \cdot \underline{\hat{Y}}^{(i)*}|}{\sqrt{\sum_{i=1}^m |\underline{Y}^{(i)}|^2 \sum_{i=1}^m |\underline{\hat{Y}}^{(i)*}|^2}}, \tag{3.28}$$

   where $\underline{Y}^{(i)} = \exp(-j\underline{y}^{(i)})$, $\underline{y}^{(i)}$ is the ith observation in radians, i.e. the deformation in the i epoch. The adjusted observation $\underline{\hat{y}}^{(i)}$ is the ith estimation based on

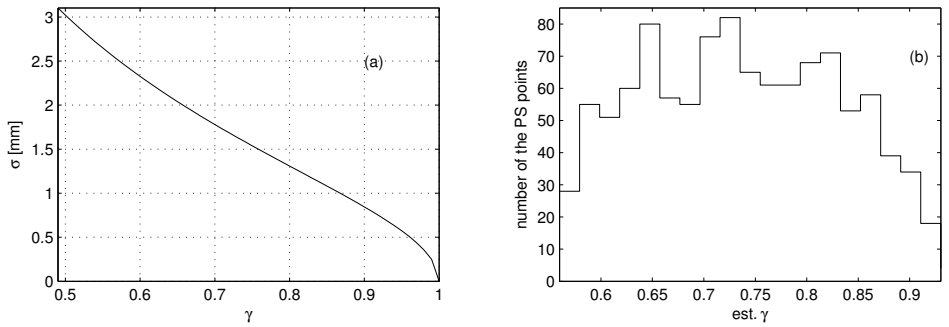

Figure 3.7: (a) The relationship between temporal coherence γ and the standard deviation σ based on Eq. (2.33). (b) The histogram of the estimated temporal coherence distribution for 1076 PS points derived from 127 TerraSAR-X data acquisitions.

the 'steady-state mode' model. Fig. 3.7b shows, as an example, the histogram of the estimated temporal coherence distribution for 1076 PS points derived from 127 TerraSAR-X acquisitions (acquired between April 2009 and June 2013). It shows that the temporal coherence of most of these PS points is larger than 0.55. Therefore, σ can be fixed as 2.5 mm or even a smaller value.

More precisely, when other information is available, the (co)variance matrix Q_{yy} can be decomposed as (Teunissen, 1988; Kenselaar, 1997; Amiri-Simkooei et al., 2007; Teunissen and Amiri-Simkooei, 2008)

$$Q_{\mathrm{yy}} = \sum_{k=1}^{p} \sigma_k^2 Q_k, \tag{3.29}$$

where Q_k are the cofactor matrices for the decomposition of R_{yy}. To derive a realistic (co)variance matrix Q_{yy}, the variance components $\underline{\hat{\sigma}}_k$ are estimated by the variance component estimation (VCE), as in

$$\underline{\hat{\sigma}}_k = N^{-1} l, \tag{3.30}$$

where

$$\begin{aligned} N_{\mathrm{kl}} &= \mathrm{tr}(Q_{\mathrm{yy}}^{-1} P_A^{\perp} Q_k P_A^{\perp} Q_l); \\ l_k &= \underline{\hat{e}}^T Q_{\mathrm{yy}}^{-1} Q_k Q_{\mathrm{yy}}^{-1} \underline{\hat{e}}, \end{aligned} \tag{3.31}$$

here k and l represent the index for the kth row and lth column variance factor. Again the orthogonal projector $P_A^{\perp} = I - A(A^T Q_{\mathrm{yy}}^{-1} A)^{-1} A^T Q_{\mathrm{yy}}^{-1}$, and $\underline{\hat{e}} = P_A^{\perp} \underline{y}$. According to the propagation law of variances and covariances, the precision of the VCE reads,

$$Q_{\hat{\sigma}} = N^{-1}. \tag{3.32}$$

Once the posterior variance is obtained, one could compare it with the a-priori variance to check whether the scalar of stochastic model is improved or not.

3. Adaptation: estimation and evaluation

If the test statistics of several alternative hypotheses are larger than their critical values, they are considered as potential optimal hypothesis candidates. To determine which alternative is the most probable one, Eq. (3.23) or Eq. (3.27) is used. In this phase, one needs to compute the critical value $\chi^2_{\alpha_j}(q_j)$ in Eq. (3.27) for a chosen α_j and a given q_j. According to the B-method of testing (Baarda, 1968), the necessary condition for this method is to fix the reference power of test γ_0, and then to calculate the reference noncentrality parameter λ_0 which is dependent on the reference power of test γ_0, the level of significance α and the dimension q, see Eq. (3.25). The choice of constant values for the noncentrality parameter λ_0 and power of test γ_0 in all the tests shows that a certain alternative model can be found with the same probability when $q = m - n$, $q = 1$, or all values in between.

The most probable model results, e.g. $\hat{x}$ and $\hat{\nabla}$, can be estimated by best linear unbiased estimation (BLUE), and the corresponding model errors, or model misspecifications $\nabla_y = C\hat{\nabla}$ with the quadratic form in Eq. (3.26) can be computed as well. In the following we will discuss the quality in terms of its precision and reliability.

3.5. Quality control

We have presented the theory and the processing procedure for statistical hypothesis testing to decide on the best mathematical model and parameterization. Theoretically, a functional model with more unknown parameters will fit the observations better. For instance, a piecewise polynomial with a high degree would coincide very well with the observations in most cases. However, the measurements cannot be purely signal without any noise. If the default model with a relatively small number of unknowns can still describe the observations well enough, with an acceptable level of noise, we could still hold this null hypothesis, cf. appendix A.3. To validate the results, the quality of results is discussed in this section.

3.5.1. Precision

Once the unknown parameters are estimated, the quality in terms of precision and reliability is taken into consideration. Per model, the precision of the estimated parameters is given by

$$Q_{\hat{x}\hat{x}} = N^{-1} = (A^T Q_{yy}^{-1} A)^{-1}. \tag{3.33}$$

This precision indicator $Q_{\hat{x}\hat{x}}$ relies on the chosen basis (or the reference point) in terms of the S-basis (Baarda, 1981), which can be compared with a predefined criterion precision $\mathbb{H}_{xx}$ (symmetric and positive definite matrix). This criterion matrix $\mathbb{H}_{xx}$ is filled with the values derived from a suitable (co)variance function, usually in a simple structure, e.g. a diagonal matrix, or even a scaled identity matrix.

The estimated precision of the parameters $Q_{\hat{x}\hat{x}}$, satisfies the criterion precision if and only if

$$\underset{n\times n}{Q_{\hat{x}\hat{x}}} \leq \underset{n\times n}{\mathbb{H}_{xx}}. \tag{3.34}$$

Both matrices should be defined w.r.t. the same S-basis. To check whether both matrices have the same S-basis, Eq. (3.34) can be cast in a generalized eigenvalue problem,

$$|Q_{\hat{x}\hat{x}} - \zeta \mathbb{H}_{xx}| = 0, \tag{3.35}$$

where $|.|$ denotes the determinant and the eigenvalue ζ scales $\mathbb{H}_{xx}$. When the two matrices, $Q_{\hat{x}\hat{x}}$ and $\mathbb{H}_{xx}$, are identical, the eigenvalue is equal to one. If the eigenvalue is smaller than one, the precision is better than required. If the eigenvalue is larger than one, the precision is worse than required. Hence, the minimal eigenvalue $\zeta_{\min}$ represents the best precision and the maximum eigenvalue $\zeta_{\max}$ corresponds to the estimated parameters with the worst precision. The latter is considered as a metric for the global precision. In this case, $\zeta_{\max}$ is independent of the chosen S-basis, which is a useful property.

Once $Q_{\hat{x}\hat{x}}$ is obtained, the precision of the adjusted observables then reads

$$Q_{\hat{y}\hat{y}} = A Q_{\hat{x}\hat{x}} A^T, \tag{3.36}$$

and the precision of the least-squares (LSQ) corrections is

$$Q_{\hat{e}\hat{e}} = Q_{yy} - Q_{\hat{y}\hat{y}}, \tag{3.37}$$

where the residual $\underline{\hat{e}} = \underline{y} - \underline{\hat{y}}$ and $\underline{\hat{y}} = A\underline{\hat{x}}$.

3.5.2. Reliability

The concept of reliability is always related to statistical testing theory. It is used as a metric to describe a model misspecification (for example an additional parameter ∇ that should be included in the functional model), that can be detected with a probability γ. Thus, a description of reliability is always related to a specific alternative hypothesis.

The mathematical model for alternative hypothesis H_j is expressed as

$$H_j: \quad \underset{m\times 1}{E\{\underline{y}\}} = \underset{m\times n}{A}\,\underset{n\times 1}{x} + \underset{m\times q}{C}\,\underset{q\times 1}{\nabla}, \ \underset{q\times 1}{\nabla} \neq 0; \quad \underset{m\times m}{D\{\underline{y}\}} = \underset{m\times m}{Q_{yy}}, \tag{3.38}$$

where ∇ is the vector of additional (deformation) parameters. For example, if the steady-state model under the null hypothesis would need to be extended by a temperature-dependent parameter η, cf. Eq. (3.3), then $\nabla = \eta$ is a 1×1 vector expressing this 'additional' parameter.

In this context, an important value to consider is the minimal (absolute) value that this additional parameter should have, to be detectable with a probability γ. This γ is the discriminatory power, see section 3.3. We refer to this value as the *Minimal Detectable Value* (MDV) for parameter ∇. In our example, the MDV[1] of the temperature-dependent parameter η is $|\nabla_{\text{MDV}}|$. If the true (but unknown) value of the temperature-dependent parameter η is equal to $|\nabla_{\text{MDV}}|$, we can state that it will be detectable with

[1] It should be noted that the MDV is known in conventional geodetic literature as the Minimal Detectable Bias (MDB), or the threshold at which errors in the observations can be detected. In our discussion, we do not regard the alternative hypothesis as identifying errors in the observations, but as a model misspecification: there needs to be an extension of the model under the null hypothesis with additional parameters added.

discriminatory power γ, when this is assessed in a test with significance level α and dimension q. In this case, since we have only one additional parameter, $q = 1$. Note that if the true value of η is greater than $|\nabla_{\text{MDV}}|$, we will detect it with a greater discriminatory power. Likewise, if the true value of η is smaller than $|\nabla_{\text{MDV}}|$, we may still detect it, but at a smaller discriminatory power.

Viewed from another perspective, if we set the discriminatory power γ to a high value, we will only detect a temperature-dependent component in our data if its value is high.

The MDV is found via the concept of internal reliability for a given significance level α, power γ and the dimension q by

$$\nabla^T C^T Q_{yy}^{-1} Q_{\underline{\hat{e}}_0 \underline{\hat{e}}_0} Q_{yy}^{-1} C \nabla = \underset{1\times 1}{\lambda}(\gamma, \alpha, q), \tag{3.39}$$

where ∇ is a new unknown vector of parameters similar to x. It is also deterministic (non-stochastic) and therefore it has a particular value. If this new parameter vector ∇ is known, the power γ (via the noncentrality parameter λ) with which it would be found in a statistical test could be computed straightforwardly. This will be discussed in sections 3.5.3 and 3.5.4.

3.5.3. 1-dimensional alternative hypothesis

The 1-dimensional alternative hypothesis $q = 1$ can be formulated as

$$H_j: \quad \underset{m\times 1}{E\{\underline{y}\}} = \underset{m\times n}{A}\underset{n\times 1}{x} + \underset{m\times 1}{c}\underset{1\times 1}{\nabla}, \underset{1\times 1}{\nabla} \neq 0; \quad \underset{m\times m}{D\{\underline{y}\}} = \underset{m\times m}{Q_{yy}}, \tag{3.40}$$

where the specification matrix C as in Eq. (3.15) reduces to a column vector c as ∇ is a scalar. Assuming that the value of ∇ is known, the noncentrality parameter is

$$\nabla^T c^T Q_{yy}^{-1} Q_{\underline{\hat{e}}_0 \underline{\hat{e}}_0} Q_{yy}^{-1} c \nabla = \underset{1\times 1}{\lambda}(\gamma_0, \alpha_0, q = 1), \tag{3.41}$$

and consequently the MDV for ∇ is

$$\underset{1\times 1}{|\nabla_{\text{MDV}}|} = \sqrt{\frac{\lambda_0}{c^T Q_{yy}^{-1} Q_{\underline{\hat{e}}_0 \underline{\hat{e}}_0} Q_{yy}^{-1} c}}. \tag{3.42}$$

The influence of the MDV on the observations is computed by $\nabla_y = c\nabla$. After computing the effect of the MDV on the observations ∇_y, the corresponding effect on the initially estimated parameter $\hat{x}$ can be computed as well,

$$\nabla_{\hat{x}} = (A^T Q_{yy}^{-1} A)^{-1} A^T Q_{yy}^{-1} \nabla_y, \tag{3.43}$$

which is called the *external reliability*, which defines the influence of an additional parameter on the estimation $\hat{x}$. Thus $\nabla_{\hat{x}}$ can be interpreted as a bias on the parameter estimation $\hat{x}_0$, $\nabla_{\hat{x}} = E\{\underline{\hat{x}}_0 | H_j\} - E\{\underline{\hat{x}}_0 | H_0\}$. For instance, if the alternative hypothesis H_j is a model superimposed on the linear model M_1, a temperature-dependent model M_2, then $\nabla_{\hat{x}}$ shows how much the velocity estimate would change due to extra temperature-dependent components.

With the precision estimation $Q_{\hat{x}\hat{x}}$ and the external reliability estimate $\nabla_{\hat{x}}$, one can relate to a scalar metric that is the bias to noise ratio,

$$\sqrt{\lambda_{\hat{x}}} = \sqrt{\nabla_{\hat{x}}^T Q_{\hat{x}\hat{x}}^{-1} \nabla_{\hat{x}}}. \tag{3.44}$$

This equation indicates that the impact of ∇_y on the parameter estimation $\hat{x}_0$ under H_0 is significant when $\sqrt{\lambda_{\hat{x}}}$ is large, and vice versa.

3.5.4. q-dimensional alternative hypothesis

When more than one additional unknown ($q > 1$) are introduced, ∇ becomes a vector instead of a scalar as for the $q = 1$ case. It implies that a scalar MDV equation (see Eq. (3.42)) cannot be used any more. This problem can be solved by reparametrization of ∇ as in (Teunissen, 2000)

$$\underset{q\times 1}{\nabla} = \underset{1\times 1}{\|\nabla\|} \cdot \underset{q\times 1}{d}, \tag{3.45}$$

where $\|\nabla\|$ is the length of vector ∇ and d is a unit vector which varies in all directions, e.g. when $q = 2$, the end point of the vector d could move along a unit circle. Then the equivalence of Eq. (3.42) reads

$$H_j: \quad \underset{m\times 1}{E\{\underline{y}\}} = \underset{m\times n}{A}\underset{n\times 1}{x} + \underset{m\times q}{C}\underset{1\times 1}{\|\nabla\|} \cdot \underset{q\times 1}{d}, \quad D\{\underline{y}\} = \underset{m\times m}{Q_{yy}}. \tag{3.46}$$

Now the noncentrality relation to the MDV is

$$\nabla^T C^T Q_{yy}^{-1} Q_{\underline{\hat{e}}_0\underline{\hat{e}}_0} Q_{yy}^{-1} C\nabla = \|\nabla\| \cdot d^T C^T Q_{yy}^{-1} Q_{\underline{\hat{e}}_0\underline{\hat{e}}_0} Q_{yy}^{-1} Cd \cdot \|\nabla\| = \underset{1\times 1}{\lambda}(\gamma_0, \alpha_0, q), \tag{3.47}$$

or

$$\|\nabla_{\underset{1\times 1}{\mathrm{MDV}}}\| = \sqrt{\frac{\lambda_0}{d^T C^T Q_{yy}^{-1} Q_{\underline{\hat{e}}_0\underline{\hat{e}}_0} Q_{yy}^{-1} Cd}}. \tag{3.48}$$

Let d move through an unit (hyper)sphere, such as a circle when $q = 2$, a sphere when $q = 3$, or a hypersphere when $q > 3$, the vector ∇ will move through a (hyper)ellipsoid as described by λ_0. Note that all the aforementioned computations, i.e. $Q_{\hat{x}\hat{x}}$, $\mathbb{H}_{xx}$, $\zeta_{\max}$, the MDV for a given α_0 and γ_0, and the external reliability $\nabla_{\hat{x}}$ or the bias $\nabla_{\hat{x}}$, can be performed without actual observations, both for the precision as well as for the reliability computations. In other words, all computations can be performed as long as the functional and stochastic model are predefined.

3.6. Choice for the parameters α and γ

In testing theory, a null hypothesis H_0 will be rejected in favor of a specific alternative hypothesis H_j, if the calculated test statistic $\underline{T}_q^j$ is greater than a predefined critical value $\chi_\alpha^2(q,0)$. This critical value follows from the probability distribution of that test statistic and an appropriate choice for the level of significance α. However, for deformation analysis of SAR data, the conventional choice for α is not always the most appropriate. Therefore this section presents the method to define the proper values for the level of significance α and the discriminatory power γ to obtain the most probable model.

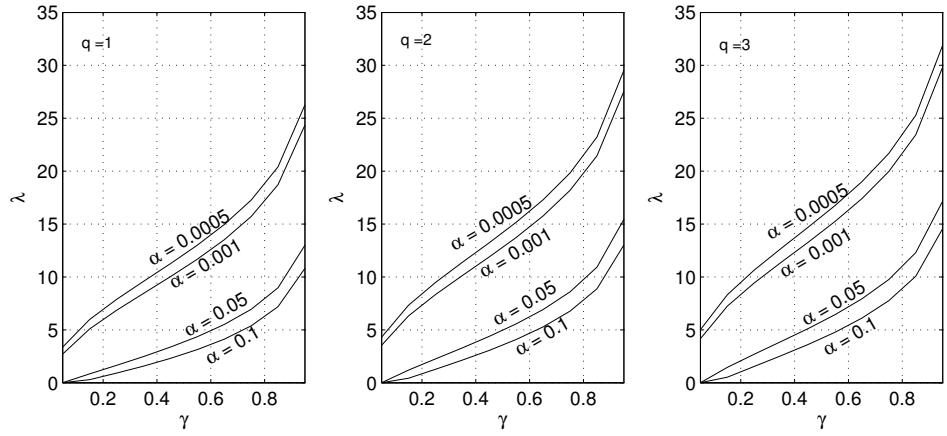

Figure 3.8: The relation between γ and λ when α and q are fixed.

3.6.1. Definition of the parameters α and γ

If one has defined the level of significance α based on a given critical value $\chi^2_\alpha(q,0)$, the size α of the test can be derived directly from

$$\alpha = \int_{\chi^2_\alpha(q,0)} f_{\underline{y}}(y|H_0)\,d_y, \tag{3.49}$$

where $f_{\underline{y}}(y|H_0)$ denotes the PDF of measurements $\underline{y}$ under the null hypothesis H_0. With a fixed α, the probability, β, of falsely rejecting different alternative hypotheses H_j's is varying in terms of the dimensions q_j's, and their noncentrality parameters λ_j. To compute the probability of a correct decision of the test, the discriminatory power $\gamma = 1-\beta$ is used, which is defined as

$$\gamma = \int_{\chi^2_\alpha(q,0)} f_{\underline{y}}(y|H_j)\,d_y. \tag{3.50}$$

With α and q known or fixed, the power γ is only a function of the noncentrality parameter λ, as in

$$\gamma = \gamma(\alpha, q, \lambda) = \gamma_{\alpha,q}(\lambda). \tag{3.51}$$

This relation between λ and γ is shown in Fig. 3.8. It shows that given fixed α, when the degree of freedom q increases, λ increases, and therefore γ increases.

3.6.2. Choice of the test parameters for InSAR time series

In standard geodetic observations, α is empirically considered to be small, e.g. α = 0.1% (Baarda et al., 1967). This stems from the fact that a smaller α would have the lower probability of wrongly rejecting the null hypothesis H_0, if it is in fact true. If H_0 is rejected, the standard action is to re-measure that part of the network. Since re-measuring is laborious and expensive, one prefers to have α small, α = 0.1% means that only one in a thousand measurements needs to be resurveyed.

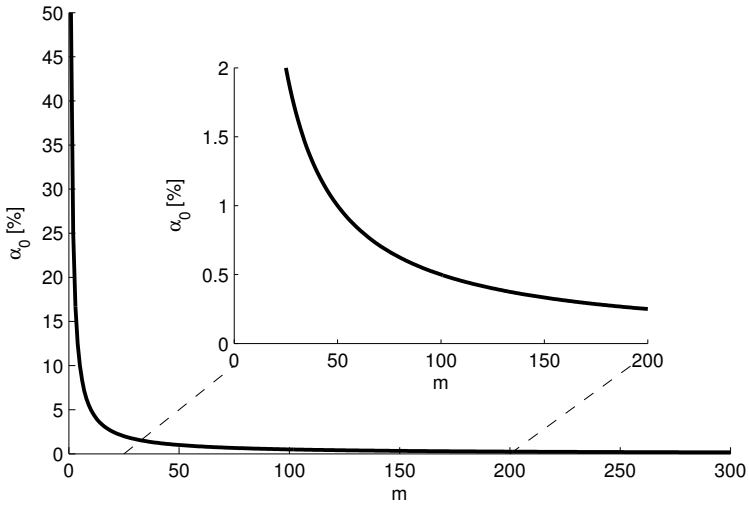

Figure 3.9: The values of the level of significance α_0 when $\alpha_0 = 1/(2m)$, m represents the number of observations.

In deformation monitoring using InSAR data, H_0 is the 'steady-state mode' model and the erroneous rejection of H_0 is not costly, it is only computationally time consuming. However, the concern is that the introduction of extensive and difficult alternative models is not needed, if they are not physically realistic. Besides, following Ockham's razor[2], as long as a signal description via the null hypothesis is reasonable enough, more difficult parameters should be not introduced. For this reason, α is set to a small value as well.

The B-method of testing requires input values for the level of significance, α, and the power of the test, γ_0, see section 3.3. To be able to select from different models with the same discriminatory power, particularly when these models have different degrees of freedom, α will need to be tuned. For initializating α, we use the $M_5(D_k(\mathbf{x}))$ model with one outlier as a 'reference' alternative hypothesis. As a heuristic rule, we choose $\alpha_0 = 1/(2m)$, related to the number of observations m, following de Heus et al. (1994). For InSAR time series, this rule of thumb typically yields $0.2\% < \alpha_0 < 2\%$, see Fig. 3.9. Fig. 3.10 shows that the coupling of α_0 ($q = 1$), for the conventional alternative hypothesis, with α_G for the Global (Overall Model, $q = m - n$) test, using Eq. (3.25), yields values for α_G around 30%, for $25 < m < 200$. This rather large level of significance of 30% can be interpreted as the amount of times in which we engage in testing alternative hypotheses, even though H_0 is actually valid. We do not consider this to be a big problem, since in the testing, alternative models will not necessarily yield a better fit. A greater value for α_G does result in a higher computational burden though.

Choosing a large discriminatory power, e.g. $\gamma_0 = 80\%$, implies that an additional parameter $|\nabla_j|$, for example temperature-dependent parameter η, would need to be large

[2]Ockham's razor (Jefferys and Berger, 1992) states that among competing hypotheses, the hypothesis with the fewest parameters that still explains the observations equally well, should be preferred.

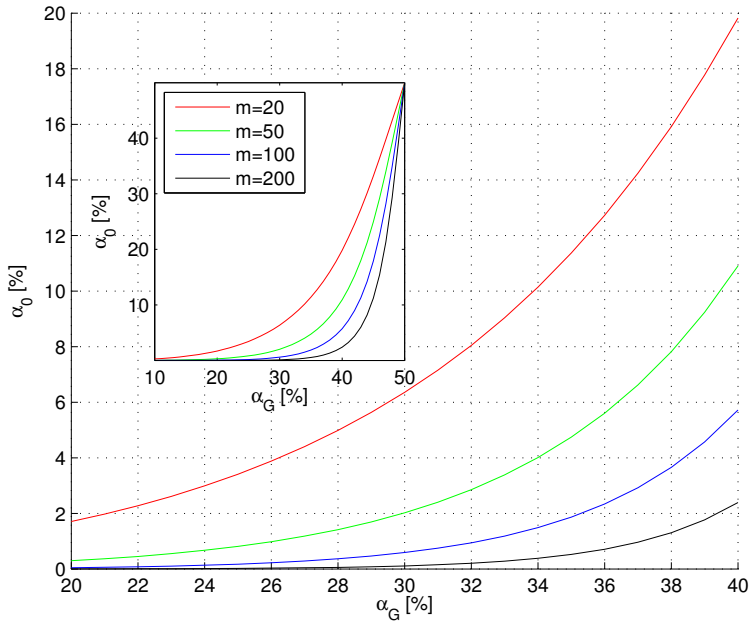

Figure 3.10: The relationship between the levels of significance α_G ($q = m - n$) and α_0 ($q = 1$). The number of observations is denoted by m. By choosing a relatively high value of α_G, e.g., around 30%, we require the α_0 values to be between 0.2 and 2%.

in order to be detected. A smaller value would then be detected with a smaller likelihood, see Fig. 3.11. In principle, when comparing different alternative hypotheses, the value for γ_0 is not that important. Here we choose $\gamma_0 = 50\%$, which can be interpreted as the size of an additional parameter that would just lead to either the rejection or the acceptance of H_0.

Given $\alpha_0 = 1/(2m)$, $\gamma_0 = 50\%$ and $q = 1$, we then use Eq. (3.25) to compute λ_0, and invert this again with $q = m - n$ to find the corresponding α_G for the overall model test. When $m - n$ is a large number, α_G will be a large value as well.

3.7. Procedure for kinematic analysis of InSAR time series

With fixed test parameters, the MHT approach can be performed on any kinematic time series. Per point at position $\mathbf{x} = \mathbf{x}(x, y)$, the null hypothesis (steady-state) and all alternative hypotheses consisting of various model combinations can be expressed in a binary table, see Tab. 3.1. Seven alternative hypotheses are listed, while the total amount of alternatives, J, is much more than seven since the offset $\Delta_i(\mathbf{x})$ may happen at any epoch and is evaluated for all epochs. Different combinations for the canonical functions form different alternative hypotheses, for instance, the functional model of H_1 is the sum of model $M_1(\nu(\mathbf{x}))$ and $M_2(\eta(\mathbf{x}))$, with one degree of freedom.

In the following, we describe the generic procedure for applying statistical testing for the kinematic analysis of InSAR time series, see also Fig. 3.12,

Table 3.1: Hypothesis table, listing the combination of canonical functions M_i for each hypothesis H_j, with q degrees of freedom. When an exponential function (M_4) is tested, it replaces the linear model M_1. The Heaviside step function (M_6) is evaluated at many or all positions in the time series.

	H_0	H_1	H_2	H_3	H_4	H_5	H_6	H_7
$M_1(\nu(\mathbf{x}))$	1	1	0	1	0	0	1	0
$M_2(\eta(\mathbf{x}))$	0	1	0	0	1	0	1	1
$M_4(\kappa(\mathbf{x}),\beta(\mathbf{x}))$	0	0	1	0	1	1	0	1
$M_6(\Delta_i(\mathbf{x}))$	0	0	0	1	0	1	1	1
q		1	2	1	3	3	2	4

1. One first needs to decide whether to reject or sustain the null hypothesis by using the Overall Model Test in Eq. (3.18). Under the condition that the level of significance α_0 is defined as $1/(2m)$, the critical value K for the central χ^2 distribution is calculated. Then the decision to compete the null hypothesis can be made when $\underline{T}_0 > K$. If $\underline{T}_0 < K$, there is no need to perform subsequent MHT. In this case, the only remaining step is to reevaluate H_0 in terms of the posterior variance $\hat{\underline{\sigma}}^2$, the precision of the parameters $Q_{\hat{x}\hat{x}}$, and the eigenvalue ζ, see Eq. (4.6). If $\underline{T}_0 > K$, we start the MHT method.

2. In the case that $\underline{T}_0 > K$, one would perform the MHT method for many alternative models. The initial noncentrality λ_0 for a given $q = 1$, $\alpha_0 = 1/(2m)$ and $\gamma_0 = 50\%$ is computed and fixed. A loop runs over all H_j's, with $j \in [1, J]$. New α_j's are used to replace α_0. Then the test ratios $\underline{\mathbf{T}}^j_{q_j}$ $(\forall\, j)$ are calculated based on Eq. (3.24). If $\underline{\mathbf{T}}^j_{q_j} < 1$, the conclusion is that H_j is not more likely than H_0. If $\underline{\mathbf{T}}^j_{q_j} > 1$, the corresponding alternative hypothesis H_j is considered to be a better model candidate and stored for further use.

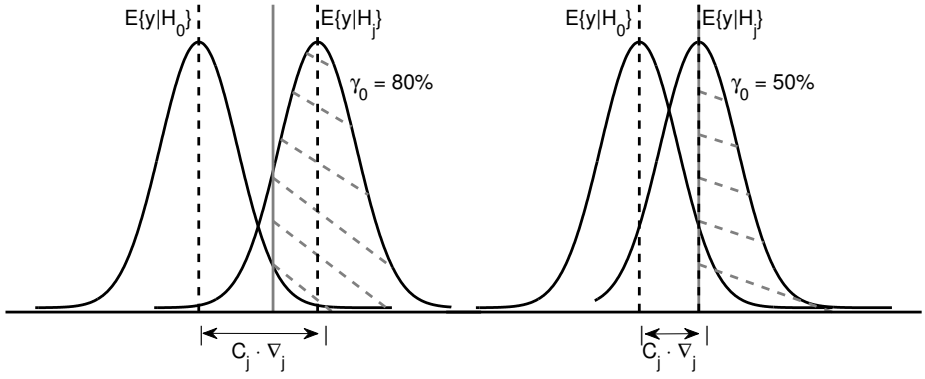

Figure 3.11: The discriminatory power γ_0 for an alternative hypothesis H_j against null hypothesis H_0. The estimation difference between H_0 and H_j is equal to $\nabla_y = C \cdot \nabla$. If the value of ∇_y is smaller, this means that an additional parameter ∇ will be detected with a smaller probability γ_0.

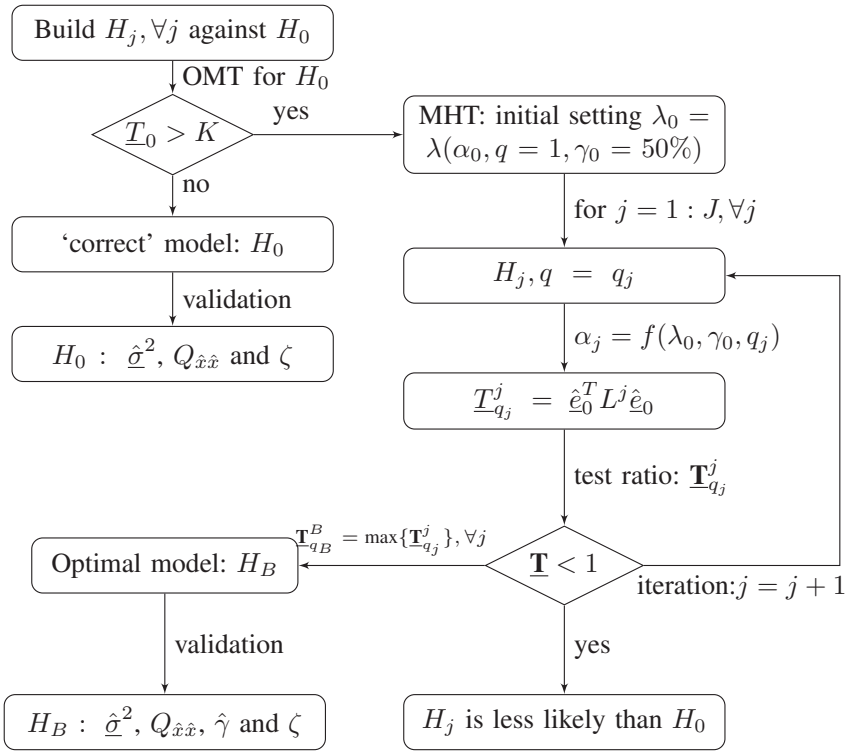

Figure 3.12: Testing flowchart for deformation modeling

3. There may be several model candidates with test ratio values larger than 1, we then select $\underline{\mathbf{T}}^B_{q_B} = \max_j\{\underline{\mathbf{T}}^j_{q_j}\}$ to be the most probable model for that time series, but store a number of alternatives for further evaluation. The parameters for the most probable model combination H_B are then estimated, as well as the posterior variance $\underline{\hat{\sigma}}^2$, the precision of the parameters $Q_{\hat{x}\hat{x}}$, the updated temporal coherence estimator $\hat{\gamma}$, and the eigenvalue ζ.

3.8. Numerical implementation

To efficiently apply the methodology to a large number of points, we discuss its numerical implementation in this section.

3.8.1. Covariance matrix Q_{yy} and design matrix A under H_0

The observation vector in our InSAR time series consists of pre-processed deformation estimates, per point and per epoch (image acquisition), relative to a reference point and a reference epoch (Hanssen, 2004). The pluriformity of scatterers, in space and time, makes it impossible to obtain an independent quality metric. Assuming tempo-

ral ergodicity, preselecting only values that behave 'smooth' in time, we use a fixed variance and assume uncorrelated observations in the time series. Hence, the $m \times m$ covariance matrix Q_{yy} is initialized by the multiplication of a specified variance factor σ^2 and an identity matrix I_m. This way, the posterior covariance matrix can be estimated by variance component estimation (Teunissen, 1988; Kenselaar, 1997; Amiri-Simkooei et al., 2007; Teunissen and Amiri-Simkooei, 2008). When the stochastic structure of the observations is better known beforehand, the covariance matrix can be more precisely specified. The design matrix A under H_0, as in Tab. 3.1, is a column of temporal baselines with respect to the master acquisition.

3.8.2. Preprocessing: reference point noise estimation

In InSAR processing, the kinematic time series of all points are all relative to a common reference point, which implicitly has a postulated zero-displacement time series. However, in reality the reference point is a scatterer as well, with SAR system thermal, quantization, and scattering noise (Zebker et al., 1994b) per epoch. Via the differencing operation that is implicit in the InSAR processing, the reference point noise (RPN)

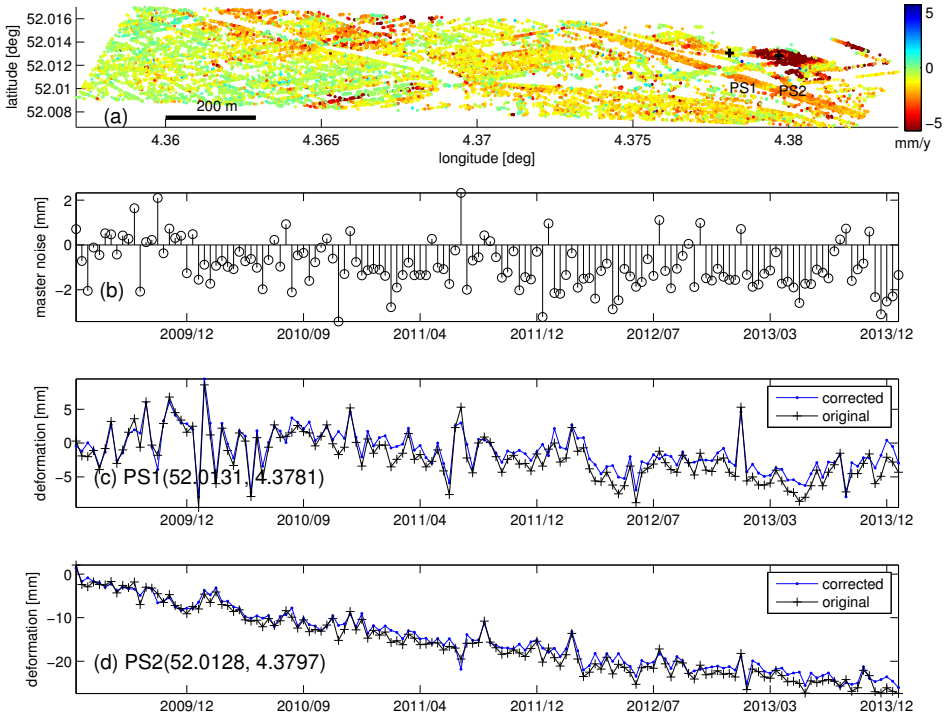

Figure 3.13: PS velocity map before removing the reference point noise (a). The error of the reference point per epoch (b). The kinematic time series of two PS points (PS1 and PS2) before (in black) and after (in blue) removing the reference point noise, shown in subfigures (c) and (d). The location of these two PS points are indicated by the black crosses in subfigure (a).

will manifest itself in every point. In other words, per epoch, the kinematic time series for all points are contaminated by the noise from the reference point. This error can be mitigated.

To estimate and mitigate the error of the reference point, we first reduce the deformation time series of every single point by subtracting a linear trend, an operation known as temporal deramping. Then, we compute the average value of all points per epoch which is considered to reflect the error of the reference point at that epoch. At the kth epoch, the error of the reference point $e^k(\mathbf{x}_{\text{rp}})$ is estimated by

$$\hat{\underline{e}}^k(\mathbf{x}_{\text{rp}}) = \frac{1}{N}\sum_{i=1}^{N} \underline{e}_i^k, \ \forall k, \tag{3.52}$$

where N denotes the number of points and e_i^k represents the residual for the ith point after temporal deramping, at the kth epoch. This error is subsequently subtracted from the kinematic time series for all points, i.e.,

$$\underline{y}'_i = \underline{y}_i - \hat{\underline{e}}(\mathbf{x}_{\text{rp}}), \ \forall i, \tag{3.53}$$

which yields an RPN-reduced time series y', to be used in the subsequent hypothesis testing approach. Informally, we refer to this RPN-reduction method as the Shenzhen-algorithm due to the location where this idea sprouted.

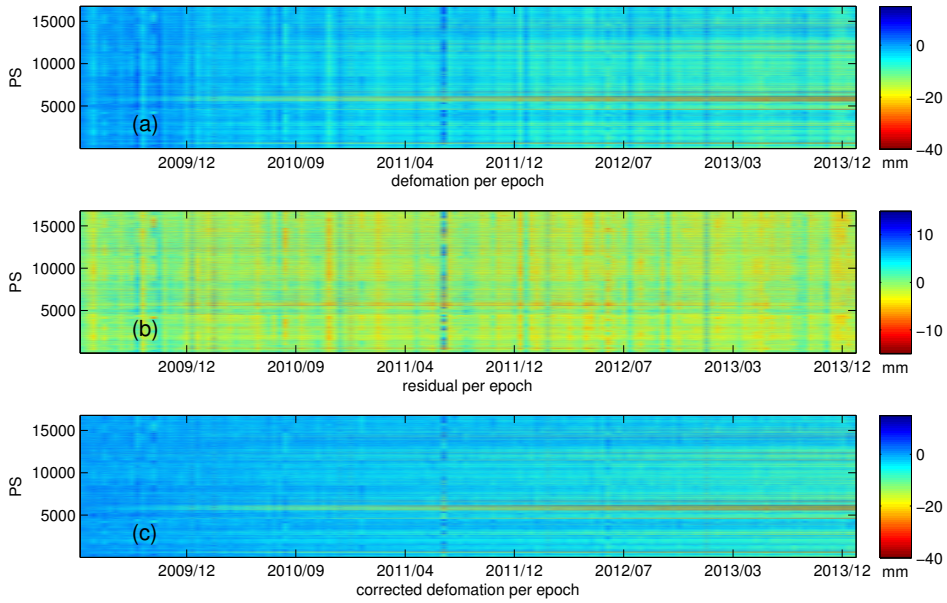

Figure 3.14: Deformation time series of PS points before (a) and after (c) removing the reference point noise. The residuals of the PS points are shown in subfigure (b). The x-axis represents the data acquisition dates, and the y-axis represents the PS serial number.

Fig. 3.13a shows the PS velocity map before removing the reference point noise. There are 16793 PS points in the map which were derived from 143 TerraSAR-X acquisitions between 08 April 2009 and 30 December 2013. The deformation time series (before removing the reference point noise) of these PS are shown in Fig. 3.14a. After performing the temporal deramping, the residuals of all PS points per epoch can be generated, see Fig. 3.14b, and used for computing the error of the reference point per epoch in terms of Eq. (3.52). The error of the reference point per epoch is then obtained and shown in Fig. 3.14c. The corrected kinematic time series of all PS points is computed by Eq. (3.53), shown in Fig. 3.14c. As an example, the kinematic time series of two PS points (PS1 and PS2) before (in black) and after (in blue) removing the reference point noise, are shown in Figs. 3.13c and 3.13d. It indicates that the corrected time series are less affected by the reference noise, showing smoother temporal behavior.

3.8.3. Preprocessing: detecting unwrapping errors

Following time series InSAR processing, there are still points which exhibit remaining unwrapping errors, either as an individual 2π-outlier, or as a 'cycle-slip', where two parts of the time series show a 2π-offset. To detect such residual phase unwrapping errors, the likelihood of remaining 2π-ambiguities in the kinematic time series is tested using the same MHT procedure, see Eq. (3.13), by fixing the outlier $D_i(\mathbf{x})$ and offset $\Delta_i(\mathbf{x})$ to be $\pm\lambda/2$, where λ represents the SAR wavelength. When hypothesis testing yields a $|D_i(\mathbf{x})|$ or $|\Delta_i(\mathbf{x})|$ larger than $|\lambda/4|$, the observation vector for that point will be corrected by $\pm\lambda/2$ to clean it from unwrapping errors, before subsequent hypothesis testing for other model errors.

3.8.4. Efficient test statistic computation

A testing procedure with hundreds of alternative hypotheses, for millions of ground targets, would be numerically very inefficient. As stated in section 3.2, the computational burden is significantly reduced by expressing the test statistic for alternative hypothesis j as

$$\underset{1\times 1}{T_q^j} = \underset{1\times m}{\hat{e}_0^T}\,\underset{m\times m}{L^j}\,\underset{m\times 1}{\hat{e}_0} = \mathrm{tr}\left(\underset{m\times m}{L^j}\,\underset{m\times 1}{\hat{e}_0}\,\underset{1\times m}{\hat{e}_0^T}\right), \tag{3.54}$$

where we have introduced the L^j matrix. The L^j matrix needs to be computed only once for every hypothesis class, but it is equal for each point, so it can be retrieved in internal memory. The $m\times m$ matrix $\hat{e}_0\hat{e}_0^T$ is computed only once per point, in evaluating only the null hypothesis.

For instance, when only the thermal expansion is considered as an additional component in the functional model, cf. M_2 in Eq. (3.13), the corresponding L matrix is temperature dependent. Fig. 3.15a shows the temperature differences between the acquisition dates of the TerraSAR-X master image (08-April-2009) and the slave images, using 127 satellite images. The corresponding 126×126 matrix L is shown in Fig. 3.15b. The seasonal variation of the temperature changes is clearly shown in Fig. 3.15b as the color changes from red to blue. This L matrix will be further used in the real case study for the Rotterdam test site, see section 3.9.2.

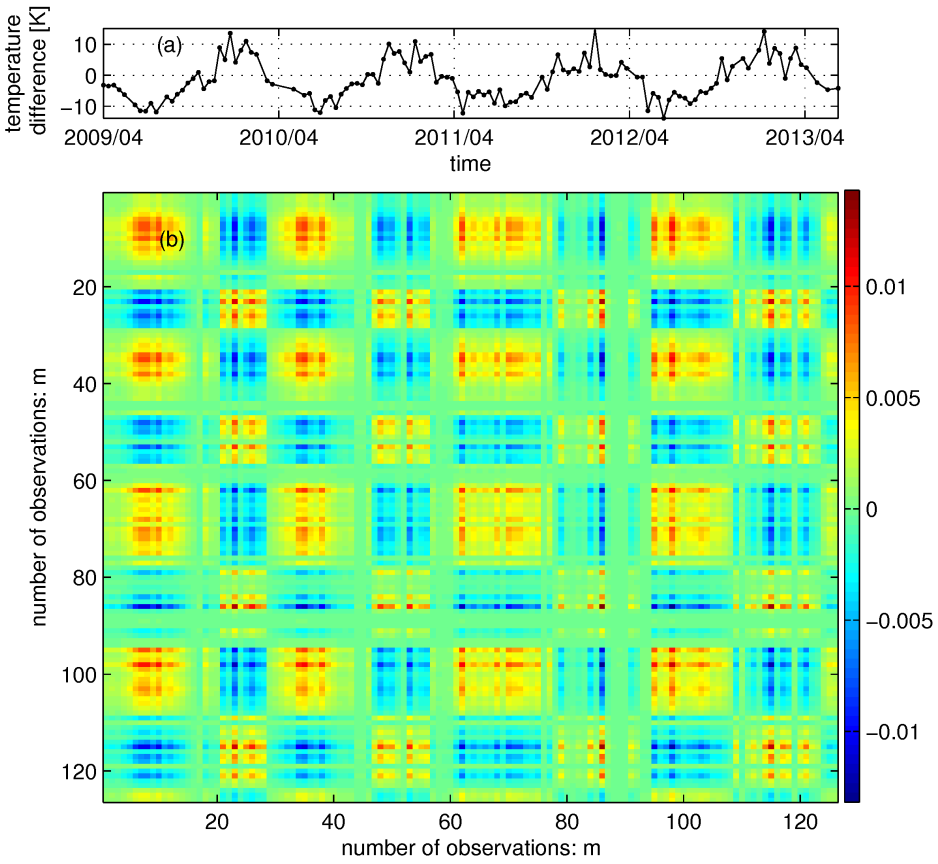

Figure 3.15: (a) Temperature differences between the acquisition dates of the TerraSAR-X master image and corresponding slave images and (b) L matrix for thermal expansion with arbitrary units, cf. Eq. (3.17).

3.9. Application on simulated data and real data

In this section we will test and evaluate the proposed MHT method, first on a simulated data set, and then on a real data set related to infrastructure (rail) monitoring.

Table 3.2: Kinematic time series modeling results for the simulated point, see Fig. 3.16.

Model Nr.	$\hat{v}$ [mm·y^{-1}]	$\hat{\eta}$ [10^{-3} m·K^{-1}]	$\hat{\kappa}$	$\hat{\beta}$	$\hat{\Delta}$ [mm]	@ acq.date	var.factor	$\hat{\underline{\sigma}}$ [mm]
H_0	−14.3						23.1	24.0
H_1	−13.6	+2.3					3.7	9.6
H_2			+20.1	−1.8			23.8	24.4
H_3	−8.4				−30.7	(18-Jun-2006)	4.4	10.5
H_4		+2.3	+130.5	−20.2			3.8	9.7
H_5			+840.5	−60.7	−30.0	(18-Jun-2006)	0.6	2.3
H_6	−10.5	+1.4			−17.1	(18-Jun-2006)	0.8	4.5
H_7		+1.4	+1100.9	−100.1	−17.1	(18-Jun-2006)	0.8	4.5

Table 3.3: Kinematic time series modeling results for eight PS points (PS1–PS8), see Fig. 3.17.

Point ID	Model Nr.	$\hat{v}$ [mm·y^{-1}]	$\hat{\eta}$ [10^{-3} m·K^{-1}]	$\hat{\kappa}$	$\hat{\beta}$	$\hat{\Delta}$ [mm]	@ acq.date	var.factor	$\underline{\hat{\sigma}}$ [mm]
PS1	H_0	−7.2						0.2	1.3
PS2	H_1	−2.6	−0.24					0.6	2.3
PS3	H_2			−78.3	+6.0			0.4	1.9
PS4	H_3	−5.4				+5.4	(28-Feb-2012)	1.1	3.1
PS5	H_4		+0.18	−21.2	+12.6			0.4	1.9
PS6	H_5			−30.0	+2.2	+7.2	(30-Jan-2010)	0.6	2.3
PS7	H_6	−3.4	−0.21			+4.8	(04-Jan-2012)	0.5	2.1
PS8	H_7		−0.19	−10.6	+3.1	−5.3	(16-Sep-2011)	0.6	2.3

3.9.1. Application on simulated data

To demonstrate the feasibility of kinematic model selection and parameter estimation using a probabilistic approach, we evaluate a synthetic example. We simulate 70 Envisat SAR images acquired between December 2003 and October 2010, for a single point, relative to an arbitrary reference point. We use the real temperature records for the actual Envisat acquisition dates. The time series of this point is modeled as a superimposition of linear motion ($v = -10$ mm/y), thermal expansion $\eta = +1.3 \cdot 10^{-3}$ m·K^{-1}, and an instantaneous Heaviside offset at or before the 26th acquisition (18 June 2006) with a level of $\Delta_{26} = -18$ mm. Gaussian distributed random noise with 5 mm standard deviation is added. Hence this fits with the sixth alternative hypothesis model H_6 shown in Tab. 3.1, see Fig. 3.16a. Following the processing procedure outlined in section 3.7, the OMT is first applied for the null hypothesis H_0 under the level of significance $\alpha_G = 23\%$, which follows via the B-method of testing from $\alpha_0 = 1/(2m)$ for the one-dimensional test, see section 3.6.2. The test statistic corresponding to each model is listed above each subfigure of Fig. 3.16, and repeated for convenience in Tab. 3.2. For H_0, the value is much larger than the critical value K (see Fig. 3.16a), causing its rejection. Then the procedure starts to find the most probable model among the alternatives. After evaluating every test statistic ratio, corresponding with the subfigures of Fig. 3.16, the most probable model, with the greatest test statistic ratio, is the alternative hypothesis H_6. For model H_6, we then estimate the corresponding parameters $\hat{v}, \hat{\eta}, \hat{\Delta}$ to be -10.5 mm/y, $+1.4 \cdot 10^{-3}$ m·K^{-1} and -17.1 mm at the 26th acquisition, which is convincingly close to the simulated values. After selecting model combination H_6 as the most probable one, the posterior variance for H_6 is estimated to be 4.5^2 mm^2.

3.9.2. Application on real data

To test the approach using real data, an experiment is performed for a test site in the Rotterdam area, the Netherlands, during the period from April 2009 to June 2013. We use a stack of 127 TerraSAR-X stripmap images and apply the Delft implementation of Persistent Scatterer Interferometry (DePSI) (van Leijen, 2014) to produce the kinematic time series of persistent scatterers (PS), using a default steady-state model to facilitate temporal unwrapping. We regard these PS results as the input data for kinematic time series modeling. We remove the reference point noise from the data using the Shenzhen algorithm, see section 3.8.2. We use the daily average temperature data for every acquired date, see Fig. 3.15a. The variance of unit weight σ^2 as in Eq. (3.15) is conser-

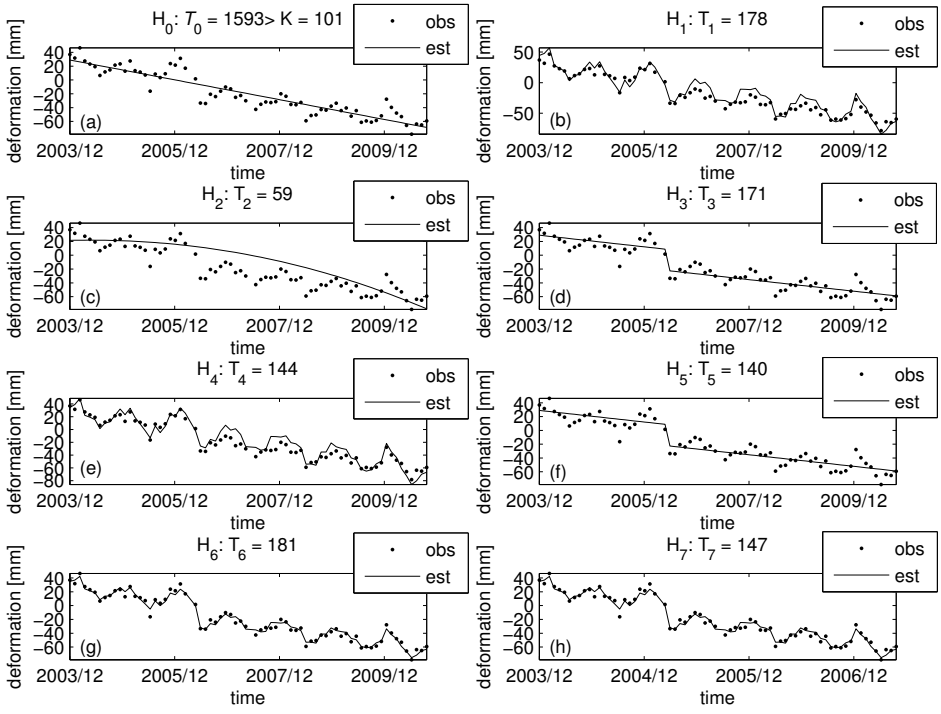

Figure 3.16: Synthetic example for multiple hypotheses testing. Black dots show the simulated kinematic data with noise modeled as the sixth alternative hypothesis model H_6. (a) null hypothesis model: steady-state (linear) motion, which is the default model for InSAR processing. Subfigures (b)–(h) show the estimated parameters for the alternative hypotheses H_1–H_7, respectively. Based on the test statistic ratios $\underline{\mathbf{T}}^k_{q_k}$, depicted in the title of each graph, the most probable model is determined, being alternative hypothesis H_6 which has the greatest test statistic ratio.

vatively predefined as 3^2 mm^2 and the cofactor matrix R_{yy} is designed as an identity matrix. According to Eqs. (3.42) and (3.48), the MDV for every additional parameter can be computed, for example the MDV of the temperature-related parameter which is 0.12 [mm$\cdot K^{-1}$] when $\lambda_0 = \lambda(\alpha_0 = 1/(2\times 127), q = 1, \gamma_0 = 50\%) = 8.23$. This implies that for a specific target, if the temperature dependent parameter is 0.12 [mm$\cdot K^{-1}$], it will be found with a likelihood of 50%. (A greater value of this parameter will be detected with a higher likelihood).

The results from the kinematic time series modeling show that 84% of the points sustains the steady-state null hypothesis H_0, while the others reject H_0 and follow the alternative models. Fig. 3.17 illustrates the MHT results for eight typical PS points, and their parameter estimates are listed in Tab. 3.3. The locations of the points are shown in Fig. 3.19. These results show that (i) each function from the library of canonical kinematic models seems physically realistic and can be used to produce an optimal kinematic model for these real data; (ii) the optimal models are different per point, as well as the quality of estimates; (iii) the optimal models for the eight PS points fit

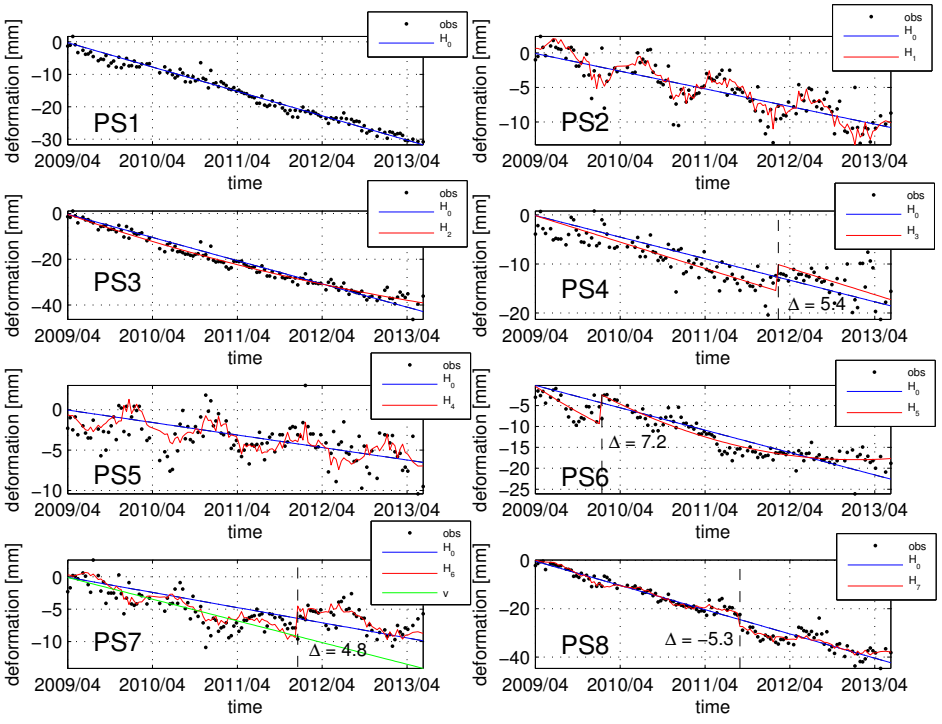

Figure 3.17: Real data examples for multiple hypotheses testing. Each subfigure shows the most probable deformation model found for a randomly selected PS point (see Figs. 3.19a and 3.19b for the location).

the kinematic time series (black dots) better than the linear deformation model (blue lines), in a probabilistic sense. All but one of the posterior variances $\underline{\hat{\sigma}}^2$ of the eight points shown in Tab. 3.3 are smaller than the conservative a priori variances, which improves the reported quality of the estimates and the time series. In addition, the kinematic time series results allow us to detect anomalous offsets Δ for PS4, PS6, PS7 and PS8.

Fig. 3.18 demonstrates that the MHT method is able to fix unnoticed unwrapping errors. It shows the MHT results for PS points 6, 9 and 10, cf. Fig. 3.19. H_5, H_3 and H_6 (black lines) are found to be the most probable models for them. For PS6, a Kronecker delta outlier is found at the 114th epoch, greater than the half wavelength, 15.5 mm, see the arrow indicator in Fig. 3.18a. Thus, the algorithm identifies it as the single unwrapping error at 23-Jan-2013 and corrects it (indicated by the green dot). For PS9 and PS10, the values of the estimated Heaviside offsets are larger than 15.5 mm as well. Therefore, they are identified as residual unwrapping errors, and corrected by adding the offsets back (shown in green).

To demonstrate the applicability of our approach on large volumes of data and analyze 4.5×13 km area near Rotterdam, the Netherlands, with 748806 PS points. Figs. 3.19a and 3.19b show the ground features of a subset (0.5×2 km) of this crop area,

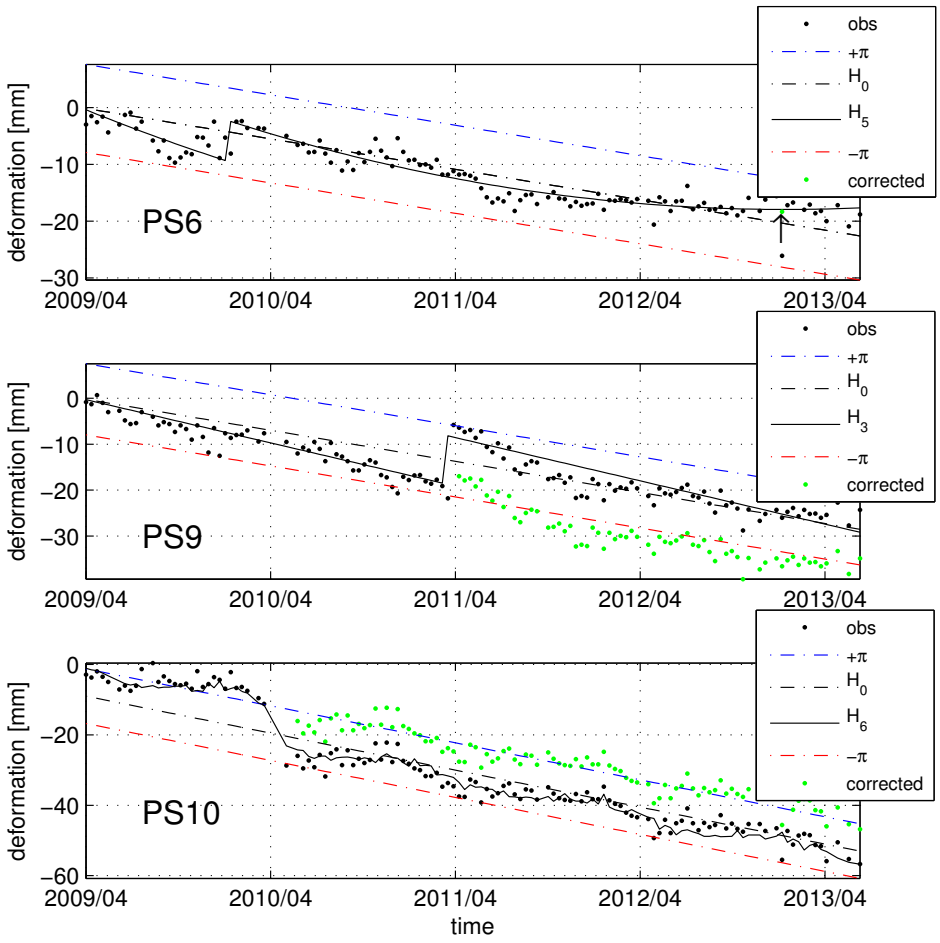

Figure 3.18: Examples for residual unwrapping error detection and correction by the MHT approach. The black up-arrow in the top plot indicates the observation on 23-Jan-2013, which is corrected for the unwrapping error from the black dot to the green dot. The lower plots indicate detected offsets (cycle-slips) in the observations.

dominantly a railway (Betuweroute, denoted by 'B') and motorway (A15) with some adjacent buildings. This subset shows 5857 detected PS, of which ten points are further elaborated in time, see Figs. 3.17 and 3.18, indicated by the red crosses.

Fig. 3.19c shows the line-of-sight velocity map of all PS points selected by default PSI processing. It indicates that the PS points reflected from the buildings (in yellow in Fig. 3.19b) are stable, while the PS points reflected from the railway lines and the motorway are deforming but with different rates. Along the railway lines, the PS velocities are heterogeneous, for instance, discrete discontinuities of the velocities are detected in the transition zones between free embankments and fixed substructures, such as the bridge (cf. C in Fig. 3.19b). Fig. 3.19d shows the line-of-sight velocity map of the

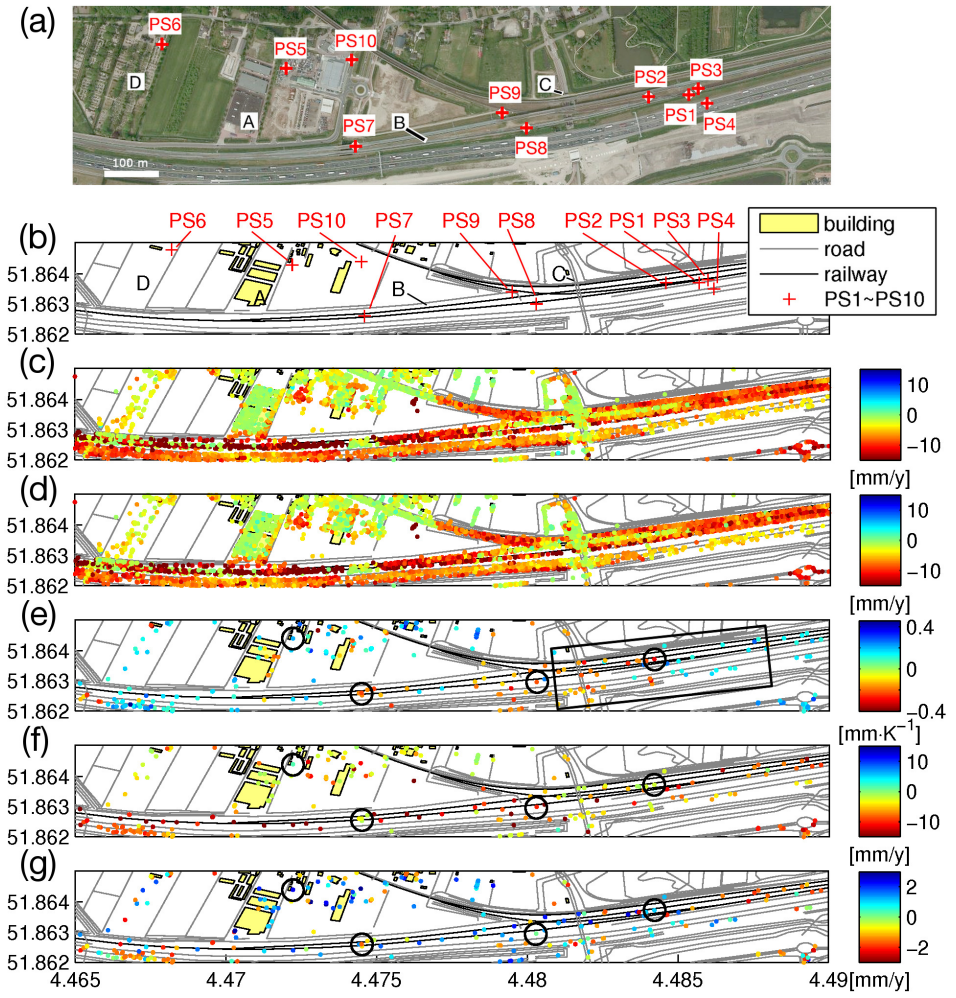

Figure 3.19: Kinematic time series analysis for the 0.5 × 2 km test area. (a) Aerial image (Bing maps). (b) Cartographic representation (Top10vector, 2011). (c) Default line-of-sight velocity map resulting from standard PSI processing. (d) Points that sustain the null hypothesis of steady-state deformation only. (e) Thermal expansion parameter η of those points whose optimal model combination includes $M_2(\eta(\mathbf{x}))$. (f) Line-of-sight velocity map corresponding to the points shown in (e). (g) Estimated velocity differences between H_0, cf. (c), and the post-determined best models for the points shown in (e).

84% PS points which sustain the null hypothesis H_0. That is, the motion of most PS on buildings, bridges and railway is best described by the default steady-state model. Yet, Fig. 3.19e shows the thermal expansion parameter η of those PS whose optimal model includes $M_2(\eta(\mathbf{x}))$, cf. Eq. (3.13). It suggests that the motions of ground targets made of concrete or steel, such as buildings, railway lines and lamp poles, are subject

to temperature variations in the form of expansion when temperature rises and contraction when temperature falls. Consequently, the thermal expansion parameter for these targets is negative ($\eta < 0$), shown in orange/red in the figure. For instance, building A, bridge C, and the railway parts and segments made of concrete/steel, (e.g. PS2, PS7 and PS8) all have a negative thermal expansion parameter. The data also show motion of targets with a positive thermal expansion parameter (in blue). These behave conversely, such as the motion of some segments of the railway tracks and a graveyard area denoted by D and PS5. These are most likely influenced by compaction due to seasonal changes in the groundwater table. Thus, according to the value (and sign) of the thermal expansion parameter, we can classify the PS points in terms of different materials and characteristics. Areas where a sign change occurs, cf. the rectangular black box in Fig. 3.19e, may indicate signal locations and materials susceptibility to fatigue. Fig. 3.19f shows the line-of-sight velocity map derived from the post-determined best models for the PS points shown in Fig. 3.19e. It shows that buildings and bridges (e.g. building A and bridge C) experience minimal motion apart from those that are temperature related, while the railway tracks show heterogeneous motion at different rail segments, probably due to different local situations such as consolidated/unconsolidated soils. Fig. 3.19g shows the estimated velocity differences between H_0 and the post-determined best models for the PS points shown in Fig. 3.19e. It implies that if we harshly stick to the null hypothesis H_0 for every single point, we may overestimate or underestimate the linear deformation, leading to an erroneous interpretation of the time series. For example, the deformation rate of PS7 under H_6 (including thermal variability) is $v_{H_6} = -3.4$ mm/y (green line in Fig. 3.17) which is significantly larger than the rate under H_0, $v_{H_0} = -2.4$ mm/y, see also Tab. 3.3. The fact that the likelihood of H_6 is greater than that of H_0 now improves the reliability of the estimates.

In terms of computational efficiency, since our method does not require the explicit estimation and adjustment of all the parameters for each evaluated model, the computational load is reduced with a factor of five. The computation time for the test is 31 ms per point, testing about 508 alternative hypotheses on an average desktop computer.

3.10. Discussion and conclusions

A probabilistic approach using multiple hypotheses testing (MHT) and the B-method of testing is proposed for kinematic time series modeling and parameter estimation. It is generally applicable to select the optimal (most probable) models for single points in InSAR kinematic time series, and to detect and correct phase unwrapping errors in a probabilistic sense.

This way, apart from *precision* now also the geodetic concept of *reliability* is added to InSAR estimates, defined as the ability to detect observational errors or model imperfections from the data. These model imperfections can relate to both the functional as well as the stochastic model, with the latter giving an improved quality description of the results.

Even though there may be several competing models with a high likelihood of being true, the methodology will allow users to critically evaluate results, avoid overinterpretation, and thereby consolidate InSAR as a geodetic technique.

The methodology described in this chapter is applied as 'post-processing' on the

PSI results. Yet, using an efficient numerical implementation it is recommended to include it at an earlier stage, i.e., the parameter estimation per arc in the PSI processing.

4
Railway Monitoring

This chapter demonstrates the feasibility of monitoring railway infrastructure using multi-epoch satellite radar observations. We discuss two distinct case studies. The first study site is situated in the Himalaya region and demonstrates the potential for monitoring remote and rather inaccessible areas, given the availability of a limited amount of satellite data. We apply an 'all-pixel' approach based on the statistical similarity of pixels to maximize the point density, and show linear settlement behavior as well as seasonal effects that suggest a dynamic influence of thawing permafrost in the region. The second study site is a rail track area situated in the Netherlands. This case study aims at the detailed analysis and interpretation of high resolution SAR data acquired from different viewing geometries, in order to estimate the deformation vector components in a rail-fixed reference system. Both studies are published in the *International Journal of Remote Sensing* (Chang and Hanssen, 2015), and the *International Journal of Railway Technology* (Chang et al., 2014), respectively.

4.1. Qinghai-Tibet railway

Climate change and human involvement are changing the dynamics of permafrost environments, with potential impact on the safety and stability of infrastructure. The Qinghai-Tibet Railway (QTR) has been designed to withstand the dynamic permafrost conditions. Yet, in-situ measurements of the track stability at elevations of about 5 km are scarce. In this case study, we attempt to detect indications of permafrost-related instabilities over an 80 km segment at the highest part of the QTR, by using medium-resolution Envisat SAR images. Section 4.1.1 gives a brief introduction to the Qinghai-Tibet railway. Section 4.1.2 introduces the geological situation and the Envisat SAR data used in the area of interest. Our approach for deformation time series estimation and analysis is elaborated in section 4.1.3. We discuss the results and interpret the most probable driving mechanisms for the deformation in section 4.1.4, followed by conclusions in section 4.1.5.

4.1.1. Introduction

The Qinghai-Tibetan Plateau is well known as 'the roof of the world', see Fig. 4.1a. Around fifty percent of the plateau is underlain by permafrost. Due to climate change and human involvement, permafrost degradation and increasing ground temperatures have been observed in recent decades (Wu and Liu, 2004; Cheng and Wu, 2007; Wang et al., 2000). Such environmental changes may cause instability or damage to infrastructure (Yu et al., 2002; Wu et al., 2002; Jin et al., 2008). The Qinghai-Tibet Railway

(QTR) is crossing the plateau, connecting Lhasa and Golmud by 1956 km of railway track, including 550 km over permafrost, see Fig. 4.1b. To ensure a safe and sustainable operation of the QTR, regular measurement campaigns are performed since regular train connections started in 2006. Geodetic measurements include GPS surveys and spirit leveling (Welk, 1997). However, such in situ surveys are notoriously difficult for the QTR, due to the harsh environmental conditions at an elevation of 5 km and higher. To investigate whether permafrost dynamics influence the infrastructure, Interferometric Synthetic Aperture Radar (InSAR) techniques (Massonnet et al., 1993; Hanssen, 2001) may be used as an alternative. InSAR uses two or more satellite radar measurements of the same area to extract ground deformation remotely and periodically, with millimeter accuracy. InSAR techniques have been widely applied in monitoring 'natural' geophysical processes but lately they have also been successfully deployed for structural health monitoring of infrastructure, especially in urban areas (Franceschetti et al., 2002; Arikan and Hanssen, 2008; Chen et al., 2012; Chang and Hanssen, 2014).

Interferometric processing techniques require temporally coherent observations. However, in a dynamic environment (snow, ice), coherence over longer time intervals is rare, which implies that only few pixels can be used. Conventional techniques attempt to identify coherent pixels before the deformation parameters are estimated (Bamler and Hanssen, 1997; Ferretti et al., 1999b; Ciuc et al., 2002). Here we apply an alternative processing methodology, in which we first estimate the displacement time series for all pixels on the track irrespective of coherence. This is followed by an a-posteriori assessment of their quality based on a specific set of criteria, as described below. In this approach, we need to reduce the phase noise due to geometric decorrelation, obtain sufficient observations along the track, detect relevant anomalies along the track, and preferably find the most probable driving mechanisms. To satisfy these conditions, we use a maximum perpendicular baseline threshold to select the interferograms to reduce geometrical decorrelation (Berardino et al., 2002; Mora et al., 2002; Lanari, 2003) and guarantee sufficient coherence while not losing resolution due to range filtering (Gatelli et al., 1994). We then estimate the deformation time series for all scatterers on the track, that is, irrespective of whether they are persistent scatterers (PS), distributed scatterers (DS), or noise. We introduce a seasonal component into the deformation model and estimate the unknown parameters based on the least-squares estimation. Finally, we assess whether the estimated deformation parameters of the QTR can be attributed to permafrost dynamics.

4.1.2. Geological situation and radar data

Permafrost is classified into cold, transitory, and warm classes (van Everdingen, 1998). The cold (less than $-1.5°C$) and transitory permafrost are relatively inactive as the ground warms up, while the warm (more than $-1°C$) permafrost is relatively active and most vulnerable against thawing. In the permafrost environment, the active layer thaws during summer and freezes in autumn (Brown and Kupsch, 1974). It extends from the ground surface to the top of the permafrost layer. The permafrost layer includes frozen sediments, ground ice, bedrock and organic materials (Linell et al., 1981). Distributed along the QTR, there is 416 km of warm permafrost (Cheng, 2003). According to observations during 2006 and 2010 at 27 sites, the active layer at the Tanggula

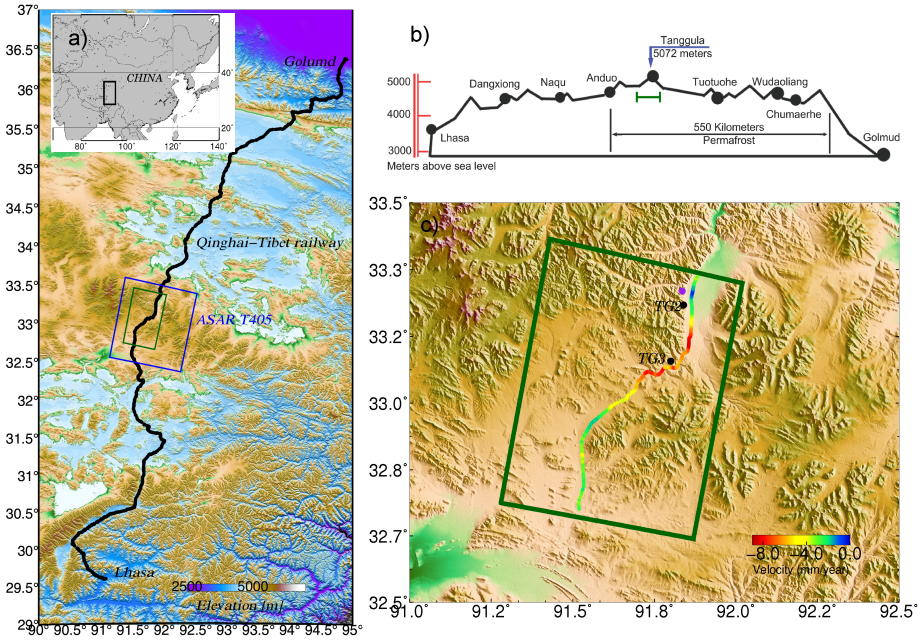

Figure 4.1: (a) Location of the Qinghai-Tibet Railway (QTR) on the Qinghai-Tibetan Plateau. The QTR is indicated by the black line on the elevation map. The full Envisat SAR image is marked by the blue square, while we evaluated the area marked in green. (b) Elevation profile of the QTR track over a length of 1956 km, including 550 km over permafrost. (c) Estimated linear deformation velocities in vertical direction.

Mts. site is one of the thickest, with depths down to 4 m (Wu et al., 2012). Therefore, we chose this area as our study site, indicated by the green rectangle in Figs. 4.1a and 4.1c. This area is located in the Qiangtang terrane (An et al., 2001; Royden et al., 2008), with flat terrain in the southwest and the highlands in the southeast and north. Borehole drillings show a geological structure consisting mainly of prairie soil, followed by a frozen sandy gravel stratum (two meters below), and ice with clay. The frozen sandy gravel stratum includes various unconsolidated sediments such as gravel, sand, silt and clay.

We used a stack of 15 Envisat SAR images (Envisat, ASAR, 2004) acquired between February 2007 and June 2009 (Track/Orbit: t405/T26010, see Tab. 4.1), to investigate the QTR ground deformations during its operational use. The radar aboard the Envisat satellite operates in C-band (5.6 cm), VV polarization mode. All used scenes are acquired from the descending orbit.

4.1.3. Methodology

In order to obtain a stack of high coherence interferograms without limiting ourselves to point-like scatterers, we define a threshold of 800 m for the perpendicular baseline to select the interferograms. This leads to 15 radar images to generate the interferograms. Every interferogram is the complex multiplication between two radar images: a

Table 4.1: Envisat SAR datasets used in this study (Track/Orbit: t405/T26010). The temporal baselines B_t and perpendicular baselines $B_\perp$ are relative to the master image.

Nr.	Acquisition dates	B_t[days]	$B_\perp$[m]
1	20070220	-385	240.1
2	20070501	-315	66.1
3	20070605	-280	160.4
4	20070710	-245	-9.2
5	20070814	-210	30.5
6	20071127	-105	240.9
7	20080101	-70	-218.0
8	20080311 (master)	0	0.0
9	20080520	70	111.9
10	20081216	280	-43.2
11	20090120	315	237.4
12	20090224	350	227.9
13	20090331	375	706.5
14	20090505	420	58.0
15	20090609	455	392.2

'master' and a 'slave' image. To align all interferograms to the same master (radar) coordinate system, a master image acquired on 11 March 2008 is selected and all the other images are aligned on the master grid. Tab. 4.1 lists the acquisition dates and the temporal and perpendicular baselines w.r.t. the master image for the Envisat SAR data. We spatially crop all the images to an area of 80×50 km (marked by the green rectangle in Fig. 4.1). We oversample all SAR images by a factor of two to avoid aliasing during interferogram formation, thereby reducing the pixel size of the SAR images in ground-range from 20 to 10 m. We remove the main part of the topographic contribution via a 90 m resolution DEM (SRTM, (Farr et al., 1999)) after the interferogram generation since the terrain variability is considerable. Regarding the atmospheric inhomogeneities between master and slave images, we apply a temporal filter to remove the atmospheric influences, in this case a temporal low pass filter since atmospheric states are assumed to be uncorrelated in time. Then we produce the atmospheric phase screen (APS) by an Ordinary Kriging method, see e.g. Wackernagel (1995), for each interferogram and remove the noise. The Ordinary Kriging method is able to smoothly interpolate the atmospheric phase for all scatterers and decrease the noise by variogram estimation. Yet, water vapor variability is minimal at these high altitudes.

We apply a two-step processing procedure to obtain the deformation time series along the QTR track. First, for the wider area, within the selected image crop, we apply standard PSI processing, see Ferretti et al. (2000a); Kampes (2005), to select temporally coherent, point-like scatterers and estimate the atmospheric phase screen. The result of this step is a sparse set of PS points, but sufficient to estimate several nuisance parameters. Second, for a two-sided 500 m wide buffer area along the geodetic coordinates of the QTR, we apply the estimation algorithm on *all* pixels, irrespective of phase stability. This approach allows us to (i) identify a maximum amount of measurement

points, (including metal, concrete and stone of the railway construction), as well as relevant points next to the tracks, while (ii) using the wide-scale PSI approach to reduce the computational efforts.

Point selection

When all pixels within the buffer area are evaluated, the QTR track will contain many incoherent pixels. We identify the coherent pixels using a series of adaptive directional windows centered at a given pixel, minimizing the local gradient of amplitude, to calculate the coherence value per pixel. The coherence value $\hat{\gamma}$ is estimated by (Touzi et al., 1999; Hanssen, 2001)

$$|\hat{\gamma}| = \left| \frac{\frac{1}{N}\sum_{i=1}^{N} M_i S_i^*}{\sqrt{\frac{1}{N}\sum_{i=1}^{N} M_i M_i^* \frac{1}{N}\sum_{i=1}^{N} S_i S_i^*}} \right|, \tag{4.1}$$

where M_i and S_i are the complex values at a given pixel in two coregistered SAR images, the superscript $\{^*\}$ is the sign for the complex conjugate, and N is the number of pixels in the adaptive window. We find statistically homogeneous pixels (SHP) within the adaptive window as suggested by Ferretti et al. (2011). Whether two selected pixels can be considered as SHP is computed by hypothesis testing based on the amplitude statistics of pixel pairs. In this testing, a neighboring area per pixel is established by a comparison of the similarity of the empirical distribution functions of the two temporal samples. Compared with the traditional boxcar window method, the adaptive window method preserves edge structures and avoids pixel heterogeneity (Ferretti et al., 2011). We use the Kolmogorov-Smirnov (KS) test for hypothesis testing. This is a nonparametric test which allows us to determine whether two or more pixels differ significantly. An intermediate product in the KS test is the brotherhood number image. The brotherhood number for every pixel is an indicator for the spatial similarity between this pixel and its surroundings. For instance, a pixel without 'brothers' is either a single coherent point (PS), or it is decorrelated, as it has no similarity with its surroundings. When the brotherhood number for a certain point is 40, it means this point has 40 similar neighboring pixels.

Parameter estimation

Due to freezing and thawing of the active layer, we expect seasonal displacements, and thus the linear deformation model needs to be extended to account for these periodic changes. In first order approximation, we add a sinusoidal function (cf. Eq. (3.4) and appendix B) to the deformation model, defined at a given position $\mathbf{x} = \mathbf{x}(x, y)$, and expressed as (Kampes, 2005; van Leijen and Hanssen, 2008)

$$\underline{y}(\mathbf{x}) = t \cdot v(\mathbf{x}) + \sin(2\pi t) \cdot s(\mathbf{x}) + (\cos(2\pi t) - 1) \cdot c(\mathbf{x}) + \underline{e}, \tag{4.2}$$

where $\underline{y}(\mathbf{x})$ is the unwrapped phase observation in the line-of-sight (LOS) direction, and t is the temporal baseline (in years). The underlining of a vector indicates a stochastic entity. The parameter $v(\mathbf{x})$ represents the linear deformation rate in LOS, while the coefficients $s(\mathbf{x})$ and $c(\mathbf{x})$ represent the seasonal periodic deformation in LOS,

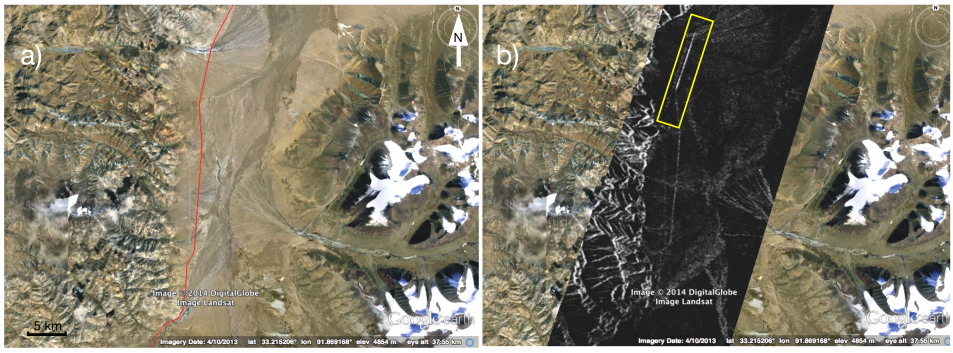

Figure 4.2: Selected part of the QTR track in optical and radar imagery. (a) location of the part of the QTR (in red) in an optical (Landsat) image. (b) incoherently averaged radar amplitude image, showing a clearly detectable QTR.

with amplitude $A(\mathbf{x}) = \sqrt{s^2(\mathbf{x}) + c^2(\mathbf{x})}$, and time offset (w.r.t. the master image time) $t_0(\mathbf{x}) = -\text{sgn}(c(\mathbf{x})) \cdot \arccos(s(\mathbf{x})/A(\mathbf{x}))/2\pi$. The period of the sinusoidal function is assumed to be one year. Unmodeled noise is denoted as $\underline{e}$, which is the residual between the observations and the estimations of the functional model using the best estimates of the parameters. The linear and seasonal contributions of the deformations are estimated by means of the least-squares estimation. Note that due to the limited number of available Envisat SAR acquisitions after the QTR started its regular service, the data span only 28 months. This implies that the seasonal component can be detected from our data processing while the monitoring of longer term periodical deformations would require more radar data.

The deformation in the line-of-sight direction can be projected onto the vertical direction under the assumption that the deformation is predominantly in the vertical deformation and the horizontal deformation is marginal. Then, the vertical deformation $y_v(\mathbf{x})$ follows from $y_v(\mathbf{x}) = \underline{y}(\mathbf{x})/\cos\theta_{\text{inc}}$, where θ_{inc} represents the satellite incidence angle.

4.1.4. Results and discussion

Fig. 4.2 shows the selected part (that is the rail segment between TG2 and TG3, see Fig. 4.1) of the QTR in optical (Landsat) and radar imagery. In Fig. 4.2b the incoherent amplitude average of 15 Envisat SAR images is draped over the optical image. The QTR is a strong signal in the radar image because the scattering conditions of the railway construction are uniform, while the amplitude is largely dependent on the orientation of the track. A cardinal effect is visible for the parts of the track parallel to the azimuth direction of the SAR. The Envisat satellite flew southbound (descending track) with its radar antenna pointing westward. Since high mountains are located directly to the west of the QTR, while the east side is less undulated, the QTR is well visible in the SAR images. Yet, to monitor the entire QTR, layover and shadowing, e.g. in the steep canyons, need to be taken into account while planning the optimal SAR acquisition geometry (Hanssen, 2001).

Figs. 4.3a and 4.3b show the incoherently averaged amplitude image and the brotherhood number image, respectively, over a 7.2×1.2 km area indicated by the yellow rectangle in Fig. 4.2b. The brotherhood number is used to separate the QTR track and its embankment from the surrounding area. We construct the adaptive window for coherence computation per pixel based on the threshold setting for the brotherhood number per pixel. Two linear objects, the G109 high speed way (located to the west of the QTR) and the QTR track, are visible because of their high average amplitude values shown in Fig. 4.3a.

We infer that the pixels with less than 60 brothers are typically reflected from the QTR track itself including the embankment. Along the track, we recognize 1 to 4 grid elements per azimuth line who have less than 60 'brothers' (see Fig. 4.3b). Pixels with more than 60 brothers are considered to be representing the surrounding meadow area, and are discarded from further analysis.

All observed deformations are relative to a specific reference point. If this point is unstable, then deformation interpretations for all the other points will be affected. To find an optimal reference point, we select an area with minimal variability in spatial deformation, in this case a 500×500 m bare rock area (indicated by the purple circle in Fig. 4.1c), 2.4 km away from the QTR. All the deformations along the track are now relative to this local reference area. The cumulative vertical displacements, $y_v(\mathbf{x})$, along the track are shown in Fig. 4.4a, showing significant lateral variability.

Figs. 4.4b and 4.4c show the estimated linear component $t \cdot \underline{\hat{v}}(\mathbf{x})$ and the seasonal components $\sin(2\pi t) \cdot \underline{\hat{s}}(\mathbf{x}) + (\cos(2\pi t) - 1) \cdot \underline{\hat{c}}(\mathbf{x})$ from Eq. (4.2). The comparison with the elevation profile, Fig. 4.4e, suggests that the subsidence is faster along flatter areas of the terrain, possibly due to the accumulation of sedimentary layers, sensitive to permafrost variation. Between 20 and 75 km along the track the elevation difference is less than 10 m. It is evident that there is a significant seasonal signal, with downward motion (red colors) in summertime and relative upward motion (blue) during winter. This corresponds with the expected dynamics of the active layer. The seasonal motion covers a range of up to 20 mm. Fig. 4.4d is the residual $\underline{\hat{e}}$ from Eq. (4.2), which is in the order

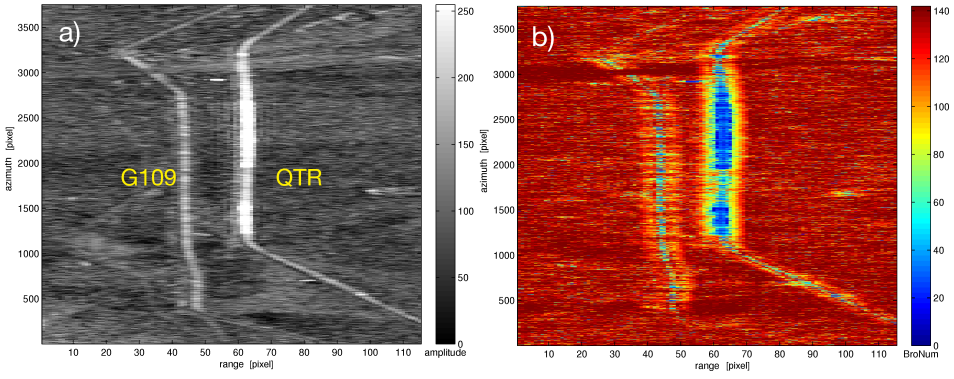

Figure 4.3: (a) Incoherently averaged amplitude image. (b) Brotherhood number image in radar coordinates (range and azimuth direction). This 7.2×1.2 km area is indicated by the yellow rectangle in Fig. 4.2.

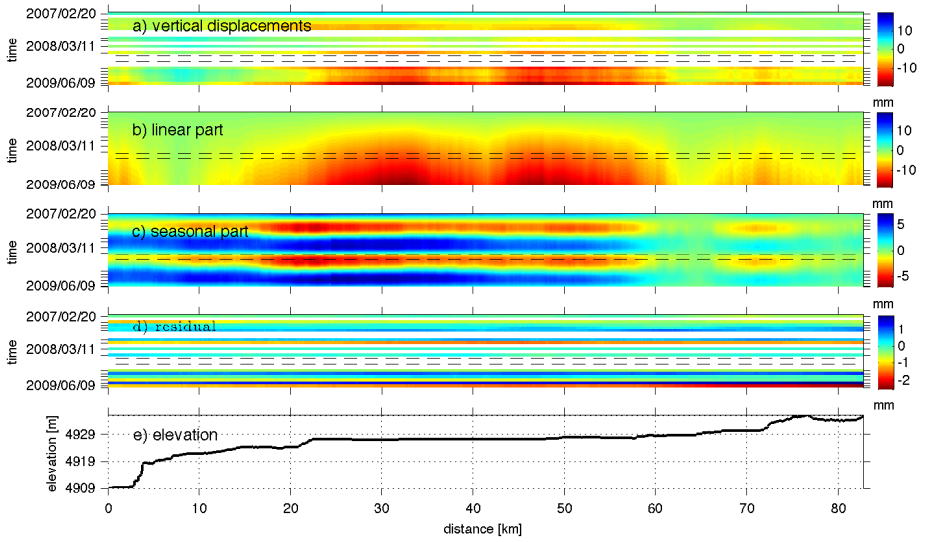

Figure 4.4: (a) Cumulative temporal evolution of observed vertical displacements along the track during the evaluated time period. Tick marks along the vertical axis indicate the SAR acquisition dates. The dashed horizontal lines refer to a period of seismicity between 08-June and 10-August 2008. (b) Estimated linear displacement per location. (c) Estimated seasonal part. (d) Residual signal. (e) Elevation profile corresponding with the track area. The x-axis is the 3D lateral distance (northbound) along the railway.

of a few mm. Both the total as well as the seasonal signal seems to be correlated with the vertical gradients of the track: higher gradients decrease the velocity as well as the seasonal amplitude of the signal. The horizontal dashed lines refer to the period of seismicity between 08-June and 10-August 2008 (USGS, `http://earthquake.usgs.gov`). From this we conclude that potential displacements due to seismic activity along the track cannot be detected from these data.

Empirical data on the dynamics of the active layer were collected by Wu et al. (2012). Between 2006 and 2010, the active layer thickness of two Tanggula Mts. sites named TG2 (91.88°E, 33.31°N) and TG3 (91.80°E, 33.09°N), see Fig. 4.1c, was found to be 4.99 m and 4.59 m, respectively. Moreover, the corresponding rates of thickness-change were 19.9 cm/y and 15.4 cm/y, indicating a deepening (thawing) active layer, and a significant inter-annual variation was observed during 2006 and 2010. We find the seasonal periodic deformation observed over the QTR to be one order of magnitude smaller than the thickness change of the active layer reported by Wu et al (2012). This could be the result of the dampening of the deformation signal due to the sturdy concrete foundation of the railway and its stone-pitching embankment, see Fig. 4.4c.

Among the potential driving mechanisms for the detected deformations (including seismic activity, glacier dynamics, and train loading) permafrost dynamics seems to be the most likely one. Continuing thaw settlement associated with an increase in soil temperature affects the formation of ice and brings about unstable conditions during initial thaw (Benn and Lehmkuhl, 2000). When soil thaws, water accumulated as ice

is released, leading to an increase in soil moisture content that will reduce the shear strength of the soil. As a result, the bearing capacity of man-made infrastructure (the QTR in our case) will be substantially reduced. The increasing thickness of the active layer found by Wu et al. (2012), could explain the linear velocity component, where lateral variability is related to the inhomogeneity related to slopes. Considering the combination of both linear as well as seasonal deformation, we believe that the active layer variability (both seasonal as inter-annual) is the most likely candidate hypothesis.

4.1.5. Conclusions

In this case study, we investigated the stability of the Qinghai-Tibet railway (QTR) in relation to permafrost dynamics. The results show that the analyzed segment of the QTR cannot be considered stable. We find inhomogeneous deformation along the track, with vertical rates of up to 10 mm/y. We also find seasonal displacements over a range of over 15 mm. Thus, using the SAR data time series, we are able to detect variability with characteristics similar as expected from permafrost dynamics, even though there is not enough ground truth to attribute the signal unambiguously to permafrost. Yet, it is evident that continuous satellite observations are of high value for the operational safety of the QTR, particularly in the permafrost region.

In the following section, a more in depth case study using high resolution SAR data from different viewing geometries will be presented. This aims at improving the applicability of satellite monitoring for rail asset management, by analyzing deformations in a track-fixed reference system.

4.2. Betuwe railway

In this case study that by using SAR measurements, we are able to detect mm-level changes in the track geometry with a bi-weekly measurement update and a high spatial resolution. When deformation of the infrastructure is mainly limited to the vertical and horizontal transversal direction, it is possible to derive the deformation vector. Section 4.2.1 gives a brief introduction to the theory of using InSAR for the monitoring of railway infrastructure. In section 4.2.2, a methodology for fine-tuning this InSAR technology to railway infrastructure for routine and near-real-time monitoring of spatio-temporal changes in geometry is presented. Also, the precision of the obtained deformation vector components is analyzed and described in terms of the variance-covariance structure. The method is demonstrated in section 4.2.3 on a segment of the Betuweroute, a freight railway heading from the Rotterdam harbor in the Netherlands towards Germany, eastwards, by using 248 TerraSAR-X SAR images acquired between 2009 and 2013, in a bi-weekly interval.

4.2.1. Introduction

On soft soils, the stability of railway tracks is a key safety and operational requirement (Esveld, 2001; Coelho et al., 2011; Varandas et al., 2014). Increasing traffic combined with higher speeds and axle loads requires special efforts in the maintenance of the geometry and position of ballasted railway tracks. One important issue in this respect is the early detection, identification and analysis of potential deformations along long

segments of the infrastructure. Especially for railway tracks that are in near-continuous use, it can be difficult to find time slots for laborious geodetic measurements (Roberts et al., 2004; Ma et al., 2011; Stiros and Psimoulis, 2012). In order to achieve wide-area and semi-continuous monitoring efficiently, Interferometric Synthetic Aperture Radar (InSAR) techniques (Curlander and McDonough, 1991; Massonnet et al., 1993; Hanssen, 2001; Hooper et al., 2007; Chang and Hanssen, 2012) can be applied. Using satellite-based InSAR measurements, we are able to detect are able to detect changes in the geometry of the tracks (Liu et al., 2011; Chen et al., 2012), up to millimeter precision (Ferretti et al., 2007), with a bi-weekly measurement update (Buckreuss et al., 2009; Covello et al., 2008), and a high spatial resolution (Bamler et al., 2009). When deformation of the infrastructure is mainly limited to the vertical and horizontal transversal direction, it is possible to derive these two components of the deformation vector by multi-track radar data (Wright et al., 2004; Ketelaar et al., 2007), albeit with a sensitivity that is dependent on the direction of the track. Here we analyze this precision and develop algorithms to tune this technology, termed satellite radar interferometry, to the case of railways. Compared to contemporary geodetic methods (e.g. tachymetry, leveling, or survey trains, our method allows for routine, systematic, and near-continuous monitoring on the potential risk of the railway tracks, in particular for spatio-temporal changes in geometry. Here we focus on the long term dynamic behavior of the tracks, and the transition zones between railways on free embankments and fixed substructures such as bridges and culverts, subject to localized differential settlement, by using a historical archive of SAR data.

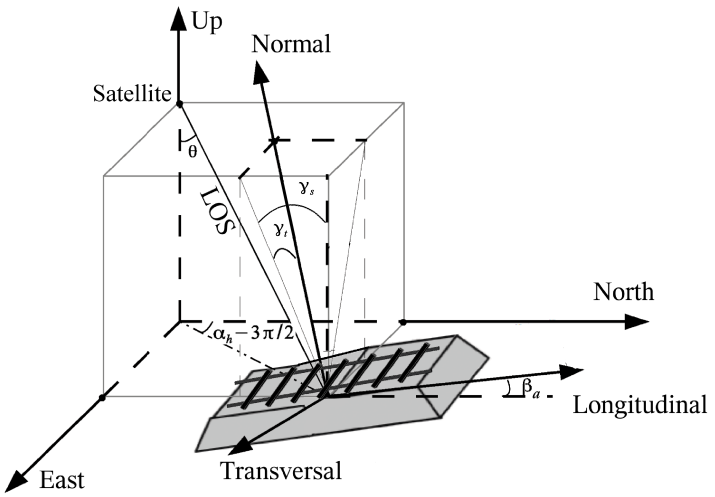

Figure 4.5: 3D deformation vector projection for railway tracks and embankments, from the radar line of sight (LOS) vector to a local Cartesian reference system. The main parameters involved are the azimuth direction of the track β_a, the slope γ_s, and the cant γ_t.

4.2.2. Method

Deformation monitoring with InSAR, see chapter 2, requires phase observations from coherent scatterers, which can be double-differenced to phase differences between two locations and two epochs. From this, differential displacements can be derived by multiplication of the phase differences with the radar wavelength (typically in the order of cm's) and correcting for the two-way travel of the radar pulse (Hanssen, 2001). The coherent scatterers (Ferretti et al., 2000b, 2001) are primarily reflected from targets which have stable phase values over time, such as buildings, bare rocks and rails. With a number of differential displacements at the sequential epochs for a given ground target, the temporal behavior presented as the deformation time series, is explored (Kampes, 2005; Ferretti et al., 2001; Chang and Hanssen, 2014).

Radar measurements are only sensitive to the projection of the (3D) deformation vector d_{geo} onto the radar line of sight (LOS), d_{LOS} (Hanssen, 2001; Kampes, 2005), see Fig. 4.5. In practice, a local geodetic coordinate system is used for the projection, defined as $d_{\text{geo}} = [d_e, d_n, d_u]^T$, containing the deformation components in East, North and Up direction, respectively, and centered at the target. The projection can be applied via $d_{\text{LOS}} = p^T d_{\text{geo}}$, where p is the projection vector

$$p = \left[-\sin\theta_{\text{inc}}\cos\alpha_h, \quad \sin\theta_{\text{inc}}\sin\alpha_h, \quad \cos\theta_{\text{inc}}\right]^T, \tag{4.3}$$

where the local incidence angle is denoted by θ_{inc}, and α_h is the instantaneous heading (azimuth with respect to the North) of the satellite track.

Fig. 4.5 depicts the 3D deformation vector projection from the radar LOS vector to a local Cartesian reference system. For a given location on the railway tracks (see Fig. 4.5) we convert the North-East-Up directions into a local, track-fixed, Cartesian reference system with $d_{\text{geo}} = R_1 R_2 R_3 d_{\text{track}}$ via rotation matrices

$$R_1 = \begin{bmatrix} \cos\beta_a & \sin\beta_a & 0 \\ -\sin\beta_a & \cos\beta_a & 0 \\ 0 & 0 & 1 \end{bmatrix}, R_2 = \begin{bmatrix} 1 & 0 & 0 \\ 0 & \cos\gamma_s & -\sin\gamma_s \\ 0 & \sin\gamma_s & \cos\gamma_s \end{bmatrix}, \tag{4.4}$$

$$R_3 = \begin{bmatrix} \cos\gamma_t & 0 & \sin\gamma_t \\ 0 & 1 & 0 \\ -\sin\gamma_t & 0 & \cos\gamma_t \end{bmatrix},$$

where $d_{\text{track}} = [d_{\text{T}}, d_{\text{L}}, d_{\text{N}}]^T$ spans a local, track-fixed, Cartesian right-handed coordinate system in the Transversal, Longitudinal, and the complementing Normal direction, respectively. Longitudinal and Transversal directions indicate the along and cross-track direction of the rails, respectively, and Normal indicates the orthogonal direction to Longitudinal-Transversal plane. We define the orientation of these axes using three angles, i.e., β_a, which is the azimuth of the track relative to the North, confined to $\beta_a \in [-90°, +90°)$ to avoid the directional ambiguity of the track direction; γ_s, which is the longitudinal slope of the track, defined positive for an uphill slope, and γ_t which can refer either to the cant of the track—which compensates for the centrifugal forces—defined positive for a track curving to the right, or to the slope of the side of an embankment, see Fig. 4.5. Note that in practice, train tracks have a maximum slope,

$|\gamma_s| \leq 4°$, and a maximum cant, i.e. $|\gamma_t| \leq 6°$ (Esveld, 2001). This implies that the normal deformation component d_N is almost identical to the Up deformation component d_u, and that R_2 and R_3 are close to the identity matrix—yet if high precisions are required they should be included.

With one satellite and a single viewing geometry, the estimation of the 3D deformation components based on the line-of-sight measurements is ill-posed, with three unknowns against one measurement. Therefore, it is impossible to determine the 3D deformation from a single satellite imaging geometry unless additional constraints can be introduced. However, a target on the ground may be observable from an ascending (north-heading) and a descending (south-heading) orbit, with two different heading orientations, $\alpha_{h,a}$ and $\alpha_{h,d}$, respectively, yielding two projection vectors p_a and p_d. This yields

$$\begin{bmatrix} d_{\mathrm{LOS},a} \\ d_{\mathrm{LOS},d} \end{bmatrix} = \begin{bmatrix} p_a^T \\ p_d^T \end{bmatrix} R_1 R_2 R_3 \, d_{\mathrm{track}} = P d_{\mathrm{track}}, \tag{4.5}$$

where P is a 2×3 projection matrix. The radar measurements in line-of-sight direction from ascending and descending direction are denoted as $d_{\mathrm{LOS},a}$ and $d_{\mathrm{LOS},d}$, respectively. As this system is still singular, and we may not have a third satellite viewing direction, we need to introduce constraints to resolve the system. Here we assume that the deformation is dominantly orthogonal to the longitudinal direction, that is, the longitudinal deformation component $d_L = 0$. Rewriting Eq. (4.5) to a linear system of observation equations, where we introduce $d_L = 0$ as an uncorrelated pseudo-observation with low variance, say $\sigma^2_{d,L} = 0.01$ mm^2, we write for the expectation operator E and dispersion D, respectively

$$E\{\underbrace{\begin{bmatrix} d_{\mathrm{LOS},a} \\ d_{\mathrm{LOS},d} \\ d_L \end{bmatrix}}_{d'}\} = \underbrace{\begin{bmatrix} p_{11} & p_{12} & p_{13} \\ p_{21} & p_{22} & p_{23} \\ 0 & 1 & 0 \end{bmatrix}}_{A} \underbrace{\begin{bmatrix} d_T \\ d_L \\ d_N \end{bmatrix}}_{d_{\mathrm{track}}}; \quad D\{\underbrace{\begin{bmatrix} d_{\mathrm{LOS},a} \\ d_{\mathrm{LOS},d} \\ d_L \end{bmatrix}}_{d'}\} = \underbrace{\begin{bmatrix} \sigma^2_{d,\mathrm{LOS}} & 0 & 0 \\ 0 & \sigma^2_{d,\mathrm{LOS}} & 0 \\ 0 & 0 & \sigma^2_{d,L} \end{bmatrix}}_{Q_{d'}}, \tag{4.6}$$

where p_{ij} are the elements of P, and the variance of the line-of-sight deformation measurement, $\sigma^2_{d,\mathrm{LOS}}$, is ideally estimated to be 1 mm^2 for the TerraSAR-X mission. This system of observation equations can be easily extended should other viewing geometries become available. In other words, the observable d_L in Eq. (4.6) can be substituted by the line-of-sight deformations from other viewing geometries and their corresponding variances can be assumed as $\sigma^2_{d,\mathrm{LOS}}$ as well. It is noted that the more number of observations d' that we have, the more accurate estimation for the unknowns d_{track} can be obtained.

To assess the achievable precision of deformation component estimates in the local track-fixed system, we produce the (co)variance matrix of $\hat{d}_{\mathrm{track}}$ using standard error propagation (Teunissen et al., 2005)

$$Q_{\hat{d}_{\mathrm{track}}} = (A^T Q_{d'}^{-1} A)^{-1}. \tag{4.7}$$

Fig. 4.6 illustrates the sensitivity of the rail track parameters β_a, γ_s and γ_t. The setting of these parameters refer to the characteristics shown in Tab. 4.2, and a LOS variance

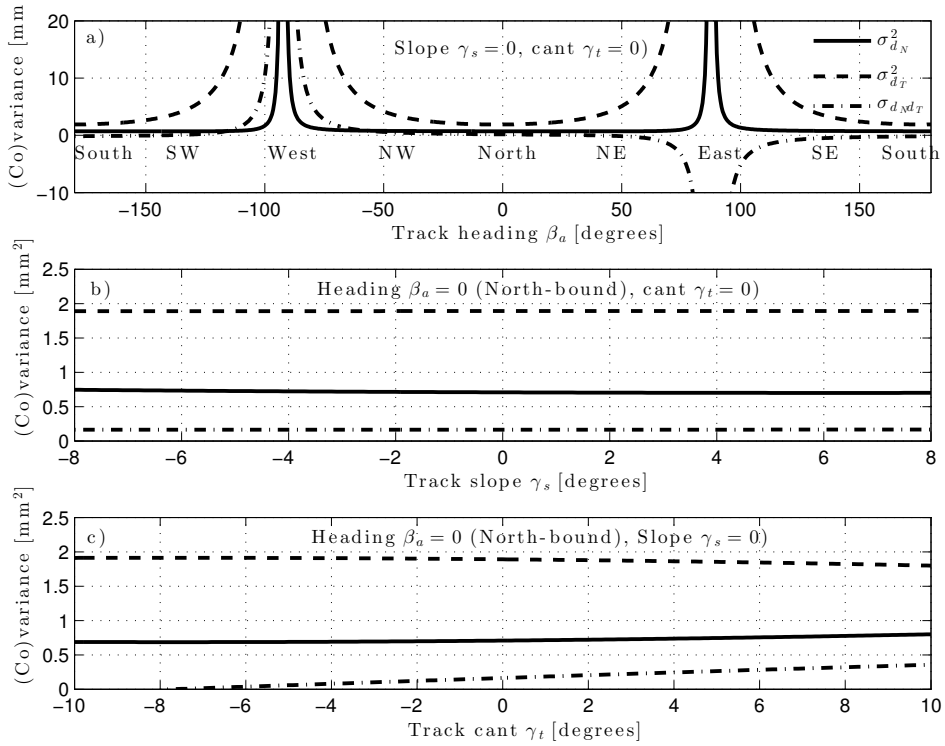

Figure 4.6: Sensitivity of rail track parameters (β_a, γ_s, γ_t), expressed using the variances of the normal (near-vertical) component, $\sigma^2_{d_N}$, the transversal component, $\sigma^2_{d_T}$, and the covariance σ_{d_N,d_T}.

$\sigma^2_{d,\mathrm{LOS}}$ and the pseudo-observation variance $\sigma^2_{d,\mathrm{L}}$ are assumed as 1 mm^2 and 0.01 mm^2, respectively. With a varying β_a and fixed $\gamma_s = \gamma_t = 0$, Fig. 4.6a shows the corresponding variance for $\sigma^2_{d_N}$, $\sigma^2_{d_T}$ and covariance $\sigma_{d_T d_N}$. It shows that $\sigma^2_{d_N}$ can always be better estimated than $\sigma^2_{d_T}$, and an east-west heading track, that is $-95° < \beta_a < -90°$ and $85° < \beta_a < 90°$, results in a poorly estimable normal (near-vertical) component, i.e. $\sigma^2_{d_N} > 9$ mm^2. For the lateral component the dead-bands lie in $-120° < \beta_a < -66°$ and $60° < \beta_a < 115°$. Note that the covariance indicates a strong correlation between both components. Best estimates are obtained for north-south heading tracks, see also Figs. 4.6b and 4.6c, showing a variance of less than 1 and 2 mm^2 for the normal and transversal component, respectively. These figures also show that the effect of varying slopes, γ_s, and cants, γ_t, is only marginal.

To jointly analyze the ascending and descending phase measurements, both in their own relative datum, they need to be referenced to a common datum, the so-called datum connection. A common reference area with sufficient coherent scatterers is required. We apply a spatially moving window with a given window size to find an area where the temporal behavior of all coherent scatterers is homogeneous. The average deformation for every epoch of all these points is considered as the common refer-

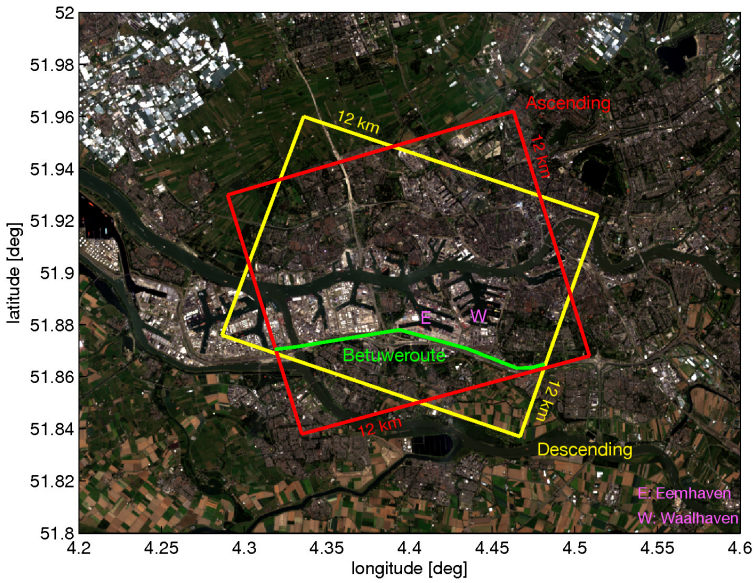

Figure 4.7: The 12×12 km cropped image areas on the top of the Landsat-8 imagery, for the ascending and descending orbits. A part of the Betuweroute is marked in green.

ence for all the other points, considering the conversion for different ascending and descending viewing geometries. In general, different sensors capture different physical targets (Ketelaar et al., 2007), which hampers interpretation. Therefore, two scatterers imaged from different orbits, with a distance less than e.g. 3 m are assumed to stem from the same physical object. Such targets can then be used to estimate deformation in the track coordinate system from their LOS observations, following Eq. (4.5).

4.2.3. Results

A part of the Betuweroute close to Rotterdam, the Netherlands is used as test site, see Fig. 4.7. The Betuweroute is a double track freight railway heading from Rotterdam towards Germany which was finished in the middle of 2007. It serves a daily average of 150 freight trains with a 6000-ton loading capability. Due to the very soft peat and clay soils, and the increase of traffic frequency, it is extremely important to monitor the stability or deformation of the rails and detect anomalies such as differential displacements and the buckling of the rails, at an early stage to ensure the safety of the operations. We use 116 ascending and 132 descending stripmap-mode images from TerraSAR-X acquired between April 2009 and July 2013, see Tab. 4.2. The cropped image areas for both ascending and descending orbits cover 12×12 km, as in Fig. 4.7 with the rectangles. A part of the Betuweroute, denoted as line AB, lies in the overlap region of these two cropped image areas.

By using the persistent scatterer interferometry (PSI) technique (Ferretti et al., 2001; Kampes, 2005; van Leijen, 2014), we compute line-of-sight deformation time series,

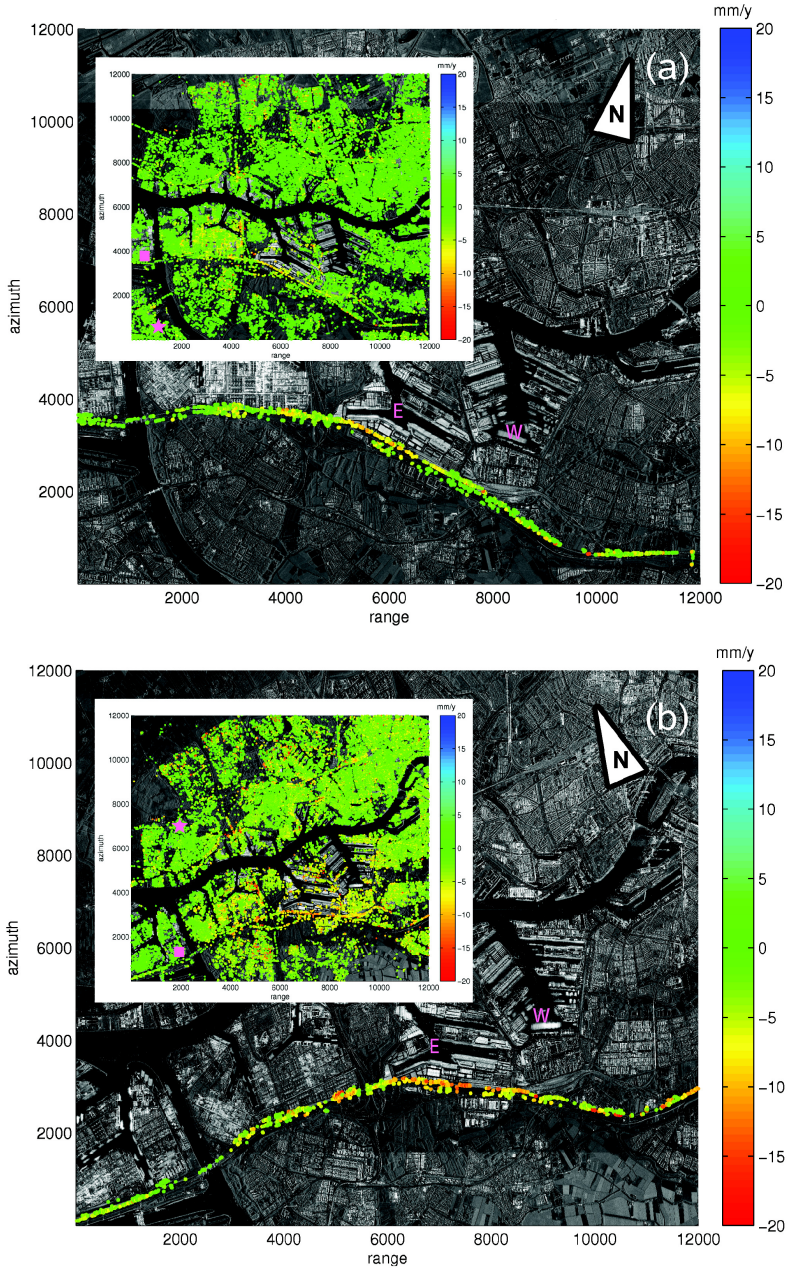

Figure 4.8: Deformation velocity map (LOS) superimposed on a temporally averaged reflectivity map from ascending (**a**) and descending (**b**) orbits in radar coordinates.

particularly for the persistently coherent scatterers (PS), from the ascending and descending orbits. Figs. 4.8a and 4.8b depict the line-of-sight deformation velocity map superimposed on a temporally averaged reflectivity map from the ascending and descending orbits in radar coordinates. In each figure, the deformation velocities along a part of the Betuweroute are filtered out whilst the subfigure on the top-left provides the entire deformation velocity map. Even though the colorbar covers a rather wide range from -20 mm/y to +20 mm/y, it is clear that both datasets detect significant deformation, e.g. due to subsidence or consolidation of the track south of the harbor area (i.e., Waalhaven and Eemhaven, which are indicated by the purple W and E, respectively). The reference area for each dataset is selected individually in the PSI processing, marked by the purple star.

Table 4.2: TerraSAR-X satellite datasets used in analysis

Stack	Track/Frame	Heading	Incidence Angle	Start/End Date	Acquisitions
Asc	t025_T172643	350°	39.2	2009–2013	116
Desc	t048_T060823	192°	23.5	2009–2013	132

To connect the ascending and descending results, we bring them into a common datum by defining a reference area of 500×500 m. The common reference area that is squared in purple in Fig. 4.8, has a near-zero average deformation rate and minimal deviation. We focus on the main railway tracks within the overlap area, that is the line AB. Considering the most relevant deformation components to be in the normal (near-vertical) and lateral direction—the longitudinal component has less impact on the safety of the rail—the deformation decomposition using both ascending and descending datasets and Eq. (4.6) is applied to estimate the normal, d_N, and transversal, d_T, components, see Fig. 4.9. Note that we downsample the grid in geodetic coordinates and assume that ascending and descending observations within a grid cell stem from the same target. Here in our case, the downsampled grid size in north and east direction is 5 m. The parameters β_a, γ_s and γ_t in the rotation matrices of Eq. (4.5) are specified for every segment of the railway.

We produce the cumulative normal d_N and transversal d_T spatial deformation map over time using TerraSAR-X InSAR data time series acquired from ascending and descending orbits for the line AB, see Figs. 4.9a and 4.9b, and also produce the deformation velocities profile in the normal and transversal directions, as in Figs. 4.9c and 4.9d. For all figures, the horizontal axes express the distance [m] along the track w.r.t. point A. The vertical axes for Figs. 4.9a and 4.9b show the cumulative deformation relative to the first image-acquisition date, 6 April 2009. The profile in Fig. 4.9a shows that a significant normal deformation area, with more than 5 cm of cumulative displacement in the analyzed time period, is detected in the 5 to 7 km distance segment (in Vondelingenweg segment). Transversal displacements, see Fig. 4.9b, appear to be small, but clear discontinuities can be observed that can be indicative for high-strain areas, in particular when correlated with the normal components. Note that the discrete discontinuities in both normal as well as transversal directions may relate to the transition zones between free embankments and fixed substructures such as bridges and culverts (Coelho et al., 2011; Varandas et al., 2014). Figs. 4.9c and 4.9d show the estimated velocities

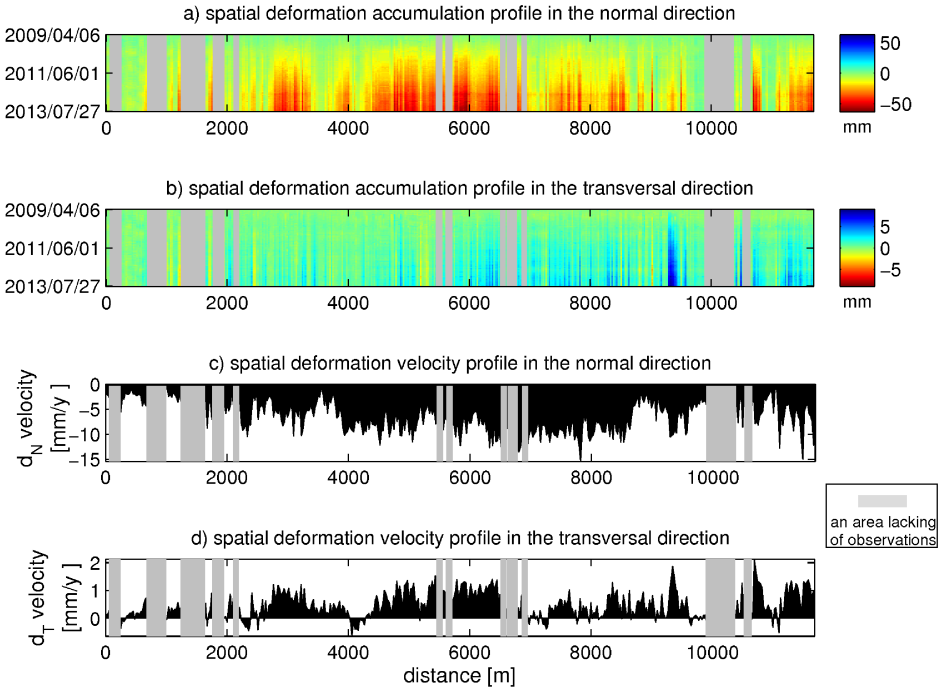

Figure 4.9: Spatial profile for the deformation accumulation and the deformation velocity for the normal d_N and transversal d_T components, over the line AB.

per line segment, demonstrating that the strongest normal deformation velocities are detected in the Vondelingenweg segment, south of the harbor, while the behavior in the transversal direction is less pronounced. Note that the gray mask indicates the segments lacking PS observations.

To express the quality of the deformation component estimates in the local railway track-fixed coordinates, error ellipses are computed based on the (co)variance derived from Eq. (4.7). In our case, $\text{diag}(Q_{d'}) = (9, 9, 0.01)^T$ [mm^2] considering the viewing geometry of the TerraSAR-X data. We randomly show a limited number of PS estimates along the track, relative to point A, to illustrate the corresponding 95% confidence interval error ellipses. These are shown in Fig. 4.10, superimposed on the Landsat-8 imagery. In Fig. 4.10A, the final total deformation vector [mm] per estimate is indicated with a white vector by its normal (N, along the vertical axis) and transversal (T, along the horizontal axis) components. The top subfigure gives the corresponding PS (marked by the red dots) location distribution along the track in terms of the distance w.r.t. point A. Since the normal components are dominant, most deformation vectors are close to the vertical direction. The error ellipse in magenta per estimate shows the confidence interval [mm], the precision of the two components and their correlation,

via the ellipse size and orientation. Thus, signal-to-noise ratios and significance can be assessed by comparing the length of the vector and the size of the ellipse, from this figure. The separate normal and transversal components with their errors are shown in Figs. 4.10B and 4.10C, respectively. These indicate that the track segments south of the Waalhaven and Eemshaven harbors (see the green square area in Fig. 4.10B) have significant normal deformation probably due to the heavy loading of the train track, and in the transition zones significant normal deformation is detected as well. Transversal deformations are marginal but relevant. Moreover, according to the results of the error ellipses, the uncertainty in the normal direction is generally less than the one in the transversal direction, which implies that the estimates in the normal direction are more reliable than the ones in the transversal direction. In order to validate our results, we compared our results with in situ survey train measurements, see Fig. 4.10D. Only a 1 km segment was made available for the comparison. The required vertical uplift for the railway track per 10 m in this segment (w.r.t. the measured track height in 2004) was computed by the survey train measurements and performed in January 2013. Every uplift estimate is marked by a blue cross. The normal linear deformation rates for the PS points within this segment are shown in black. Around the 5.25 km indicator, the comparison shows that the locally faster subsiding areas require a bigger uplift, and vice versa. Between the 5.25 to 5.4 km distance segment, the uplift values approach to zero, while the behavior of the PS points in this area is spatially homogeneous, representing the small variation of their deformation rates. Particularly, the uplift values in the 5.45 to 5.7 km distance segment are more than 50 cm. The deformation rates of the PS points in this area are strongly varying and considerably increasing. After the 5.7 km distance, the uplift values are still proportional to the deforming rates of the PS points. The comparison demonstrates that the uplift values of the railway track are highly correlated with the normal deformation rates observed by the satellite. This suggests that spatially anomalous deformation detection and the maintenance of the railway tracks can be assisted by satellite-based InSAR monitoring.

4.2.4. Conclusions

The satellite InSAR measurements of railway tracks presented here prove to be adequate to significantly estimate displacement time series in the lateral and normal (near-vertical) direction, with millimeter precision, assuming the absence of longitudinal deformation. We derived the decomposition equations to convert satellite line-of-sight displacement measurements to a local Cartesian track-fixed coordinate system, showing how observational errors propagate into the estimates. The sensitivity of the techniques using the TerraSAR-X imaging geometry of ascending and descending orbits, was shown to have dead-bands where the sensitivity for displacement estimates is low. The method is tested on a segment of the Betuweroute, in the Netherlands, using 248 TerraSAR-X satellite images acquired between 2009 and 2013, with a bi-weekly interval. The results show that track segments south of the Waalhaven and Eemhaven harbors are subject to significant vertical displacements, up to 5 cm, most likely due to settlement or compaction. Moreover, sudden abrupt changes in displacements along the track suggest transition zones between free embankments and fixed substructures such as bridges and culverts, subject to localized differential settlement. Transversal

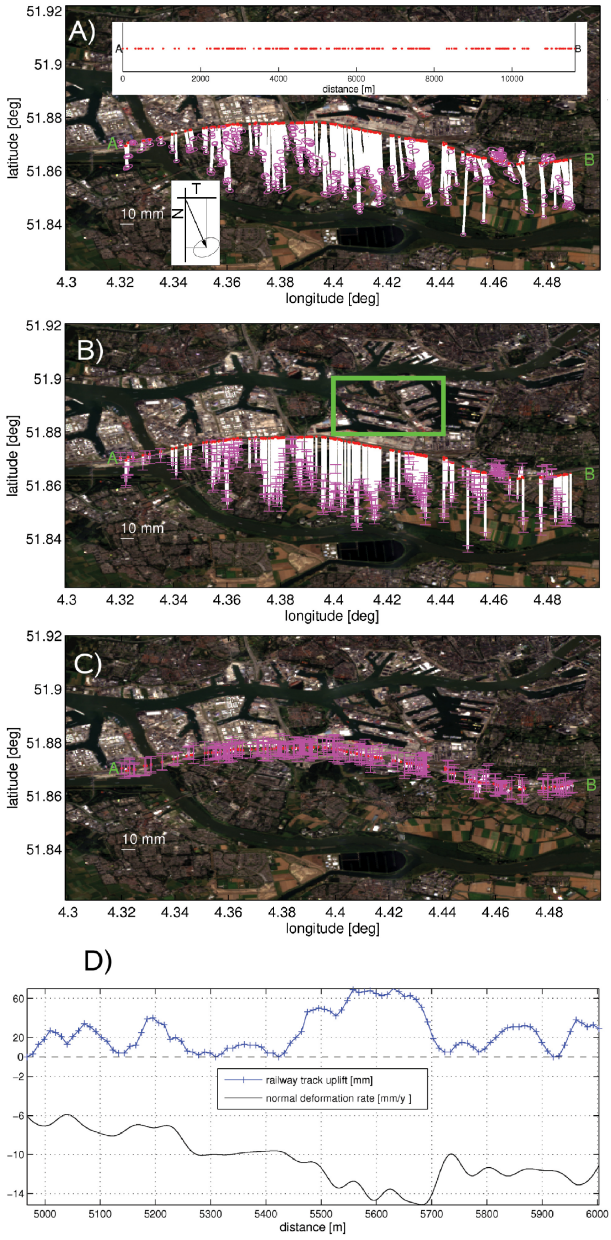

Figure 4.10: Quality of the deformation estimates for (**A**) the total deformation vector, (**B**) the normal and (**C**) transversal deformation components. (**D**) The comparison between the survey train measurements and InSAR results for the 1 km segment.

displacements are dominantly in the northward direction. Furthermore, according to the comparison between survey train measurements and our results in a 1 km segment, the large railway track uplift area corresponds with a considerable normal subsidence. In the case of using TerrSAR-X SAR data, the methodology demonstrated here can be used to improve the efficiency of managing rail infrastructure, enabling a systematic monitoring, which could be deployed to provide semi-continuous (bi-weekly) status updates.

4.3. Summary

In this chapter, we applied time series InSAR techniques to two different study sites: the Qinghai-Tibet Railway (QTR) and a segment of the Betuweroute, in the Netherlands. We demonstrated the feasibility of monitoring railway infrastructure using the satellite techniques in both rural and urban environments. We developed methodology to improve the capability for operational railway infrastructure monitoring.

In a rural environment, particular in a dynamic environment (snow, ice), such as in the QTR case, we applied a point-selection method using an adaptive directional window filter, to optimize the amount of InSAR measurement points over the railway. The kinematic time series of those InSAR measurement points (derived from PSI processing) were used to explore the temporal behavior of the railway. We also applied a sinusoidal function to account for seasonal variations, and found strong indications for permafrost-related railway dynamics.

In an urban environment, such as the Betuweroute case, we derived the decomposition equations to convert radar line-of-sight displacement measurements to a local Cartesian track-fixed coordinate system, using multi-track SAR data. We described the quality of the deformation component estimates in the local Cartesian track-fixed coordinate system based on the variance-covariance structure. We also demonstrated that our InSAR results fit well with in situ survey train measurements.

5
Building Monitoring

This chapter will focus on structural health monitoring of a single building. We show a *forensic* research using InSAR techniques on the near-collapsed building *'t Loon* due to a developing sinkhole, related to previous underground mining activities. We present the PSI application on monitoring the structural health of building *'t Loon*, showing how multi-track SAR data (ERS-1, ERS-2 and Envisat and Radarsat-2) can be converted into the identical system, how to obtain the precise PS geolocation aided by lidar-based DSM data, and how to hypothesize the driving mechanism of the ground anomalous deformation.

5.1. Introduction

Upward migrating cavities of both natural or anthropogenic origins are an important hazard in many parts of the world, able to cause sudden cover-collapse leading to sinkholes (Coker et al., 1969; Newton et al., 1973; Lamoreaux and Newton, 1986; Caramanna et al., 2008; Galve et al., 2009; Tolmachev and Leonenko, 2011). Moreover, rising population densities in sinkhole-prone areas, in combination with media attention using public video surveillance and private cell phone video, have increased public awareness (Meng, 2013; CNN, 2014; Schwartz, 2013; Wines, 2013). Apart from sudden collapse sinkholes, the consequences of migrating cavities include the lack of support of building foundations, drainage of water bodies, and the deformation or destruction of water defense systems or critical infrastructure (Gutiérrez et al., 2009).

The chief problem in the assessment of sinkhole risk is the lack of a priori knowledge on the location of the cavity (Baer et al., 2002; Wust-Bloch and Joswig, 2006). Although in situ measurements, such as gravimetry (Colley, 1963), seismic (Cook, 1965) or electromagnetic surveying or ground-penetrating radar (Beres et al., 2001; Mochales et al., 2008), are in principle able to detect an underground void, it is not economically possible to use these techniques over vast areas. Moreover, the risk of fatalities is highest for urbanized areas (Bezuidenhout and Enslin, 1970; Frumkin and Raz, 2001), in which the built-up environment prevents getting close enough to perform these measurements. The second problem is that there is usually no data available preceding a collapse, so it cannot be assessed whether there was precursory motion, and how far ahead in time critical levels can be detected. Here we investigate the use of satellite radar interferometry to detect minute signs of impending sinkholes (Abelson et al., 2003; Nof et al., 2013). In particular, we hypothesize that precursory deformation may be occurring before sinkhole formation, potentially detectable as relative displacements using radar satellites. As this hypothesis can only be tested empirically

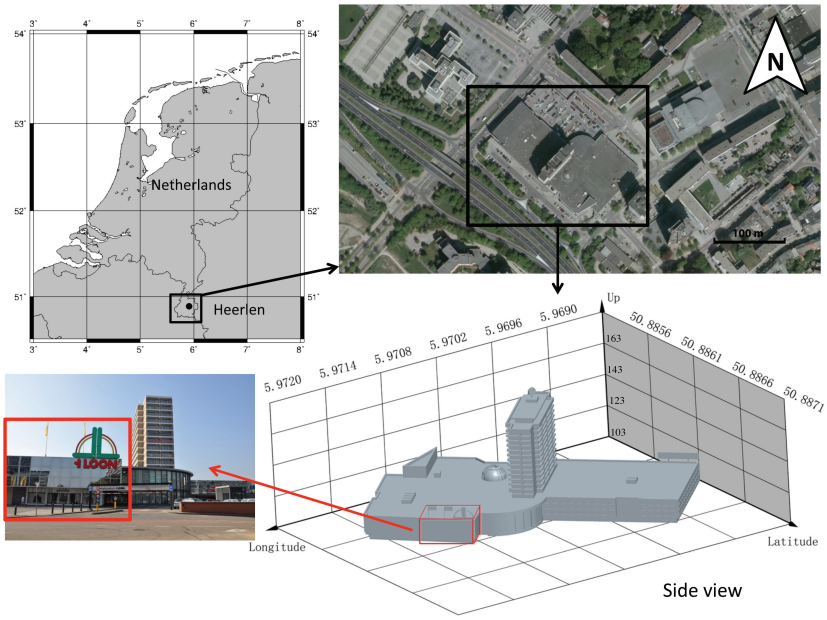

Figure 5.1: Location of the study area (Heerlen, the Netherlands) and the shopping mall from airborne imagery. A 3D model of the building at the lower right was constructed using airborne lidar-based data and photographic information, see Fig. 5.3 and the ground-view photo on the lower left. The area indicated by the red square was subject to the localized subsidence. Aerodata 50°53′10″N and 5°58′13″E.

using case studies we choose a near-collapse event of a shopping mall in Heerlen, the Netherlands, to investigate the efficacy of the method. Even though a successful case study does not prove generic applicability of the approach, it is crucial to expand the scarce empirical material available.

5.2. Study area and near-collapse event

From the late 19th century to the mid 1970s, coal mining took place in the Heerlen area, in the southeastern Netherlands, see Fig. 5.1 (Messing, 1988; Westen, 1971). The extraction of coal caused up to several meters subsidence of the surface, leading to damage to the build-up environment (Caro Cuenca and Hanssen, 2008; Caro Cuenca, 2012). After the discovery of large reserves of natural gas in the north of the country, mining ceased abruptly, and shafts and galleries were backfilled and abandoned, but possibly leaving cavities. When the overburden of the mine galleries would collapse, such cavities could migrate upwards over time and eventually reach the surface.

Shopping mall and apartment building *'t Loon* in Heerlen, see Fig. 5.1, was built in 1965, as it later appeared some 90 m above an abandoned mining gallery. In June 2011, movements were occurring in the structure of the mall, and periodic surveys were performed to monitor their behavior (Engelbertink et al., 2012). Late August 2011, cracks

were observed in the columns supporting the car park below the mall, leading to the installation of support constructions and further investigations. November 29th, a significant crack was observed in the head of column D18, see Fig. 5.2, and parts of the floor and facade had deformed. A part of the mall was evacuated. December 3rd, an 8 m wide and 1.5 m deep sinkhole occurred beneath column D18, marked in red in Fig. 5.2 (Hordijk, 2012). The entire complex (mall and apartments) was evacuated. The municipality decided to demolish the part of the mall that was constructively affected.

In the analysis of the event, several hypotheses were formulated on the driving mechanisms for the sinkhole, such as (i) coal mining activities between 1950 and 1956, (Parise, 2012) (ii) rising mine water, (iii) surface water run-off, (Sinclair, 1982) (iv) karst dissolution, (Parise and Lollino, 2011) and (v) tree roots and the flushing of a broken sewer system, where it was recognized that it could also be a combination of mechanisms (Roest, 2012).

In this study, we use the Heerlen events to investigate the value of satellite radar data archives to detect potential sinkhole-prone locations over build-up areas, to assimilate various data sources, and to analyze the spatio-temporal information retrieved from the data. In section 5.3 we discuss the applied methodology for multi-sensor data processing and precise geolocation, followed by the results and interpretation in section 5.4. Section 5.5 is dedicated to the Conclusions.

5.3. Methods

In order to investigate the hypothesis of precursory deformation preceding sinkhole occurrence, we jointly use the SAR data archives of four radar satellites (ERS-1, ERS-2, Envisat, and Radarsat-2) over a period of close to 20 years. We then apply radar interferometry via time series analysis using a persistent scatterer interferometry (PSI) method (Ferretti et al., 2001; Kampes, 2005). This yields estimates of the relative one-dimensional motion of time-coherent scatterers, here termed PS, in the radar line of sight (LOS) (Ferretti et al., 2000b; Hanssen, 2001; Ketelaar, 2004). The periodically acquired SAR images are then used to retrieve the deformation time history. In our case, we applied a joint multi-sensor approach for the four SAR satellites and optimized the geolocation of PS points using external lidar-based digital surface model (DSM) data.

5.3.1. Joint multi-sensor processing

In this study, we use 69 ERS-1/2, 71 Envisat and 20 Radarsat-2 stripmap SAR images acquired all from descending orbit geometries between April 1992 and October 2011. By using the Delft implementation of Persistent Scatterer Interferometry (*DePSI*) (Kampes, 2005), the PS deformation time series for these four satellites are produced. We use precise orbit data with precisions better than 15 cm, (for Radarsat-2 after readjustment, see Bahr and Hanssen (2012)), and remove acquisitions with perpendicular baselines greater than 850 m. Unwrapping is performed using integer bootstrapping, see Kampes and Hanssen (2004b). In first instance, the deformation time series of PS in every dataset are relative to an arbitrary selected PS reference point. Moreover, the incidence angles vary for each satellite system, i.e. 23°, 21.6°, and 33.3° for ERS-1/2, Envisat and Radarsat-2, respectively, which causes different projections of the defor-

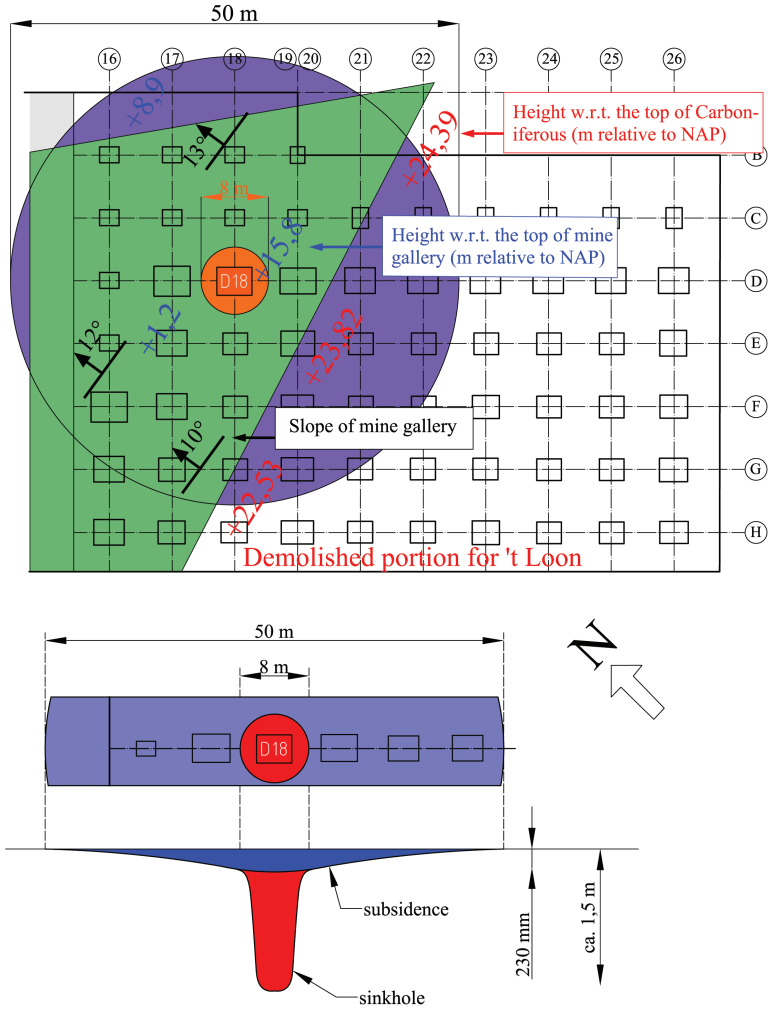

Figure 5.2: Schematic drawing of ground subsidence (purple) and sinkhole (red), and coal mining map under *'t Loon*. The rectangles in the top figure represent the concrete foundation elements. The light green area outlines the end of a mine gallery of the Oranje Nassau mine. The blue numbers show the height of the ceiling of the gallery, while the red numbers represent the height of the top of the carboniferous layer, both relative to the Dutch national vertical datum (known as 'NAP'). The difference between these numbers indicates that the carboniferous layer was very thin (less than 8 m) above the gallery, thus increasing the collapse risk. The black numbers and vectors show the dipping angle of the gallery. The bottom figure is a cross section over the center of the subsidence area. (Figure adapted from (Hordijk, 2012))

mation to the vertical direction. Thus, as the PS results from different satellites are in different local datums, a datum transformation is applied to align them into a uniform datum. For each satellite InSAR data stack, we introduce a standard interferometric functional model w.r.t. an individual reference PS point,

$$\phi_{0P}^{k} = \phi_{P}^{k} - \phi_{0}^{k} = \phi_{0P}^{k,\mathrm{topo}} + \phi_{0P}^{k,\mathrm{defo}} + \phi_{0P}^{k,\mathrm{atmo}} + \phi_{0P}^{k,\mathrm{n}}, \tag{5.1}$$

where ϕ_{0P}^{k} is the interferometric phase for point P w.r.t. reference point 0 in interferogram number k, and $\phi_{0P}^{k,\mathrm{topo}}$ represents the height phase residual after removing the main part of the topographic contribution via a coarse (90 m) resolution DEM (SRTM, (van Zyl, 2001)). The term $\phi_{0P}^{k,\mathrm{defo}}$ represents the relative deformation between point P and point 0. The differential atmospheric delay component is $\phi_{0P}^{k,\mathrm{atmo}}$, and the noise is $\phi_{0P}^{k,\mathrm{n}}$.

To correct the difference in reference point 0 per dataset, we manually select a persistent scatterer R (i) that could be uniquely identified in each time series, (ii) that exists over the entire data acquisition time period as a joint PS reference point in all the SAR datasets, (iii) which is far enough outside the area of interest, and (iv) which is far enough outside the wider uplift area due to the rising water tables after termination of the mining activities, located farther north, see Caro Cuenca et al. (2013). Moreover, within the vicinity of R, PS points show homogeneously constant velocities, suggesting that the reference area is sufficiently stable. Subsequently we convert all the PS points into a same coordinate system using

$$\phi_{RP}^{k} = \phi_{0P}^{k} - \phi_{0R}^{k}, \tag{5.2}$$

whilst the deformation parts are converted as well by $\phi_{RP}^{k,\mathrm{defo}} = \phi_{0P}^{k,\mathrm{defo}} - \phi_{0R}^{k,\mathrm{defo}}$. The relative height residuals w.r.t. point R as well as the atmospheric delays are estimated with sufficient precision due to the number of available SAR images (Chang and Hanssen, 2012). However, for a more precise absolute geolocation of the PS points of interest—in order to link the points to a specific part of the structure—we need a shared absolute reference level.

5.3.2. Precise geolocation of PS points aided by lidar DSM

A precise geolocation of PS points w.r.t. buildings and infrastructure is needed to avoid an erroneous interpretation of the driving mechanisms (Perissin, 2006). It requires the sub-pixel positioning of the peak of the impulse response function, here applied using oversampling. With a ground resolution of 20 m in range and 4 m in azimuth (for ERS and Envisat), the positioning precision is in the order of about 1 m. The interferometric uncertainty of the relative vertical positioning in PS techniques is around 1 m as well (Perissin, 2006). However, inaccuracies in the master satellite orbit and clock, absolute atmospheric delays and various geophysical parameters (such as solid Earth tides, plate tectonics and loading) cause a systematic error that biases the geolocation up to a few meters (Eineder et al., 2011). This hampers the attribution of the observed PS to a specific part of a building or structure.

To iteratively improve the geolocation for DePSI-derived PS results, we use ground control points (GCPs) for the horizontal positions and correlate them with external li-

dar measurements for the vertical. As GCPs lamp posts are used, which show a clear and unique reflection in the radar image. Subsequently, for the vertical positions, a highly accurate lidar-based DSM, containing both terrain as well as building heights, is used to compute the offset between PS and DSM height distribution histograms over a wider region of 10 × 10 km. As the absolute height offset is identical for all PS, and the horizontal position of the PS is already corrected for using GCPs, this procedure has the advantage that the radar line-of-sight geometry is not relevant anymore. This process of horizontal and vertical offset estimation is repeated until convergence is reached.

The DSM, referred to as the Actual Height model of the Netherlands (AHN), is lidar-based. It was acquired between 1997 and 2007 and processed to a product with a posting of 5 m and a vertical precision (absolute and relative) of 15 cm (van der Zon, 2013).

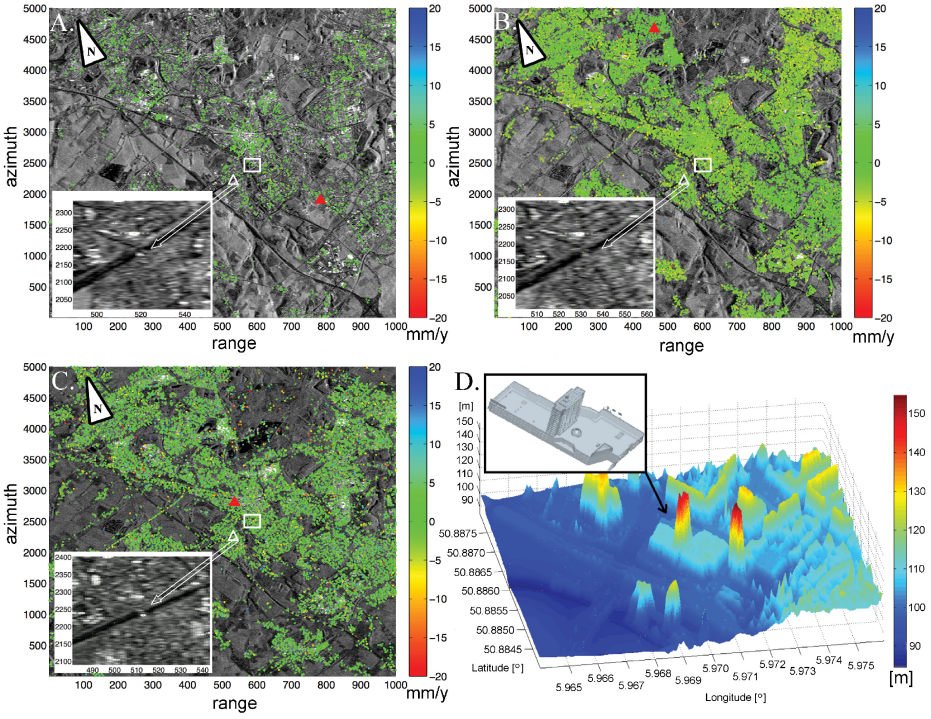

Figure 5.3: Line-of-sight PS deformation maps for ERS-1/2 (A), Envisat (B), and Radarsat-2 (C). Area size is 10×10 km. The reference point is different for each dataset, indicated by the solid red triangle. The joint reference point is marked by the open white triangle, the zoom around this point is shown in the inset figures. Shopping mall *'t Loon* is within the white rectangle. (D) Lidar-based 3D point cloud of the mall and its surrounding. The inset shows the 3D building model.

5.4. Results and discussion

Line-of-sight PS deformation maps are produced via individual PSI processing for ERS-1/2, Envisat and Radarsat-2, see Fig. 5.3A, 5.3B and 5.3C, respectively. The reference point is different for each dataset, indicated by the solid red triangle. To merge the PS time series, we select a joint reference point with constant amplitude behavior in all SAR datasets, see the open white triangle and the zoom around this point in the inset figures. Shopping mall *'t Loon* is within the white rectangle. Based on DSM data, we then show the interpolated 3D point cloud of the mall and its surroundings in Fig. 5.3D. Note the effects of smoothed building edges due to the interpolation of gridded point data. The inset shows a 3D building model derived assuming parallel facades and orthogonal angles, in combination with photographic information (ProEngineer software).

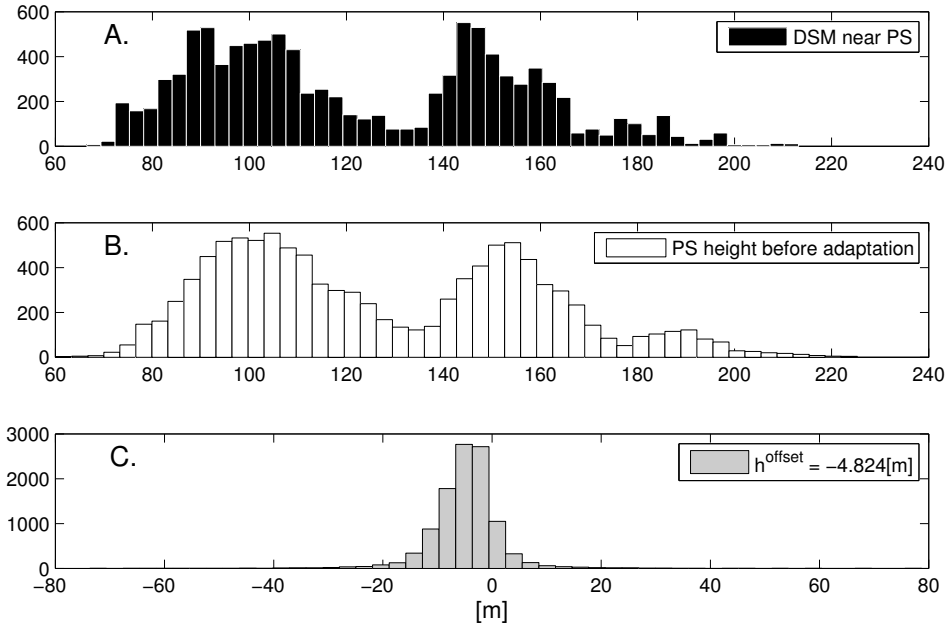

Figure 5.4: Histograms of lidar-based DSM data and PS heights before offset correction, and the offset between lidar and PS heights for Envisat (10×10 km). A.) Distribution of DSM height close to PS points. B.) Original distribution of PS height. C.) Height offset distribution between DSM data and PS height, and the mean offset value $h^{\text{offset}} = -4.824$ m.

The lidar-based DSM height correction, cf. section 5.3.2, is applied to correct for the height offset of all PS points. Fig. 5.4A shows the histograms of lidar-based DSM points selected close to PS points (< 5 m, horizontal), and B shows the histogram of these corresponding PS heights. Fig. 5.4C shows the height offset distribution, indicating an estimated mean offset of $h^{\text{offset}} = -4.824$ m. This yields the adapted heights of the PS. It should be noted that the applied method for offset estimation is not perfect, as the corresponding radar and lidar points may stem from different objects. However, by

applying this method over thousands of points we obtain a reasonable offset, of a few meters. After offset estimation, we can classify points as stemming from the roof or from the ground. In Fig. 5.5 we interpolate both classes separately, since intra-building displacements may be independent of land surface displacements. The locations of the observation positions are indicated in the figure (squares for roof and circles for ground positions) to visually assess the impact of interpolation uncertainty. We applied Ordinary Kriging, which allows for producing prediction error maps as well.

After projecting all LOS displacements onto the vertical direction, the deformation velocities of PS points are time variable, indicated by different color bar ranges in Figs. 5.5A, 5.5B, and 5.5C. The figure shows unambiguously that the observations stemming from the roof behave independently from observations from the surrounding ground area. Note that we have assumed that all displacements are mainly vertical, as we do not have complementary ascending orbits to decompose the displacement vectors. Nevertheless, a common decomposition direction is required in any case to allow for the comparison of data with different incidence angles.

In the last couple of years shown in Fig. 5.5C, the vertical deformation in the near-collapse area increases by a factor of three, up to a velocity of 15.6 mm/y. For two representative points, indicated with PS1 (maximum deformation) and PS2 (stable), Fig. 5.6 shows the deformation time series. For PS1, the average deformation rate is 3.3 mm/y during the first 18 years. Two accelerations are observed: between October 2005 and June 2006, and in the summer of 2010. During the latter, a strong acceleration occurred, with an additional 2.1 cm displacement preceding the final failure of the garage structure. In total, 8 cm of vertical deformation is observed over the entire period of 20 years. Considering interpolation uncertainty, the differential displacements appear over a horizontal distance of less than 20–40 m, which implies that a shear strain of more than 2–4 millistrain was built up, or a shear strain rate of more than 100–200 microstrain per year.

From Fig. 5.6 we observe that the noise levels are higher for the ERS-1/2 time series than for the Envisat/Radarsat-2 data. Nevertheless, all estimates are still far below the ambiguity levels of 3.07, 3.02, and 3.32 cm (vertical projection) for the satellites ERS-1/2, Envisat and Radarsat-2, respectively. This implies that the two observed accelerations of PS1 cannot be due to phase unwrapping errors. Moreover, the fact that PS2 does not show the acceleration in the summer of 2010, in conjunction with the start of the Radarsat-2 series, proves that the observed acceleration is not due to instable reference points or noise in the data.

These data suggest a gradual motion, possibly the upward migration of a cavity, observable at least two decades before the 2011 collapse-sinkhole events. In the following, we will discuss the driving mechanism hypotheses and time-line based on the local geological condition.

The subsurface of Heerlen is sampled by core drillings performed on-site after the collapse (Heitfeld et al., 2012). From the top down, this consists mainly of sandy material, (Rupel and Tongeren formation) see Fig. 5.7, followed by limestones (Maastricht formation) and the carboniferous layer where the mined coal seams are located. Two important observations followed from the core drilling. First, between Rupel and Tongeren there is a shallow impermeable clay layer, known as the Goudsberg member,

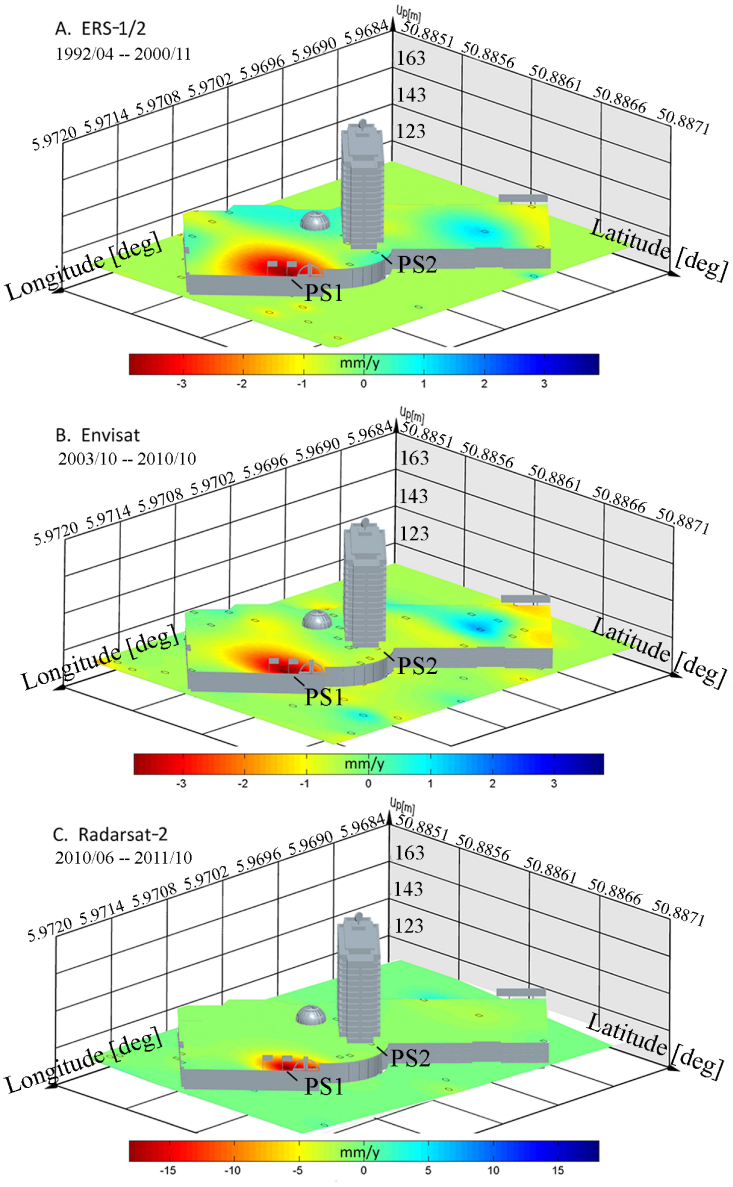

Figure 5.5: Interpolated PS velocity maps, projected onto the vertical direction, from ERS-1/ERS-2 (1992/04–2000/11), Envisat (2003/12–2010/10), and Radarsat-2 (2010/06–2011/10). Interpolation using Ordinary Kriging is applied independently for the roof areas and the ground areas, as these are not necessarily correlated. The original PS points are plotted to visually assess the influence of interpolation uncertainties. Ground points are marked with circles and roof points with squares. Note the wider color bar range in C for the Radarsat-2 data.

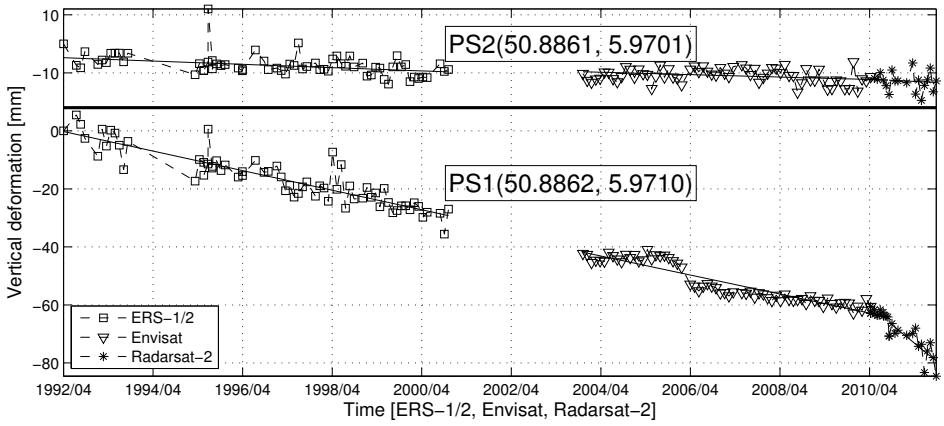

Figure 5.6: Temporal distribution of radar acquisitions and deformation time series of two PS (locations indicated in Fig. 5.5). PS1 is within the collapse-sinkhole area, with relatively large velocities, while neighboring PS2 is stable. During the first 18 years, the average vertical deformation rate of PS1 is 3.3 mm/y, relative to the stable parts of the building, while the deformation rate of PS2 remains 0.6 mm/y during the whole period. For PS1, a first acceleration is observed between October 2005 and June 2006. Then, in the summer of 2010, a strong acceleration occurred, up to a velocity of 15.6 mm/y and an additional 2.1 cm displacement preceding the final failure of the structure. These accelerations may be due to the breaking of clay layers and consequent transport of water and material, cf. phase C-E in Fig. 5.8. The black lines represent the average linear deformation per sensor.

which seems to be curved downward at the sinkhole location. Second, in the carboniferous layer, above the mine galleries, sandy layers were observed, which seem severely fragmented and weakened.

Based on the core drillings and the observed deformation rates from InSAR, we hypothesize that the cavity finds its origin in the partial collapse of the mine gallery, which created the fractured and fragmented area above it, see Figs. 5.8A and 5.8B. Over time, and possibly in relation to ground water dynamics, the cavity collapsed sequentially, causing it to move gradually upward. It appears plausible that the impermeable Goudsberg clay layer acted as a hydrological boundary, which curved downward with the rising cavity below, see Fig. 5.8C. Then, when the curvature became too strong, the layer fractured, causing a hydrological connection between the strata above and below and consequently transport of water and sand between these strata. We hypothesize that this may explain the sudden acceleration between 2005 and 2006. As soon as the cavity passes the clay layer, it cannot be arrested by the soft sandy strata. As a result, the cavity widens while continuing to propagate upwards, cf. Fig. 5.8D. This explains the sudden acceleration of the deformation from the InSAR data, starting summer 2010, more than one year before the collapse. Finally, Fig. 5.8E shows the occurrence of the sinkhole at the mall. In this last stage, the combination of ground water and soil transport facilitated the collapse.

5.5. Summary and conclusions

In this chapter, we set out to demonstrate the feasibility of structural health assessment of building infrastructure using radar satellite. We also demonstrated the feasibility of early detection of dynamic processes in the underground, long before they unveil themselves as surface sinkholes, with risks for life and property. Four consecutive InSAR time series from the satellites ERS-1, ERS-2, Envisat and Radarsat-2 between 1992 and 2011 detected deformation of PS over the Heerlen area, with an emphasis on shopping mall *'t Loon*. We detect localized strain within the concrete structure of the mall, exactly at the location where the construction later failed in early December 2011. The data suggest that the driving mechanism of the collapse-sinkhole must have a long lead

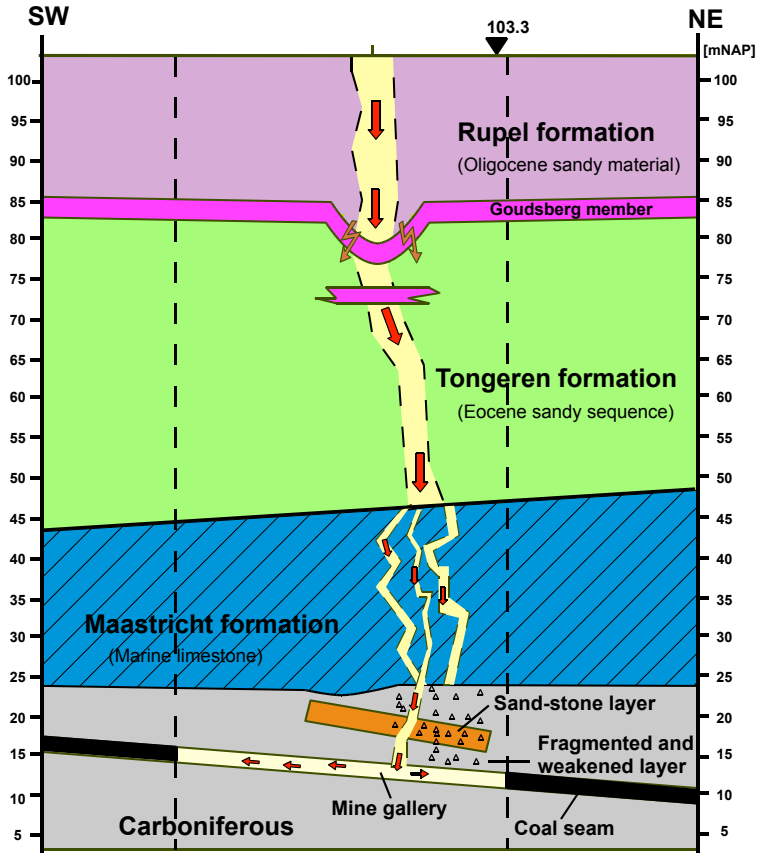

Figure 5.7: Geological profile under *'t Loon* (adapted from (Heitfeld et al., 2012)). The formation includes four main strata: from top to bottom the Rupel, Tongeren, and Maastricht formation and the carboniferous layer. The mining activities took place in the fragmented and weakened carboniferous zone below the sandstone layer. The ground height is 103.3 m w.r.t. NAP. The red arrows show possible soil movement due to the permanent seepage flow of ground water down to the mining gallery. The open black triangles indicate a mining induced fracture zone at 81 m depth.

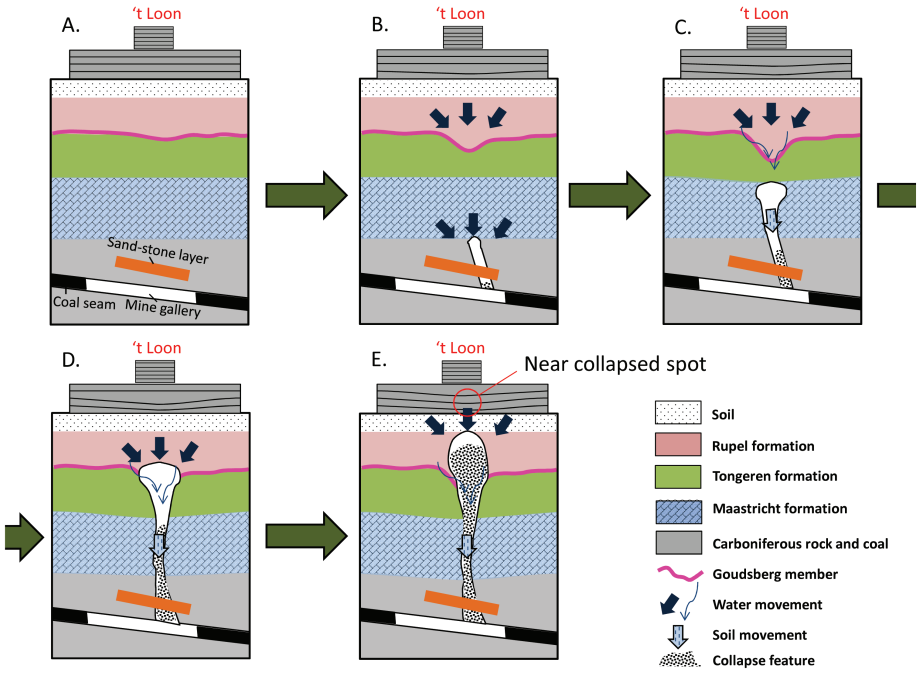

Figure 5.8: Hypothesized cavity migration sequence, suggesting a long (decadal) and gradual process after termination of the mining activities, starting with the collapse of the direct overburden (A and B) due to fractures and water movement. Elastic deformation of the layers above may occur, and hydrological units, as confined by the Goudsberg clay layer (in purple) may still be intact, (C). At shallow depths, elastic structural deformation of the building will be possible as observed by InSAR. In (D) we suggest the collapse of these hydrological confinements, corresponding with the observed accelerations, finally leading to the sinkhole at the surface (E).

time, significantly observable from the early 1990s. Two periods of accelerated deformation suggest the detectability of sudden subsurface events, such as the breaking of hydrologically confining clay layers, as in situ core drillings suggest. Therefore, given dense time-series of radar data, subsurface cavity migration may be detectable at an early stage, even when occurring beneath buildings. We suggest the implementation of automatic detection algorithms as in chapter 3, to scan radar databases over sinkhole-prone areas, typically looking for localized spatial anomalies in the deformation rates, as well as for variations in the time series.

6

Conclusions and Recommendations

The main objective of this study is to develop and demonstrate methodology to improve the capability for operational infrastructure and structural health monitoring using satellite radar interferometry. Hereby, it is assumed that the relative deformation of InSAR measurement points on a structure is a key input parameter in the assessment of its health. The study is centered around the main research question:

How to optimally assess and monitor structural health of civil infrastructure using satellite radar interferometry?

It is evident that the assessment and monitoring of all civil infrastructure on Earth will never be 'optimal' in the sense that one satellite method can yield all-encompassing and conclusive results. It is even very likely that the majority of civil infrastructure in the world will not be measurable at all, due to the lack of satellite acquisitions, an unfavorable object size and geometry, the lack of representative radar reflections, or limitations in radar resolution and revisit frequency. Yet it cannot be denied that the rapid expansion of satellite missions, improvements in resolution, revisit frequency, measurement precision, data availability and cost holds an unprecedented potential to gather information on our built environment. 'Optimality' should therefore not be assessed from the perspective of one specific object, but from a bird's eye viewpoint.

The assessment of 'structural health' of civil objects and infrastructure requires a close collaboration of different disciplines. Yet, similar to the health assessment of a human body, one cannot come to a diagnosis without observations. Furthermore, early warning (preventive) observations are preferred over observations after a critical health defect has already manifested itself. Similarly, also for structural health monitoring using observations from satellites we can distinguish *forensic analysis*, investigating the behavior of a structure after a failure manifested itself, and *preventive monitoring*, to identify anomalies in behavior that may be indicative for impending structural failure. The first application is valuable to study and recognize patterns in structural health failure, while the second aims to prevent failure by detecting structural weakness before it leads to failure.

The main research question is subdivided into four specific research questions which we will discuss subsequently.

1. *How to design the optimal functional and stochastic model?*

   We use satellite radar phase measurements to estimate kinematic parameters of points on a structure. A representative mathematical model is a prerequisite for estimating these parameters in a precise and reliable way. For infrastructure

monitoring, this mathematical model, consisting of a functional and stochastic part, should focus on the temporal behavior of points, and allow for point pairs at close distance to differ significantly. This is different from conventional InSAR/PSI processing of spatially correlated signals such as subsidence bowls, earthquakes or even volcano deformation. For infrastructure, the overall motion of the entire structure may not lead to damage, as local strain is minimal, but a local difference results in a high strain and a higher failure likelihood.

In current radar interferometric processing methods, a functional model with a minimal number of parameters is preferred (the standard steady-state model). The (implicit) stochastic model is a simple assumption of constant variance of the observations. The degree-of-fit of the data points with the functional model is then a metric to decide whether a point should be rejected as being a coherent (persistent) scatterer, or kept. Even though several authors have reported alternative models, e.g. seasonal dependent parameterizations, there was no clear framework to decide which model would be preferable, and usually all data points were analyzed with the same model. Thus, these approaches are suboptimal in their definition of the functional and stochastic model.

In chapter 3 we show how this problem can be solved. We find the optimal (most probable) functional and stochastic model (among the predefined set of hypotheses) via a systematic procedure based on multiple hypothesis testing. Starting with the null-hypothesis comprised of a steady-state functional model (which has maximum redundancy) and a scaled diagonal covariance matrix as stochastic model, we evaluate whether this null hypothesis should be rejected or not. This is applied per arc between points and the observations are double differenced in time and space. In this first implementation, it is applied as a post-processing step to the unwrapped kinematic phase data, although the approach would be applicable for wrapped (reduced) phase observations too. If the null hypothesis is not rejected, we can adjust the stochastic model to a less pessimistic and more representative quality description via the Variance Component Estimation. If the null hypothesis is rejected, we evaluate a large number of alternative hypotheses, to find the optimal functional model. The risk of overfitting the data to an unrealistically complex model is avoided via the stochastic model, which would not allow the rejection of the null hypothesis. This way we find the optimal functional model in a probabilistic way, and retrieve a characterization of the evolution of a measurement point that can be further analyzed.

As hypothesis testing methods require the a priori definition of acceptable Type-I errors (erroneous rejection of the null hypothesis) and Type-II errors (erroneous rejection of an alternative hypothesis), the proposed methodology also enables us to decide when a particular alternative hypothesis is significantly different from the null-hypothesis. This mechanism can be used by end-users of structural health assessment studies to determine at which risk level warning flags should be raised, and which level of 'false positives' is still acceptable. We conclude that a numerically efficient way for performing multiple hypothesis testing over hundreds of alternative models is able to find a most probable

functional and stochastic model for each observation point.

2. *How to detect spatio-temporal anomalies efficiently and precisely?*

   For structural health assessment, the detection of anomalies in the spatial or temporal behavior of points is probably the best indication of an (impending) problem. This, however, is not possible without defining what an anomaly is, or better, when we regard a signal as being free of anomalies. In the multiple hypothesis testing methodology presented in chapter 3, we use the steady-state null-hypothesis as the 'anomaly free' model. Hence, if the null hypothesis is not rejected, there is no (significant) anomaly in the data.

   In the library of potential kinematic models, we designed several scenarios that would be representative of an anomaly, such as the step offset (Heaviside) function in section 3.1.4 and the single outlier (Kronecker delta) model in section 3.1.5. By testing these models, subsequently for different epochs of occurrence, we can detect where and when such spatio-temporal anomalies occur. By adjusting the stochastic model under the null hypothesis, or adjusting the detection likelihood (power) of the test, we can influence the results of anomaly detection to prevent too many false positives or false negatives.

   Although not elaborated in this study, it can be stated that this approach is easily extendable from 'batch processing' for anomaly detection in hindsight, to 'recursive processing' for preventive monitoring. In the latter approach, for every new satellite data acquisition it can be evaluated whether the new observation still fits the kinematic model of the past. If it does not, warning flags can be raised, again with predefined detection likelihoods.

   This way detected spatio-temporal anomalies are a key indicator for asset management, leading to dedicated actions to avoid damage, for example by deploying more dedicated in-situ instrumentations, take appropriate maintenance or repair actions, or even evacuate hazardous locations to prevent loss of property or life in the worst case.

   We conclude that the approach presented in this study is appropriate for detecting spatio-temporal anomalies, with a priori defined precision levels (dependent on the requirements of the end user) and in a computationally efficient way.

3. *How to optimize InSAR data processing to monitor civil infrastructure?*

   As there is no single, all-encompassing method to monitor all civil infrastructure in the world, there is a need for a systematic approach to optimize the InSAR data processing method for each particular case. Experience from the various case studies performed in this study on roads, railways, bridges and buildings, shows that before starting InSAR data processing, it is important to evaluate all available prior knowledge available for the problem at hand. When more a priori knowledge is available, the first order functional (including the parameterization) and stochastic model can be defined better. This includes knowledge about the location of the study area, and the spatial and temporal extent and smoothness of the expected signal. For example, the permafrost hypothesis in

section 4.1 has an expected distinct signal that can be recognized from the data. Moreover, environmental information on land cover and atmospheric characteristics can be used to optimize the processing. In the end, all this information can be used to 'reduce' the phase, i.e., remove as much as possible of the expected phase variability, in order to facilitate parameter estimation. After this stage, the availability of satellite data should be evaluated, as this varies for different geographic locations. High-resolution, frequently acquired SAR images in X-band are preferred, from different viewing geometries. Section 4.2 on railway monitoring shows the benefits of multiple (ascending and descending) viewing geometries for estimating the various components of motion in a local, track-fixed, Cartesian right-handed coordinate system from the initial radar line-of-sight observations. Chapter 5 on building monitoring demonstrates the benefits of combining SAR data from different satellite missions to obtain a long-term data time series of structural deformation.

When the data options are known, one should choose the optimal InSAR time-series processing procedure. Typically, the persistent scatterer approaches, the small subsets of baselines (SBAS) approach, or the combination of data based on the averaging of statistically homogeneous resolution cells are are commonly used. In section 4.1 we show that for medium resolution SAR data acquired over a railway, the measurement point density can be significantly improved by averaging over statistically homogeneous points. We applied a point-selection method using an adaptive directional window filter to obtain a sufficient number of InSAR measurement points along this railway track. A dense sampling of measurement points is preferable for structural health assessment and monitoring.

By (post-)processing the results of these time series, it is important to include all possible kinematic models in the estimation procedure. Regarding the thermal component in the time series, it can be concluded that temperature-dependent corrections are to be preferred over sinusoidal fits, since temperature variability can be dominant over seasonal variability.

Several case study conclusions can be distilled from Chapters 4 and 5.

In the Qinghai-Tibet railway case (see section 4.1), we detected potential permafrost-related instabilities of the track: inhomogeneous deformations of up to 10 mm/y and seasonal displacements over a range of over 15 mm along the track. In the Betuwe railway case (see section 4.2), we converted satellite one-dimensional radar line-of-sight displacement measurements to a local, track-fixed, Cartesian right-handed coordinate system and detected the deformations in the Transversal, Longitudinal and Normal direction by using high-resolution TerraSAR-X images obtained from both ascending and descending orbits. We unveiled that track segments south of the Waalhaven and Eemhaven harbors are subject to significant vertical (normal) displacements, up to 5 cm, most likely due to settlement or compaction, during 2009 and 2013. Moreover, we also detected sudden abrupt changes in displacements along the track which suggest the existence of transition zones between free embankments and fixed substructures, such as bridges and culverts, that are subject to localized differential settle-

ment. Furthermore, we found a very high correspondence between survey train measurements and our satellite-based results, demonstrating the potential, precision, and reliability of the technology.

Applying structural health monitoring to shopping mall *'t Loon*, using a joint multi-sensor method based on the exploitation of archived medium resolution SAR data acquired by four different SAR satellite missions between April 1992 and October 2011, we detected localized strain within the concrete structure of *'t Loon*, exactly at the location where the construction later failed in early December 2011. We showed two periods of accelerated deformation which suggest the detectability of sudden subsurface events, such as the breaking of hydrologically confining clay layers, as in situ core drillings suggest. We demonstrated the feasibility of early detection of subsurface dynamic processes before they unveil themselves as surface sinkholes. Also, we concluded that the driving mechanism of the collapse-sinkhole in our case must have a long lead time, as it was significantly observable from the early 1990s.

4. *How to evaluate the quality of the obtained results?*

The quality of the obtained results can be expressed in the precision (variance-covariance, or VC-, matrix) of the estimated parameters and the internal and external reliability of the results. We showed that multiple hypotheses testing (see section 3.2) allows us to first detect model misspecifications, such as unwrapping errors, and finally adopt the most probable model per point. This testing facilitates a realistic quality description in terms of precision and reliability of the results. In the testing, the most probable functional model is built up based on a library of canonical deformation functions (see section 3.1.6), while the VC matrices of both observations and parameters can be estimated a posteriori when the parameter estimators for the most probable functional model are obtained. This posterior VC matrix of observations can be compared with an a-priori VC matrix which is predefined based on requirements, assumptions or experiments, in order to check whether the posterior stochastic model is well-determined. The estimated VC matrix of the parameters is used to check the precision of the parameters via the comparison with the criterion matrix (see section 3.5.1). Regarding the reliability of the obtained results, we introduce the *Minimal Detectable Value* (MDV) for parameter ∇, which can be used to compute the size of the errors or model misspecifications, see section 3.5.2. Since the reliability is always related to a specific alternative hypothesis, we compute the MDV, which is varying in terms of different degrees of freedom for alternative hypotheses, see sections 3.5.3 and 3.5.4.

We conclude that our testing methodology yields sound metrics to evaluate the quality of the observed results, expressed in precision and reliability. It can also be concluded that this is an important step in finding the formal error propagation procedure for InSAR time series.

6.1. Contributions

The main contributions of this study are summarized as follows,

- We introduce a stochastic model for the arc phase and describe all associated errors.
- We design and implement a probabilistic methodology of kinematic time series modeling based on multiple hypotheses testing and the B-method of testing to determine the best-fit mathematical model and identify the anomaly in time and space.
- We define a symmetric matrix L representative for every alternative hypothesis, which can be efficiently stored and retrieved in/from the RAM (random access memory) when evaluating every single point.
- We introduce the geodetic concept of reliability to InSAR estimates, defined as the ability to detect observational errors or model imperfections from the data, apart from precision.
- We introduce the Shenzhen-algorithm to estimate and mitigate the error of the reference point cased by instrumental and scattering noise.
- We detect indications of permafrost-related instabilities over the Qinghai-Tibet railway using medium-resolution SAR data.
- We find the three dimensional spatio-temporal deformation over the Betuwe railway using multi-track high resolution SAR data.
- We define the 3D coordinate transformations from the radar LOS vectors to a local, track-fixed, Cartesian right-handed coordinate system, which is dependent on the azimuth of the railway track relative to the North, the longitudinal slope of the track, and the cant of the track—which compensates for the centrifugal forces.
- We detect localized strain within the concrete structure of a building (*'t Loon*), many years before a sinkhole appeared under the building, and exactly at the location where the construction later failed in early December 2011.
- We find localized precursory displacements preceding sinkhole occurrence over the near-collapsed building *'t Loon*, using SAR data acquired by four different SAR satellite missions. We find that the long-term cavity upward migration in the abandoned mining shaft which is underneath the building, led to its near-collapse.

6.2. Recommendations

This study touched upon several issues which require to be further investigated.

High performance computing As kinematic time series contain an enormous amount of InSAR measurement points in the order of several millions, there is a need

to improve the computational efficiency and standardize the output for the end-users. In this study, we have implemented multiple hypotheses testing via single-threaded matlab codes, and demonstrated that the algorithm is efficient by using the B-method of testing. Still, the speed of data processing can be accelerated by using graphics processing unit (GPU) together with a central processing unit (CPU). GPU computing is able to process large data in a parallel way. The testing output will be formatted as a hierarchical data format, instead of a comma-separated-values format, to store and organize large amounts of numerical data.

Alternative multiple hypotheses testing approaches The most probable mathematical model of kinematic time series, for every InSAR measurement point, has been determined by multiple hypotheses testing, in the framework of the B-method of testing. However, the criterion for selecting the 'best' model, via the evaluation of test-ratios (de Heus et al., 1994), still lacks a formal proof. Moreover, other testing methods, such as the Akaike Information Criterion (Akaike, 1974, 1978), the Bayesian Information Criterion cf. (Stoica and Selen, 2004), and the P-value criterion (Murtaugh, 2014), can be used as well. These options would need to be studied in more detail.

Semi-recursive monitoring The idea of multi-epoch SAR interferometry introduced in section 2.3 is to estimate the unknown parameters and validate the quality of results when all observations have been used together in a batch processing scenario. In the practical applications, such as the monitoring of *'t Loon* in chapter 5, we are not only concerned with the historical exploitation of archived SAR data, but also interested in the possibility to predict the status during the upcoming epoch. Therefore, a dynamic data processing system is required, which is able to semi-recursively determine the solution of parameters from sequentially collected data, and recognize the anomalies in the new epoch.

High-precision positioning for InSAR measurements A major constraint in the use of satellite radar interferometry to monitoring civil infrastructure is the relatively poor geolocalization precision of the measurement points (the scatterers). This makes it difficult to attribute these measurements unambiguously to physical objects, or to elements of these objects. Even though for sensors such as TerraSAR-X, a precision of several centimeters has been reported, see Eineder et al. (2011), these results still relate to the azimuth and range position only, not to a terrestrial 3D position, and they are limited to the highly exclusive spotlight imaging mode. For a wide-scale and operational application of civil infrastructure monitoring with InSAR, medium resolution sensors such as Sentinel-1 and Radarsat-2 need to be used as well. Using advanced interferometric processing, the uncertainty of radar target positioning for those sensors will still be in the meter-range, with a highly-inclined cigar-shaped error ellipsoid with typical axis length ratios of 1/3/100 for azimuth, range, and cross-range directions (Dheenathayalan et al., 2015). Operational monitoring of, e.g., railway constructions, requires a geolocalization precision in the decimeter range, in order to determine whether the InSAR measurements stem from railway tracks, poles, embankments, or sleepers. Further research should focus on precise geolocalization and on mapping the corrected position of InSAR measurements to a 3D model of the environment.

Appendix A: Testing

During hypothesis testing, one has to define the Type-I and Type-II errors, and test the probability of correctness of the null-hypothesis against one or more alternative hypotheses, and identify the misspecifications in the mathematical model. This appendix first gives a brief overview of the types of errors in section A.1, and then separately addresses the general approaches for the observation test and the parameter significance test in section A.2 and A.3.

A.1. Error types

According to the Neyman-Pearson principle, the binary hypotheses testing problem evaluates a null hypothesis H_0 against an alternative hypothesis H_a for a one-sample test (see Fig. A.1). For the testing of such binary hypotheses, only the expectation values between H_0 and H_a are taken into account provided that the variances are known, and the conclusion of the testing is either to reject H_0 or H_a upon a certain level of significance (α is used to notate the level of significance in most literatures). There are however two possible decisions driven by the critical region K (Teunissen et al., 2005) that lead to four possible combinations including two incorrect decisions as in:

Type I error: False rejection for the null hypothesis when H_0 is true

Type II error: False acceptance for the null hypothesis when H_a is true

The probabilities of Type I and Type II errors are denoted as α and β respectively, and the probability of correct rejection of H_0 when H_a is true is known as the power of the test γ equaling to $1-\beta$. Thus,

$$\begin{aligned} \alpha &= P(\underline{\phi} \in K|H_0) = \textstyle\int_K f_{\underline{\phi}}(\phi|H_0)\,d\phi \\ \beta &= P(\underline{\phi} \notin K|H_a) = 1 - \textstyle\int_K f_{\underline{\phi}}(\phi|H_a)\,d\phi \\ \gamma &= \textstyle\int_K f_{\underline{\phi}}(\phi|H_a)\,d\phi, \end{aligned} \tag{A.1}$$

where $f_{\underline{\phi}}(\phi|H_0)$ and $f_{\underline{\phi}}(\phi|H_a)$ denote the PDF of random observable $\underline{\phi}$ under the null and alternative hypothesis, respectively. As a smaller α leads to a larger β, the ideal case when both are zero is impossible to achieve regardless of increasing the samples of data to decrease both of them at the same time. When reducing the probability of a Type I error, the consequence is an increased probability of a Type II error. A good hypothesis testing approach is to minimize both α and β by searching an optimized critical region K for test statistic $\underline{T}_q$. The test reads (Neyman and Pearson, 1933; Tiberius, 1998):

$$\begin{array}{llllll} \text{if} & T_q \in K & \text{then} & \text{reject} & H_0 \\ \text{else if} & T_q \notin K & \text{then} & \text{sustain} & H_0, \end{array} \tag{A.2}$$

where the subscript q denotes the redundancy.

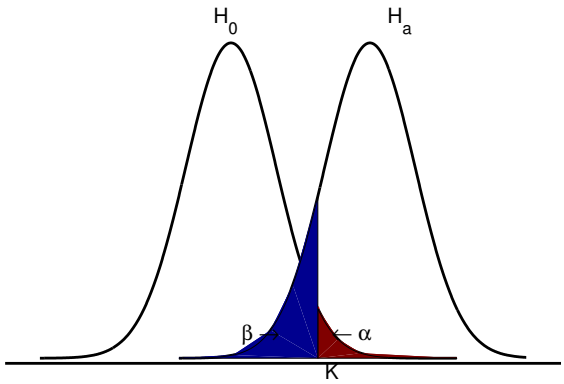

Figure A.1: The size of Type I error: α and the size of Type II error: β, for testing simple hypotheses in the case of $H_0 : x = x_0$ against $H_a : x = x_a, x_a > x_0$

A.2. Observation testing

A blunder or outlier in a single observation can be detected by an observation test when a nominal or default functional model is an appropriate description for the observables. In order to identify those observables that hold gross errors or require additional unknown parameters (see section 3.2), p. 39, the following two binary hypotheses on the expectation of $\underline{\phi}$ are given as

$$\begin{aligned} H_0 &: \quad E\{\underline{\phi}\} = Ax \\ H_a &: \quad E\{\underline{\phi}\} = Ax + C_\phi \nabla, \quad \nabla \neq 0, \end{aligned} \tag{A.3}$$

with the $m \times n$ design matrix A, the n-vector x for the unknown parameters, and the $q \times 1$ additional unknown parameters ∇ in the alternative hypothesis H_a related to the expectation of $\underline{\phi}$ by $m \times q$ specification matrix C_ϕ. Observation tests account for the unmodeled effects in vector ∇ as disturbances or blunders in the observations, not the potential relevant parameters.

Given the stochastic model of observations $D\{\underline{\phi}\} = Q_{\phi\phi}$, the test statistic is (Teunissen et al., 2005)

$$\underline{T}_q = \widehat{\underline{\nabla}}^T C_\phi^T Q_{\phi\phi}^{-1} Q_{\widehat{e}_0\widehat{e}_0} Q_{\phi\phi}^{-1} C_\phi \widehat{\underline{\nabla}}, \tag{A.4}$$

where $Q_{\widehat{e}_0\widehat{e}_0} = Q_{\phi\phi} - A(A^T Q_{\phi\phi}^{-1} A)^{-1} A^T$ ($\underline{\widehat{e}}_0$ is the residual vector between the observations and model estimations under H_0). This test statistic follows a χ^2-distribution, which is shown as

$$\begin{aligned} H_0 &: \quad \underline{T}_q \sim \chi^2(q, 0) \\ H_a &: \quad \underline{T}_q \sim \chi^2(q, \lambda), \quad \lambda \neq 0, \end{aligned} \tag{A.5}$$

where $\lambda = \nabla^T C_\phi^T Q_{\phi\phi}^{-1} Q_{\widehat{e}_0\widehat{e}_0} Q_{\phi\phi}^{-1} C_\phi \nabla$.

When the variance of unit weight σ^2 is unknown but $R_{\phi\phi}$ is given, for the stochastic model of observations $D\{\underline{\phi}\} = Q_{\phi\phi} = \sigma^2 R_{\phi\phi}$, the test statistic reads (Teunissen et al.,

2005)

$$\underline{T}_q = \frac{1}{q\underline{\widehat{\sigma}}_a^2}\underline{\widehat{\nabla}}^T C_\phi^T R_{\phi\phi}^{-1} R_{\widehat{e}_0\widehat{e}_0} R_{\phi\phi}^{-1} C_\phi \underline{\widehat{\nabla}}, \tag{A.6}$$

with $\underline{\widehat{\sigma}}_a^2 = \frac{\widehat{e}_a^T R_{\phi\phi}^{-1}\widehat{e}_a}{m-n-q}$. This test statistic is distributed as

$$\begin{aligned} H_0: &\quad \underline{T}_q \sim F(q, m-n-q, 0) \\ H_a: &\quad \underline{T}_q \sim F(q, m-n-q, \lambda), \quad \lambda \neq 0, \end{aligned} \tag{A.7}$$

where $\lambda = \frac{1}{\sigma^2}\nabla^T C_\phi^T R_{\phi\phi}^{-1} R_{\widehat{e}_0\widehat{e}_0} R_{\phi\phi}^{-1} C_\phi \nabla$.

When $q = 1$, there is only one additional unknown parameter in vector ∇, and matrix C_ϕ reduces to a vector denoted as c_ϕ. Thereby the test statistic is reduced to the $w-$test statistic and shown as

$$\underline{w} = \frac{1}{\underline{\widehat{\sigma}}_a} \frac{c_\phi^T R_{\phi\phi}^{-1}\underline{\widehat{e}_0}}{\sqrt{c_\phi^T R_{\phi\phi}^{-1} R_{\widehat{e}_0\widehat{e}_0} R_{\phi\phi}^{-1} c_\phi}}, \tag{A.8}$$

with the corresponding Student t distribution

$$\begin{aligned} H_0: &\quad \underline{w} \sim t(m-n-1, 0) \\ H_a: &\quad \underline{w} \sim t(m-n-1, \nabla w), \end{aligned} \tag{A.9}$$

where the parameter $\nabla w = \frac{1}{\sigma}\sqrt{c_\phi^T R_{\phi\phi}^{-1} R_{\widehat{e}_0\widehat{e}_0} R_{\phi\phi}^{-1} c_\phi}\nabla$ is related to the noncentrality parameter λ in Eq. (A.7), $\lambda = \nabla w^2$.

A.3. Parameter significance test

Parameter estimation and testing of statistical hypotheses consider the case that whether the functional model can appropriately describe the properties of observables. If yes, it implies that an alternative model is not needed to be applied by introducing a new parameter into the default model. This testing is put forward

$$\begin{aligned} H_0: &\quad E\{\underline{\phi}\} = Ax \quad \text{with} \quad C_x^T x = c_0 \\ H_a: &\quad E\{\underline{\phi}\} = Ax, \end{aligned} \tag{A.10}$$

where C_x represents a $n \times d$ constraint matrix and c_0 is a $d-$vector indicating the insignificant level of parameter. The rank of constraint matrix C_x equals d in which $d \leq n$. The alternative hypothesis H_a is the default model without any constraint on the parameters.

Given the stochastic model of observations $D\{\underline{\phi}\} = Q_{\phi\phi}$ and $Q_{\widehat{x}_a\widehat{x}_a} = (A^T Q_{\phi\phi}^{-1} A)^{-1}$, the test statistic is (Teunissen et al., 2005)

$$\underline{V}_d = (C_x^T \underline{\widehat{x}}_a - c_0)^T (C_x^T Q_{\widehat{x}_a\widehat{x}_a} C_x)^{-1} (C_x^T \underline{\widehat{x}}_a - c_0), \tag{A.11}$$

which follows a χ^2-distribution,

$$\begin{aligned} H_0: &\quad \underline{v}_d \sim \chi^2(d, 0) \\ H_a: &\quad \underline{v}_d \sim \chi^2(d, \lambda), \end{aligned} \tag{A.12}$$

where $\lambda = (c_a - c_0)^T (C_x^T Q_{\hat{x}_a \hat{x}_a} C_x)^{-1} (c_a - c_0)$, with $C_x^T x = c_a \neq c_0$ under H_a. Particularly, with a single constraint ($d = 1$), the test statistic becomes

$$\underline{v} = \frac{c_x^T \underline{\hat{x}}_a - c_0}{\sqrt{c_x^T Q_{\hat{x}_a \hat{x}_a} c_x}}, \tag{A.13}$$

which is distributed as

$$\begin{aligned} H_0: &\quad \underline{v}_d \sim N(0,1) \\ H_a: &\quad \underline{v}_d \sim N(\nabla v, 1), \end{aligned} \tag{A.14}$$

with $\nabla v = (c_a - c_0)/\sqrt{c_x^T Q_{\hat{x}_a \hat{x}_a} c_x}$. It is related to the noncentrality parameter $\lambda = \nabla v^2$ in Eq. (A.12).

When the variance of unit weight σ^2 is unknown but $R_{\phi\phi}$ is defined, the test statistic reads (Teunissen et al., 2005)

$$\underline{V}_d = \frac{1}{d \underline{\hat{\sigma}}_a^2} (C_x^T \underline{\hat{x}}_a - c_0)^T (C_x^T R_{\hat{x}_a \hat{x}_a} C_x)^{-1} (C_x^T \underline{\hat{x}}_a - c_0), \tag{A.15}$$

with $R_{\hat{x}_a \hat{x}_a} = (A^T R_{\phi\phi}{}^{-1} A)^{-1}$, and $\underline{\hat{\sigma}}_a^2 = \frac{\underline{\hat{e}}_a^T R_{\phi\phi}{}^{-1} \underline{\hat{e}}_a}{m-n}$, $\underline{\hat{e}}_a$ is the residual vector between the observations and model estimations under H_a. The denominator $m - n$ is the redundancy representing the difference between the number of observations m and the number of unknown parameters n. When $n = m$, the empirical variance is non-existent. This test statistic follows an F distribution,

$$\begin{aligned} H_0: &\quad \underline{V}_d \sim F(d, m-n, 0) \\ H_a: &\quad \underline{V}_d \sim F(d, m-n, \lambda), \quad \lambda \neq 0, \end{aligned} \tag{A.16}$$

where $\lambda = \frac{1}{\sigma^2} (c_a - c_0)^T (C_x^T R_{\hat{x}_a \hat{x}_a} C_x)^{-1} (c_a - c_0)$ with $C_x^T x = c_a \neq c_0$ under H_a. H_0 is rejected when $V > F_\alpha(d, m-n)$. In a special case with a single constraint vector in which $d = 1$, the test statistic becomes

$$\underline{v} = \frac{c_x^T \underline{\hat{x}}_a - c_0}{\underline{\hat{\sigma}}_a \sqrt{c_x^T R_{\hat{x}_a \hat{x}_a} c_x}}, \tag{A.17}$$

with its Student t distribution

$$\begin{aligned} H_0: &\quad \underline{v}_d \sim t(m-n, 0) \\ H_a: &\quad \underline{v}_d \sim t(m-n, \nabla v), \end{aligned} \tag{A.18}$$

with $\nabla v = (c_a - c_0)/(\sigma \sqrt{c_x^T R_{\hat{x}_a \hat{x}_a} c_x})$ which is related to the noncentrality parameter λ in Eq. (A.16), $\lambda = \nabla v^2$.

Appendix B: Seasonal periodic signal modeling

A sinusoidal function can be used for seasonal periodic signal modeling, which is generally formulated as

$$M(t) = A\sin[2\pi(t - t_0)], \tag{B.1}$$

where the observed signal M is a function of time t, for example in Julian years, t_0 is the time offset w.r.t. the master image time ($t = 0$) for InSAR case, and A is the amplitude. Empirically, the period of the sinusoidal function is assumed to be one year ($T = 1$). When $M(t = 0) = -A\sin[2\pi t_0] \neq 0$, it shows the difference of the start of the seasonal cycle with the master image, see the black curve shown in Fig. B.1, which does not agree with the assumption $M(t = 0) = 0$ for the InSAR data processing. Hence, a constant term $A\sin(2\pi t_0)$ is introduced to constrain $M(t = 0) = 0$, then Eq. (B.1) is shifted and rebuilt as

$$M(t) = A\sin[2\pi(t - t_0)] + A\sin(2\pi t_0). \tag{B.2}$$

The gray curve in Fig. B.1 indicates the rebuilt function for the InSAR case. Then to

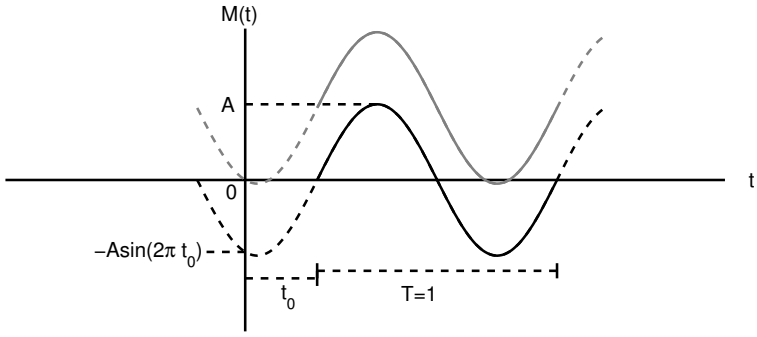

Figure B.1: Sinusoidal function

determine the two unknowns A and t_0, we expand Eq. (B.2) as follows,

$$\begin{aligned} M(t) &= A\sin[2\pi(t - t_0)] + A\sin(2\pi t_0) \\ &= A\cos(2\pi t_0)\sin(2\pi t) - A\sin(2\pi t_0)\cos(2\pi t) + A\sin(2\pi t_0) \\ &= \sin(2\pi t)\cdot(A\cos(2\pi t_0)) + (\cos(2\pi t) - 1)\cdot(-A\sin(2\pi t_0)) \\ &= \sin(2\pi t)\cdot s + (\cos(2\pi t) - 1)\cdot c, \end{aligned} \tag{B.3}$$

where the unknown coefficients s and c are linear, and $s = A\cos(2\pi t_0)$ and $c = -A\sin(2\pi t_0)$, cf. Eq. (3.4).

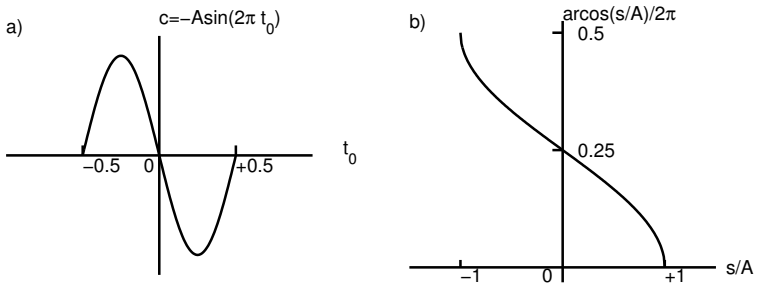

Figure B.2: Graph for a) $c = -A\sin(2\pi t_0)$ and b) $\arccos(s/A)/2\pi$

We find that

$$\begin{aligned} s^2 + c^2 &= (A\cos(2\pi t_0))^2 + (-A\sin(2\pi t_0))^2 \\ &= A^2 \cdot (\cos^2(2\pi t_0) + \sin^2(2\pi t_0)) \\ &= A^2, \end{aligned} \tag{B.4}$$

which implies that the unknown A can be derived by

$$A = \sqrt{s^2 + c^2}. \tag{B.5}$$

To compute the value of t_0, we compute it from the inverse cosine function of $\cos(2\pi t_0) = s/A$, that is

$$t_0 = -\text{sgn}(c)\arccos(s/A)/2\pi, \tag{B.6}$$

where

$$\text{sgn}(c) = \begin{cases} -1, & \text{if } c < 0 \\ 0, & \text{if } c = 0. \\ +1, & \text{if } c > 0 \end{cases}$$ Since $c = -A\sin(2\pi t_0)$, sgn(c) is dependent on t_0, it means that

$$\text{sgn}(c) = \begin{cases} -1, & \text{if } t_0 \in [0,\ +0.5] \\ 0, & \text{if } t_0 = 0 \\ +1, & \text{if } t_0 \in [-0.5,\ 0] \end{cases}$$ (see the graph for $c = -A\sin(2\pi t_0)$ in Fig. B.2a).

It is noted that the values of $\arccos(s/A)/2\pi$ are limited between 0 and 0.5 (see Fig. B.2b), which covers the half of one full cycle on the interval $t_0 \in [-0.5,\ 0.5]$, hence we multiply $\arccos(s/A)/2\pi$ by sgn(c) in order to estimate the value of t_0 when t_0 falls in [-0.5, 0].

Bibliography

Abelson, M., Baer, G., Shtivelman, V., Wachs, D., Raz, E., Crouvi, O., Kurzon, I., and Yechieli, Y. (2003). Collapse-sinkholes and radar interferometry reveal neotectonics concealed within the Dead Sea basin. *Geophysical Research Letters*, 30(10):521–524.

Abramowitz, M. and Stegun, I. A. (1970). *Handbook of Mathematical Functions*. Dover books on advanced mathematics. Dover, New York, 9 edition.

Adam, N., Eineder, M., Yague-Martinez, N., and Bamler, R. (2008). High resolution interferometric stacking with TerraSAR-X. In *Geoscience and Remote Sensing Symposium, 2008. IGARSS 2008. IEEE International*, volume 2, pages II–117. IEEE.

Adam, N., Kampes, B. M., and Eineder, M. (2004). The development of a scientific persistent scatterer system: Modifications for mixed ERS/ENVISAT time series. In *ENVISAT & ERS Symposium, Salzburg, Austria, 6–10 September, 2004*, page 9.

Akaike, H. (1974). A new look at the statistical model identification. *IEEE Transactions on Automatic Control*, 19(6):716–723.

Akaike, H. (1978). On the likelihood of a time series model. *The Statistician*, pages 217–235.

Amelung, F., Galloway, D. L., Bell, J. W., Zebker, H. A., and Laczniak, R. J. (1999). Sensing the ups and downs of Las Vegas: InSAR reveals structural control of land subsidence and aquifer-system deformation. *Geology*, 27(6):483–486.

Amelung, F., Jónsson, S., Zebker, H., and Segall, P. (2000). Widespread uplift and trap door faulting on Galápagos volcanoes observed with radar interferometry. *Nature*, 407(6807):993–996.

Amiri-Simkooei, A., Tiberius, C., and Teunissen, P. (2007). Assessment of noise in GPS coordinate time series: methodology and results. *Journal of Geophysical Research: Solid Earth (1978–2012)*, 112(B7).

An, Z., Kutzbach, J. E., Prell, W. L., and Porter, S. C. (2001). Evolution of Asian monsoons and phased uplift of the Himalaya–Tibetan plateau since Late Miocene times. *Nature*, 411(6833):62–66.

Arfken, G. (1985). *Mathematical Methods for Physicists*. Academic Press, Boston, third edition.

Arikan, M. and Hanssen, R. F. (2008). Structural deformation of the High-Speed Line (HSL) infrastructure in the Netherlands: observations using satellite radar interferometry. In 13^{th} *FIG International Symposium on Deformation Measurements and Analysis, Lisbon, Portugal, 12–15 May, 2008*, Lisbon, Portugal.

ASCE, A. S. f. C. E. (2014). 2013 report card for America's infrastructure. *ASCE website (Dec. 30, 2014)*.

Baarda, W. (1968). *A testing procedure for use in geodetic networks*, volume 5 of *Publications on Geodesy*. Netherlands Geodetic Commission, Delft, second edition.

Baarda, W. (1976). Reliability and precision of networks. In *VIIth International Course for Engineering Surveys of high precision*, pages 1–11, Darmstadt, Germany.

Baarda, W. (1977). Measures for the accuracy of geodetic networks. In *International symposium in Optimization of Design and Computation of Control Networks*, pages 1–26, Sopron, Hungary. IAG.

Baarda, W. (1979). Mathematical models. *European Organization for Experimental Photogrammetric Research*, 11:73–101.

Baarda, W. (1981). *S-Transformations and Criterion Matrices*, volume 5 of *Publications on Geodesy, New Series*. Netherlands Geodetic Commission, Delft, second edition.

Baarda, W., Commission, N. G., et al. (1967). *Statistical concepts in geodesy*, volume 2. Rijkscommissie voor Geodesie.

Baer, G., Schattner, U., Wachs, D., Sandwell, D., Wdowinski, S., and Frydman, S. (2002). The lowest place on Earth is subsiding—an InSAR (interferometric synthetic aperture radar) perspective. *Geological Society of America Bulletin*, 114(1):12–23.

Bahr, H. and Hanssen, R. (2012). Reliable estimation of orbit errors in spaceborne SAR interferometry, the network approach. *Journal of Geodesy*, 86(issue 12):1147–1164.

Bamler, R., Eineder, M., Adam, N., Zhu, X., and Gernhardt, S. (2009). Interferometric potential of high resolution spaceborne SAR. *Photogrammetrie-Fernerkundung-Geoinformation*, 2009(5):407–419.

Bamler, R. and Hanssen, R. (1997). Decorrelation induced by interpolation errors in InSAR processing. In *International Geoscience and Remote Sensing Symposium, Singapore, 3–8 Aug 1997*, pages 1710–1712.

Bamler, R. and Hartl, P. (1998). Synthetic aperture radar interferometry. *Inverse problems*, 14(4):R1–54.

Bendat, J. S. and Piersol, A. G. (1986). *Random Data: Analysis and Measurement Procedures*. Wiley-Interscience, New York, second edition.

Benn, D. I. and Lehmkuhl, F. (2000). Mass balance and equilibrium-line altitudes of glaciers in high-mountain environments. *Quaternary International*, 65:15–29.

Berardino, P., Fornaro, G., Lanari, R., and Sansosti, E. (2002). A new algorithm for surface deformation monitoring based on small baseline differential SAR interferograms. *IEEE Transactions on Geoscience and Remote Sensing*, 40(11):2375–2383.

Beres, M., Luetscher, M., and Olivier, R. (2001). Integration of ground-penetrating radar and microgravimetric methods to map shallow caves. *Journal of Applied Geophysics*, 46(4):249–262.

Bezuidenhout, C. and Enslin, J. (1970). Surface subsidence and sinkholes in the dolomitic areas of the Far West Rand, Transvaal, Republic of South Africa.

Box, G. E. P., Jenkins, G. M., and Reinsel, G. C. (1994). *Time series analysis: forecasting and control*. Prentice-Hall, Englewood Cliffs, third edition.

Brown, R. J. E. and Kupsch, W. O. (1974). *Permafrost terminology*. Number 111. National Research Council of Canada Associate Committee on Geotechnical Research. Ottawa.

Buckreuss, S., Werninghaus, R., and Pitz, W. (2009). The German satellite mission TerraSAR-X. *Aerospace and Electronic Systems Magazine, IEEE*, 24(11):4–9.

Ćakir, Z., de Chabalier, J.-B., Armijo, R., Meyer, B., Barka, A., and Peltzer, G. (2003). Coseismic and early post-seismic slip associated with the 1999 Izmit earthquake (Turkey), from SAR interferometry and tectonic field observations. *Geophysical Journal International*, 155:93–110.

Caramanna, G., Ciotoli, G., and Nisio, S. (2008). A review of natural sinkhole phenomena in Italian plain areas. *Natural Hazards*, 45(2):145–172.

Caro Cuenca, M. (2012). *Improving radar interferometry for monitoring fault-related surface deformation: Applications for the Roer valley graben and coal mine induced displacements in the southern Netherlands*. Number 81. Netherlands Geodetic Commission.

Caro Cuenca, M. and Hanssen, R. F. (2008). Subsidence and uplift at Wassenberg, Germany due to coal mining using persistent scatterer interferometry. In 13^{th} *FIG International Symposium on Deformation Measurements and Analysis, Lisbon, Portugal, 12–15 May, 2008*, Lisbon, Portugal.

Caro Cuenca, M., Hooper, A. J., and Hanssen, R. F. (2013). Surface deformation induced by water influx in the abandoned coal mines in Limburg, the Netherlands observed by satellite radar interferometry. *Journal of Applied Geophysics*, 88:1–11.

Chang, L., Dollevoet, R., and Hanssen, R. (2014). Railway infrastructure monitoring using satellite radar data. *International Journal of Railway Technology*, volume 2.

Chang, L. and Hanssen, R. (2011). Near real-time deformation monitoring based on persistent scatterer interferometry. In *International Workshop on ERS/Envisat SAR Interferometry, 'FRINGE011', Frascati, Italy, 19 Sept-23 Sept 2011*.

Chang, L. and Hanssen, R. (2012). Near real-time, semi-recursive, deformation monitoring of infrastructure using satellite radar interferometry. In *Geoscience and Remote Sensing Symposium (IGARSS), 2012 IEEE International*, pages 1876–1879. IEEE.

Chang, L. and Hanssen, R. (2015). Detection of permafrost sensitivity of the Qinghai–Tibet Railway using satellite radar interferometry. *International Journal of Remote Sensing*, 36(3):691–700.

Chang, L. and Hanssen, R. F. (2014). Detection of cavity migration and sinkhole risk using radar interferometric time series. *Remote Sensing of Environment*, 147:56–64.

Chang, P. C., Flatau, A., and Liu, S. (2003). Review paper: health monitoring of civil infrastructure. *Structural health monitoring*, 2(3):257–267.

Chen, F., Lin, H., Li, Z., Chen, Q., and Zhou, J. (2012). Interaction between permafrost and infrastructure along the Qinghai–Tibet Railway detected via jointly analysis of C-and L-band small baseline SAR interferometry. *Remote Sensing of Environment*, 123:532–540.

Cheng, G. (2003). Construction of Qinghai-Tibet Railway with cooled roadbed. *China Railway Science*, 24(3):1–4.

Cheng, G. and Wu, T. (2007). Responses of permafrost to climate change and their environmental significance, Qinghai-Tibet Plateau. *Journal of Geophysical Research: Earth Surface (2003–2012)*, 112(F2).

Cheng, P., John, W., and Zheng, W. (2002). Large structure health dynamic monitoring using GPS technology. In *FIG XXII International Congress, Washington, DC USA*.

Ching, N. H., Rosenfeld, D., and Braun, M. (1992). Two-dimensional phase unwrapping using a minimum spanning tree algorithm. *IEEE Transactions on Image Processing*, 1:355–365.

Choi, H., Choi, S., and Cha, H. (2008). Structural health monitoring system based on strain gauge enabled wireless sensor nodes. In *Networked Sensing Systems, 2008. INSS 2008. 5th International Conference on*, pages 211–214. IEEE.

Ciuc, M., Trouvé, E., Bolon, P., and Buzuloiu, V. (2002). Amplitude-driven coherence filtering in complex interferograms. In *International Geoscience and Remote Sensing Symposium, Toronto, Canada, 24–28 June 2002*.

CNN (2014). Sinkhole swallows truck in Hawaii, heavy rains force ground to give way, January 2, 2014. *CNN television*.

Coelho, B., Hölscher, P., Priest, J., Powrie, W., and Barends, F. (2011). An assessment of transition zone performance. *Proceedings of the Institution of Mechanical Engineers, Part F: Journal of Rail and Rapid Transit*, 225(2):129–139.

Coker, A., Marshall, R., and Thomson, N. (1969). Application of computer processed multispectral data to the discrimination of land collapse (sinkhole) prone areas in Florida. In *Remote Sensing of Environment, VI*, volume 1, page 65.

Colley, G. (1963). The detection of caves by gravity measurements. *Geophysical prospecting*, 11(1):1–9.

Cook, J. C. (1965). Seismic mapping of underground cavities using reflection amplitudes. *Geophysics*, 30(4):527–538.

Costantini, M. (1996). A phase unwrapping method based on network programming. In *'FRINGE 96' workshop on ERS SAR Interferometry, Zürich, Switzerland, 30 Sep–2 October 1996*.

Covello, F., Battazza, F., Coletta, A., Lopinto, E., Pietranera, L., Valentini, G., and Zoffoli, S. (2008). COSMO-SkyMed mission status. In *SPIE Remote Sensing*, pages 710918–710918. International Society for Optics and Photonics.

Crosetto, M., Monserrat, O., R., I., and B., C. (2010). Persistent Scatterer Interferometry: potential, limits and initial C- and X-band comparison. *Photogrammetric Engineering and Remote Sensing*, 76(9):1061–1069.

Curlander, J. C. and McDonough, R. N. (1991). *Synthetic aperture radar: systems and signal processing*. John Wiley & Sons, Inc, New York.

Dainty, J. C., editor (1975). *Laser Speckle and Related Phenomena*, volume 9 of *Topics in Applied Physics*. Springer-Verlag, Heidelberg.

Davenport, Jr, W. B. and Root, W. L. (1987). The Gaussian process. In *An introduction to the Theory of Random Signals and Noise*, chapter 8, pages 145–170. IEEE Press, New York.

Davis, P. J. (1970). Gamma function and related functions. In Abramowitz and Stegun (1970), chapter 6, pages 253–294.

de Heus, H. M., Joosten, P., Martens, M. H. F., and Verhoef, H. M. E. (1994). Geodetische deformatie analyse: 1d-deformatie analyse uit waterpasnetwerken. Technical Report 5, Delft University of Technology, LGR Series, Delft.

Dheenathayalan, P., Small, D., and Hanssen, R. (2014). 3D geolocation capability of medium resolution SAR sensors. In *Proceedings of the joint international geoscience and remote sensing symposium (IGARSS 2014), 35th canadian symposium on remote sensing (35th CSRS), 13-18 july 2014, Quebec, Canada*. IEEE.

Dheenathayalan, P., Small, D., Schubert, A., and Hanssen, R. F. (2015). High precision positioning of radar scatterers. *Journal of Geodesy*, submitted.

Doornbos, E. and Scharroo, R. (2004). Improved ERS and ENVISAT precise orbit determination. In *2004 ENVISAT & ERS symposium, Salzburg, Austria*.

Eineder, M. and Holzner, J. (1999). Phase unwrapping of low coherence differential interferograms. In *International Geoscience and Remote Sensing Symposium, Hamburg, Germany, 28 June–2 July 1999*.

Eineder, M., Minet, C., Steigenberger, P., Cong, X., and Fritz, T. (2011). Imaging geodesy - Toward centimeter-level ranging accuracy with TerraSAR-X. *IEEE Transactions on Geoscience and Remote Sensing*, 49(2):661–671.

Elachi, C. (1987). *Introduction To The Physics and Techniques of Remote Sensing*. John Wiley & Sons, New York, second edition.

Engelbertink, R., Morée, R., and Muis, S. (2012). Evaluatie crisisorganisatie verzakking 't Loon. Technical report, Twynstra Gudde. In Dutch.

Envisat, ASAR (2004). Envisat ASAR product handbook. *European Space*.

Esveld, C. (2001). *Modern railway track*. MRT-productions Zaltbommel, Netherlands.

Farr, T. G., Hensley, S., Rodriguez, E., Martin, J., and Kobrick, M. (1999). The shuttle radar topography mission. In *CEOS SAR Workshop, ESA-CNES, Toulouse, France, 26-29 October 1999*, pages 1–3.

Feigl, K. L., Sarti, F., Vadon, H., McClusky, S., Ergintav, S., Durand, P., Burgmann, R., Rigo, A., Massonnet, D., and Reilinger, R. (2002). Estimating slip distribution for the Izmit mainshock from coseismic GPS, ERS-1, RADARSAT and SPOT measurements. *Bulletin of the Seismological Society of America*, 92(1):138–160.

Ferretti, A., Fumagalli, A., Novali, F., Prati, C., Rocca, F., and Rucci, A. (2011). A new algorithm for processing interferometric data-stacks: SqueeSAR. *IEEE Transactions on Geoscience and Remote Sensing*, 49(9):3460–3470.

Ferretti, A., Perissin, D., Prati, C., and Rocca, F. (2005). On the physical nature of SAR permanent scatterers. In *URSI Commission F Symposium on Microwave Remote Sensing of the Earth, Oceans, Ice and Atmosphere, Ispra, Italy, 20–21 April, 2005*.

Ferretti, A., Prati, C., and Rocca, F. (1999a). Non-uniform motion monitoring using the permanent scatterers technique. In *Second International Workshop on ERS SAR Interferometry, 'FRINGE99', Liège, Belgium, 10–12 Nov 1999*, pages 1–6. ESA.

Ferretti, A., Prati, C., and Rocca, F. (1999b). Permanent scatterers in SAR interferometry. In *International Geoscience and Remote Sensing Symposium, Hamburg, Germany, 28 June–2 July 1999*, pages 1–3.

Ferretti, A., Prati, C., and Rocca, F. (2000a). Measuring subsidence with SAR interferometry: Applications of the permanent scatterers technique. In Carbognin, L., Gambolati, G., and Johnson, A. I., editors, *Land subsidence; Proceedings of the Sixth International Symposium on Land Subsidence*, volume 2, pages 67–79. CNR.

Ferretti, A., Prati, C., and Rocca, F. (2000b). Nonlinear subsidence rate estimation using permanent scatterers in differential SAR interferometry. *IEEE Transactions on Geoscience and Remote Sensing*, 38(5):2202–2212.

Ferretti, A., Prati, C., and Rocca, F. (2000c). Process for radar measurements of the movement of city areas and landsliding zones. International Application Published under the Patent Cooperation Treaty (PCT).

Ferretti, A., Prati, C., and Rocca, F. (2001). Permanent scatterers in SAR interferometry. *IEEE Transactions on Geoscience and Remote Sensing*, 39(1):8–20.

Ferretti, A., Savio, G., Barzaghi, R., Borghi, A., Musazzi, S., Novali, F., Prati, C., and Rocca, F. (2007). Submillimeter accuracy of InSAR time series: Experimental validation. *IEEE Transactions on Geoscience and Remote Sensing*, 45(5):1142–1153.

Fielding, E. J., Sladen, A., Li, Z., Avouac, J.-P., Bürgmann, R., and Ryder, I. (2013). Kinematic fault slip evolution source models of the 2008 M7. 9 Wenchuan earthquake in China from SAR interferometry, GPS and teleseismic analysis and implications for Longmen Shan tectonics. *Geophysical Journal International*.

Franceschetti, G., Iodice, A., and Riccio, D. (2002). A canonical problem in electromagnetic backscattering from buildings. *IEEE Transactions on Geoscience and Remote Sensing*, 40(8):1787–1801.

Frumkin, A. and Raz, E. (2001). Collapse and subsidence associated with salt karstification along the Dead Sea. *Carbonates and Evaporites*, 16(2):117–130.

Gabriel, A. K., Goldstein, R. M., and Zebker, H. A. (1989). Mapping small elevation changes over large areas: differential radar interferometry. *Journal of Geophysical Research*, 94(B7):9183–9191.

Galve, J., Gutiérrez, F., Lucha, P., Bonachea, J., Remondo, J., Cendrero, A., Gutiérrez, M., Gimeno, M., Pardo, G., and Sánchez, J. (2009). Sinkholes in the salt-bearing evaporite karst of the Ebro river valley upstream of Zaragoza city (NE Spain): geomorphological mapping and analysis as a basis for risk management. *Geomorphology*, 108(3):145–158.

Gatelli, F., Monti Guarnieri, A., Parizzi, F., Pasquali, P., Prati, C., and Rocca, F. (1994). The wavenumber shift in SAR interferometry. *IEEE Transactions on Geoscience and Remote Sensing*, 32(4):855–865.

Gauss, C. F. (1809). *Theoria Motus Corporum Coelestium*. Perthes und Besser, Hamburg.

Ghiglia, D. C. and Pritt, M. D. (1998). *Two-dimensional phase unwrapping: theory, algorithms, and software*. John Wiley & Sons, Inc, New York.

Ghiglia, D. C. and Romero, L. A. (1994). Robust two-dimensional weighted and unweighted phase unwrapping that uses fast transforms and iterative methods. *Journal of the Optical Society of America A.*, 11(1):107–117.

Goel, K. (2014). *Advanced Stacking Techniques and Applications in High Resolution SAR Interferometry*. PhD thesis, Technische Universität München.

Goldstein, R. M., Zebker, H. A., and Werner, C. L. (1988). Satellite radar interferometry: Two-dimensional phase unwrapping. *Radio Science*, 23(4):713–720.

Goodwillie, T. G. (2003). Calculus III: Taylor series. *Geometry & Topology*, 7(2):645–711.

Gutiérrez, F., Galve, J., Lucha, P., Bonachea, J., Jordá, L., and Jordá, R. (2009). Investigation of a large collapse sinkhole affecting a multi-storey building by means of geophysics and the trenching technique (Zaragoza city, NE Spain). *Environmental geology*, 58(5):1107–1122.

Hanssen, R. (2004). Stochastic modeling of time series radar interferometry. In *International Geoscience and Remote Sensing Symposium, Anchorage, Alaska, 20–24 September 2004*, pages cdrom, 4 pages.

Hanssen, R. and Kampes, B. (2000). On the treatment of radar interferometry in terms of geodetic adjustment and testing theory. In *International Geoscience and Remote Sensing Symposium, Honolulu, Hawaii, 24–28 July 2000*.

Hanssen, R., Riva, R., Vermeersen, B., Aoudia, K., and Sabadini, R. (2000). Coseismic deformation of the 17.8.1999, Izmit, Turkey earthquake from spherical and half-space modeling and satellite radar interferometry (SAR) imaging. In *AGU Fall meeting, San Francisco, USA*.

Hanssen, R. and van Leijen, F. (2008). On the potential of persistent scatterer interferometry for monitoring dikes in the Netherlands. 9e Nederlands Aardwetenschappelijk Congres 18-19 March, 2008, Veldhoven.

Hanssen, R. F. (2001). *Radar Interferometry: Data Interpretation and Error Analysis*. Kluwer Academic Publishers, Dordrecht.

Heitfeld, M., Schetelig, K., Klünker, J., and Paape, B. (2012). Report on geological-hydrogeological-mining settings around sinkhole at Winkelcentrum 't Loon in Heerlen/Netherlands. Technical report.

Hida, T. (1980). *Brownian motion*. Springer.

Hooper, A. (2006). *Persistent Scatterer Radar Interferometry for Crustal Deformation Studies and Modeling of Volcanic Deformation*. PhD thesis, Stanford University.

Hooper, A. (2008). A multi-temporal InSAR method incorporating both persistent scatterer and small baseline approaches. *Geophysical Research Letters*, 35(16).

Hooper, A., Segall, P., and Zebker, H. (2007). Persistent scatterer interferometric synthetic aperture radar for crustal deformation analysis, with application to Volcán Alcedo, Galápagos. *Journal of Geophysical Research*, 112(B7):B07407.

Hooper, A., Zebker, H., Segall, P., and Kampes, B. (2004). A new method for measuring deformation on volcanoes and other non-urban areas using InSAR persistent scatterers. *Geophysical Research Letters*, 31:L23611, doi:10.1029/2004GL021737.

Hordijk, D. (2012). Sinkhole at shopping center 't Loon in Heerlen. Judgment of safety and investigation in the cause. In *Adviesbureau Hageman report*, pages 7998–1–1.

Hunt, B. R. (1979). Matrix formulation of the reconstruction of phase values from phase differences. *Journal of the Optical Society of America A.*, 69(3):393–399.

Jefferys, W. H. and Berger, J. O. (1992). Ockham's razor and Bayesian analysis. *American Scientist*, pages 64–72.

Jiang, M. (2014). *InSAR Coherence Estimation and Application to Earth Observation*. PhD thesis, The Hong Kong Polytechnic University.

Jiang, M., Ding, X., Hanssen, R. F., Malhotra, R., and Chang, L. (2015). Fast statistically homogeneous pixel selection for covariance matrix estimation for multitemporal insar. *IEEE Transactions on Geoscience and Remote Sensing*, 53:1213–1224.

Jin, H.-j., Yu, Q.-h., Wang, S.-l., and Lü, L.-z. (2008). Changes in permafrost environments along the Qinghai–Tibet engineering corridor induced by anthropogenic activities and climate warming. *Cold Regions Science and Technology*, 53(3):317–333.

Just, D. and Bamler, R. (1994). Phase statistics of interferograms with applications to synthetic aperture radar. *Applied Optics*, 33(20):4361–4368.

Kampes, B. (1999). *Delft Object-Oriented Radar Interferometric Software: Users manual and Technical Documentation*. Delft University of Technology, Delft.

Kampes, B. (2005). *Displacement parameter estimation using permanent scatterer interferometry*. Forschungsbericht. DLR, Bibliotheks- und Informationswesen.

Kampes, B. and Hanssen, R. (2004a). Radar interferometric processing with Doris, cookbook. Technical report, Delft University of Technology, Delft.

Kampes, B. M. and Adam, N. (2006). The STUN algorithm for persistent scatterer interferometry. In *Fourth International Workshop on ERS/Envisat SAR Interferometry, 'FRINGE05', Frascati, Italy, 28 Nov-2 Dec 2005*.

Kampes, B. M. and Hanssen, R. F. (2004b). Ambiguity resolution for permanent scatterer interferometry. *IEEE Transactions on Geoscience and Remote Sensing*, 42(11):2446–2453.

Kaplan, W. (1952). *Advanced calculus*, volume 4. Addison-Wesley Reading, MA.

Kates, R. W., Colten, C. E., Laska, S., and Leatherman, S. P. (2006). Reconstruction of New Orleans after Hurricane Katrina: a research perspective. *Proceedings of the National Academy of Sciences*, 103(40):14653–14660.

Kenselaar, F. (1997). Model formulation and adjustment of geodetic positioning problems. Technical report, Delft University of Technology.

Ketelaar, G. (2004). Subsidence monitoring using radar interferometry. *Geomatics World Newsletter*.

Ketelaar, G., van Leijen, F., Marinkovic, P., and Hanssen, R. (2007). Multi-track PS-InSAR datum connection. In *International Geoscience and Remote Sensing Symposium, Barcelona, Spain, 23–27 July 2007*.

Ketelaar, V. B. H. (2009). *Satellite radar interferometry: Subsidence monitoring techniques*, volume 14. Springer Science & Business Media.

Koch, K.-R. (1999). *Parameter Estimation and Hypothesis Testing in Linear Models*. Springer-Verlag, New York, second edition.

Kohler, B. (2014). Dams in 26 states are getting some TLC. *The Civil Engineering Blog and News Network (Dec. 30, 2014)*.

Kohlhase, A. O., Feigl, K. L., and Massonnet, D. (2003). Applying differential InSAR to orbital dynamics: a new approach for estimating ERS trajectories. *Journal of Geodesy*, 77(9):493–502.

Kreibich, H., Thieken, A. H., Petrow, T., Müller, M., and Merz, B. (2005). Flood loss reduction of private households due to building precautionary measures–lessons learned from the Elbe flood in August 2002. *Natural Hazards and Earth System Science*, 5(1):117–126.

Krul, L. (1982). Principles of radar measurement. In *Radar calibration, Proceedings of EARSeL Workshop, Alpbach, Austria, 6–10 December 1982*, pages 11–20.

Lagios, E., Sakkas, V., Novali, F., Bellotti, F., Ferretti, A., Vlachou, K., and Dietrich, V. (2013). SqueeSAR™ and GPS ground deformation monitoring of Santorini Volcano (1992–2012): Tectonic implications. *Tectonophysics*, 594:38–59.

Lamoreaux, P. E. and Newton, J. (1986). Catastrophic subsidence: an environmental hazard, Shelby County, Alabama. *Environmental Geology and Water Sciences*, 8(1-2):25–40.

Lanari, R. (2003). Small baseline DIFSAR techniques for earth surface deformation analysis. In *Third International Workshop on ERS SAR Interferometry, 'FRINGE03', Frascati, Italy, 1-5 Dec 2003*.

Lanari, R., Berardino, P., Bonano, M., Casu, F., Manconi, A., Manunta, M., Manzo, M., Pepe, A., Pepe, S., Sansosti, E., et al. (2010). Surface displacements associated with the L'Aquila 2009 Mw 6.3 earthquake (central Italy): New evidence from SBAS-DInSAR time series analysis. *Geophysical Research Letters*, 37(20).

Lepadatu, A. and Tiberius, C. (2014). GPS for structural health monitoring–case study on the Basarab overpass cable-stayed bridge. *Journal of Applied Geodesy*, 8(1):65–86.

Lima, H. F., da Silva Vicente, R., Nogueira, R. N., Abe, I., de Brito Andre, P. S., Fernandes, C., Rodrigues, H., Varum, H., Kalinowski, H. J., Costa, A., et al. (2008). Structural health monitoring of the church of Santa Casa da Misericórdia of Aveiro using FBG sensors. *Sensors Journal, IEEE*, 8(7):1236–1242.

Linell, K. A., Tedrow, J. C., et al. (1981). *Soil and permafrost surveys in the Arctic*. Oxford University Press.

Liu, G., Jia, H., Zhang, R., Zhang, H., Jia, H., Yu, B., and Sang, M. (2011). Exploration of subsidence estimation by persistent scatterer InSAR on time series of high resolution TerraSAR-X images. *IEEE Journal of Selected Topics in Applied Earth Observations and Remote Sensing*, 4(1):159–170.

Lovse, J., Teskey, W., Lachapelle, G., and Cannon, M. (1995). Dynamic deformation monitoring of tall structure using GPS technology. *Journal of surveying engineering*, 121(1):35–40.

Ma, W., Mu, Y., Wu, Q., Sun, Z., and Liu, Y. (2011). Characteristics and mechanisms of embankment deformation along the Qinghai–Tibet Railway in permafrost regions. *Cold Regions Science and Technology*, 67(3):178–186.

Madsen, S. N. (1986). *Speckle Theory: Modelling, analysis, and applications related to Synthetic Aperture Radar Data*. PhD thesis, Technical University of Denmark.

Mahapatra, P., Samiei-Esfahany, S., and Hanssen, R. (2014). Geodetic network design for InSAR using reflectors and transponders. In *Geoscience and Remote Sensing Symposium (IGARSS), 2014 IEEE International*, pages 974–977. IEEE.

Manik, J. A., Yardley, J., and Dhaka, B. (2013). Building collapse in Bangladesh Leaves Scores Dead. *NY TIMES (Apr. 24, 2013), http://www. nytimes. com/2013/04/25/world/asia/bangladesh-buildingcollapse. html*.

Marinkovic, P., Ketelaar, G., Perski, Z., and Hanssen, R. (2006). Delft object-oriented radar interferometric software. 8ste Nederlands Aardwetenschappelijk Congres 24-25 April, 2006, Veldhoven.

Massonnet, D. and Adragna, F. (1993). A full-scale validation of radar interferometry with ERS-1: the Landers earthquake. *Earth Observation Quarterly*, 41.

Massonnet, D., Briole, P., and Arnaud, A. (1995). Deflation of Mount Etna monitored by spaceborne radar interferometry. *Nature*, 375:567–570.

Massonnet, D. and Feigl, K. L. (1998). Radar interferometry and its application to changes in the earth's surface. *Reviews of Geophysics*, 36(4):441–500.

Massonnet, D., Rossi, M., Carmona, C., Adagna, F., Peltzer, G., Feigl, K., and Rabaute, T. (1993). The displacement field of the Landers earthquake mapped by radar interferometry. *Nature*, 364(8):138–142.

Meng, M. (2013). Living a nightmare in China's city of sinkholes, july 25, 2013. *CNN television*.

Messing, F. A. M. (1988). De mijnsluiting in Limburg. Leiden, the Netherlands: Martinus nijhoff.

Miliaresis, G. C. and Argialas, D. (1999). Segmentation of physiographic features from the global digital elevation model/GTOPO30. *Computers & Geosciences*, 25(7):715–728.

Milne, I., Ritchie, R. O., and Karihaloo, B. L. (2003). *Comprehensive Structural Integrity: Cyclic loading and fatigue*, volume 4. Elsevier.

Mochales, T., Casas, A., Pueyo, E., Pueyo, O., RomRomán, M., Pocoví, A., Soriano, M., and Ansón, D. (2008). Detection of underground cavities by combining gravity, magnetic and ground penetrating radar surveys: a case study from the Zaragoza area, NE Spain. *Environmental Geology*, 53(5):1067–1077.

Mohr, J. J. and Madsen, S. N. (1996). Multi-pass interferometric for studies of glacier dynamics. In *'FRINGE 96' workshop on ERS SAR Interferometry, Zürich, Switzerland, 30 Sep–2 October 1996*. ESA.

Monserrat, O., Crosetto, M., Cuevas, M., and Crippa, B. (2011). The thermal expansion component of persistent scatterer interferometry observations. *Geoscience and Remote Sensing Letters, IEEE*, 8(5):864–868.

Montgomery, D. R., Sullivan, K., and Greenberg, H. M. (1998). Regional test of a model for shallow landsliding. *Hydrological Processes*, 12(6):943–955.

Mora, O., Lanari, R., Mallorqui, J. J., Bernadino, P., and Sansosti, E. (2002). A new algorithm for monitoring localized deformation phenomena based on small baseline differential SAR interferograms. In *International Geoscience and Remote Sensing Symposium, Toronto, Canada, 24–28 June 2002*.

Morishita, Y. and Hanssen, R. F. (2013). Deformation parameter estimation in low-coherence areas using a multi-satellite InSAR approach. In *Synthetic Aperture Radar (APSAR), 2013 Asia-Pacific Conference on*, pages 249–252. IEEE.

Morishita, Y. and Hanssen, R. F. (2015). Temporal decorrelation in L-, C-, and X-band satellite radar interferometry for pasture on drained peat soils. *IEEE Transactions on Geoscience and Remote Sensing*, 53:1096–1104.

Murtaugh, P. A. (2014). In defense of P values. *Ecology*, 95(3):611–617.

Nakamura, R., Nakamura, S., Kudo, N., and Katagiri, S. (2007). Precise orbit determination for ALOS. In *20th International symposium on space flight dynamics, Annapolis, USA*, pages 24–28.

Nassif, H. H., Gindy, M., and Davis, J. (2005). Comparison of laser Doppler vibrometer with contact sensors for monitoring bridge deflection and vibration. *NDT & E International*, 38(3):213–218.

Newton, J. G., Copeland, C. W., and Scarbrough, L. (1973). *Sinkhole problem along proposed route of Interstate Highway 459 near Greenwood, Alabama*. Geological Survey of Alabama, Division of Paleontology and Stratigraphy.

Neyman, J. and Pearson, E. (1933). On the problem of the most efficient tests of statistical hypotheses. *Philosophical Transactions of the Royal Society of London. Series A, Containing Papers of a Mathematical or Physical Character*, 231:289–337.

Nof, R. N., Baer, G., Ziv, A., Raz, E., Atzori, S., and Salvi, S. (2013). Sinkhole precursors along the Dead Sea, Israel, revealed by SAR interferometry. *Geology*, 41(9):1019–1022.

Otten, M. and Dow, J. (2004). Envisat precise orbit determination. In *2004 ENVISAT & ERS symposium, Salzburg, Austria*.

Papoulis, A. (1968). *Systems and Tronsforms with Applications in Optics*. McGraw-Hill series in Systems Science. McGraw-Hill, New York.

Parise, M. (2012). A present risk from past activities: sinkhole occurrence above underground quarries. *Carbonates and evaporites*, 27(2):109–118.

Parise, M. and Lollino, P. (2011). A preliminary analysis of failure mechanisms in karst and man-made underground caves in Southern Italy. *Geomorphology*, 134(1):132–143.

Perissin, D. (2006). *SAR super-resolution and characterization of urban targets*. PhD thesis, Politecnico di Milano, Italy.

Perski, Z., Hanssen, R., and Marinkovic, P. (2008). Deformation of the margin of Sudety mountains (Southern Poland), studied by persistent scatterers interferometry. In *Fifth International Workshop on ERS/Envisat SAR Interferometry, 'FRINGE07', Frascati, Italy, 26 Nov-30 Nov 2007*.

Pritt, M. D. (1996). Phase unwrapping by means of multigrid techniques for interferometric SAR. *IEEE Transactions on Geoscience and Remote Sensing*, 34(3):728–738.

Roberts, G. W., Meng, X., and Dodson, A. H. (2004). Integrating a global positioning system and accelerometers to monitor the deflection of bridges. *Journal of Surveying Engineering*, 130(2):65–72.

Rocca, F. (2007). Modeling interferogram stacks. *IEEE Transactions on Geoscience and Remote Sensing*, 45(10):3289–3299.

Rodriguez, E. and Martin, J. M. (1992). Theory and design of interferometric synthetic aperture radars. *IEE Proceedings-F*, 139(2):147–159.

Roest, H. (2012). Personal communication, 6 Jan 2012.

Royden, L. H., Burchfiel, B. C., and van der Hilst, R. D. (2008). The geological evolution of the Tibetan Plateau. *Science*, 321(5892):1054–1058.

Samiei-Esfahany, S. and Hanssen, R. F. (2011). Time-series InSAR: An integer least-squares approach for distributed scatterers. In *International Workshop on ERS/Envisat SAR Interferometry, 'FRINGE011', Frascati, Italy, 19 Sept-23 Sept 2011*.

Samiei-Esfahany, S., van Leijen, F. J., Marinkovic, P., Ketelaar, G., and Hanssen, R. F. (2008). Lessons learned from PSIC4: Improving PSI results for a constrained test site. In *Fifth International Workshop on ERS/Envisat SAR Interferometry, 'FRINGE07', Frascati, Italy, 26 Nov-30 Nov 2007*.

Sandwell, D. T. and Price, E. J. (1998). Phase gradient approach to stacking interferograms. *Journal of Geophysical Research*, 103(B12):30183–30204.

Sandwell, D. T. and Sichoix, L. (2000). Topographic phase recovery from stacked ERS interferometry and a low resolution digital elevation model. *Journal of Geophysical Research*, 105(B12):28211–28222.

Savage, J., Svarc, J., and Prescott, W. (2003). Near-field postseismic deformation associated with the 1992 Landers and 1999 Hector Mine, California, earthquakes. *Journal of Geophysical Research: Solid Earth (1978–2012)*, 108(B9).

Scharroo, R. and Visser, P. (1998). Precise orbit determination and gravity field improvement for the ERS satellites. *Journal of Geophysical Research*, 103(C4):8113–8127.

Schwabisch, M. and Geudtner, D. (1995). Improvement of phase and coherence map quality using azimuth prefiltering: Examples from ERS-1 and X-SAR. In *Geoscience and Remote Sensing Symposium, 1995. IGARSS'95.'Quantitative Remote Sensing for Science and Applications', International*, volume 1, pages 205–207. IEEE.

Schwäbisch, M. and Geudtner, D. (1995). Improvement of phase and coherence map quality using azimuth prefiltering: Examples from ERS-1 and X-SAR. In *International Geoscience and Remote Sensing Symposium, Florence, Italy, 10–14 July 1995*, pages 205–207.

Schwartz, J. (2013). Sinkhole swallows part of a building at a resort in Florida, August 13, 2013. *New York Times*, page A10.

Shin, T.-C. and Teng, T.-l. (2001). An overview of the 1999 Chi-Chi, Taiwan, earthquake. *Bulletin of the Seismological Society of America*, 91(5):895–913.

Sigmundsson, F., Hreinsdóttir, S., Hooper, A., Árnadóttir, T., Pedersen, R., Roberts, M. J., Óskarsson, N., Auriac, A., Decriem, J., Einarsson, P., et al. (2010). Intrusion triggering of the 2010 Eyjafjallajokull explosive eruption. *Nature*, 468(7322):426–430.

Sinclair, W. C. (1982). *Sinkhole development resulting from ground-water withdrawal in the Tampa area, Florida*. US Geological Survey, Water Resources Division.

Sousa, J. J., Ruiz, A. M., Hanssen, R. F., Perski, Z., Bastos, L., and Gil, A. J. (2008). PS-INSAR measurement of ground subsidence in Granada area (Betic Cordillera, Spain). In 13^{th} *FIG International Symposium on Deformation Measurements and Analysis, Lisbon, Portugal, 12–15 May, 2008*, Lisbon, Portugal.

Stevens, N. F., Wadge, G., and Williams, C. A. (2001). Post-emplacement lava subsidence and the accuracy of ERS IfSAR digital elevation models of volcanoes. *International Journal of Remote Sensing*, 22(5):819–828.

Stiros, S. C. and Psimoulis, P. A. (2012). Response of a historical short-span railway bridge to passing trains: 3-D deflections and dominant frequencies derived from Robotic Total Station (RTS) measurements. *Engineering Structures*, 45:362–371.

Stoica, P. and Selen, Y. (2004). Model-order selection: a review of information criterion rules. *Signal Processing Magazine, IEEE*, 21(4):36–47.

Takada, Y. and Fukushima, Y. (2013). Volcanic subsidence triggered by the 2011 Tohoku earthquake in Japan. *Nature Geoscience*, 6(8):637–641.

Teunissen, P. J. G. (1988). *Towards a Least-Squares Framework for Adjusting and Testing of both Functional and Stochastic Models*, volume 26 of *Mathematical Geodesy and Positioning series*.

Teunissen, P. J. G. (1989). Estimation in nonlinear models. In *II Hotine-Marussi Symposium on Mathematical Geodesy, Pisa, Italy, June 5–8 1989*.

Teunissen, P. J. G. (1990). Quality control in integrated navigation systems. *IEEE Aerospace and Electronic Systems Magazine*, 5(7):35–41.

Teunissen, P. J. G. (2000). *Testing theory; an introduction*. Delft University Press, Delft, first edition.

Teunissen, P. J. G. (2003). Integer aperture GNSS ambiguity resolution. *Artificial Satellites*, 38(3):79–88.

Teunissen, P. J. G. (2006). On InSAR ambiguity resolution for deformation monitoring. *Artificial Satellites*, 41(1):17–22.

Teunissen, P. J. G. and Amiri-Simkooei, A. R. (2008). Least-squares variance component estimation. *Journal of Geodesy*, 82(2):65–82.

Teunissen, P. J. G., Simons, D. G., and Tiberius, C. C. J. M. (2005). *Probability and observation theory*. Delft Institute of Earth Observation and Space Systems (DEOS), Delft University of Technology, The Netherlands.

Tiberius, C. (1998). *Recursive data processing for kinematic GPS surveying*. Number 45. Nederlandse Commissie Voor Geodesie.

Tipler, P. A. and Mosca, G. (2007). *Physics for scientists and engineers*. WH Freeman & Company.

Tizzani, P., Berardino, P., Casu, F., Euillades, P., Manzo, M., Ricciardi, G., Zeni, G., and Lanari, R. (2007). Surface deformation of Long Valley caldera and Mono Basin, California, investigated with the SBAS-InSAR approach. *Remote Sensing of Environment*, 108(3):277–289.

Tolmachev, V. and Leonenko, M. (2011). Experience in collapse risk assessment of building on covered karst landscapes in Russia. In *Karst Management*, pages 75–102. Springer.

Tough, R. J. A., Blacknell, D., and Quegan, S. (1995). A statistical description of polarimetric and interferometric synthetic aperture radar. *Proceeedings of the Royal Society London A*, 449:567–589.

Touzi, R., Lopes, A., Bruniquel, J., and Vachon, P. W. (1999). Coherence estimation for SAR imagery. *IEEE Transactions on Geoscience and Remote Sensing*, 37(1):135–149.

Usai, S., Sansosti, E., Tampellini, L., Borgstrom, S., Ricciardi, G., Spaans, J., Pepe, A., Guarino, S., Maddalena, V., van Persie, M., Berardino, P., Lanari, R., Fornaro, G., and Seifer, F. M. (2003). MINERVA: an INSAR monitoring system for volcanic hazard. *International Geoscience and Remote Sensing Symposium, Toulouse, France, 21–25 July 2003*, pages 2433–2436.

van Baars, S. (2005). The horizontal failure mechanism of the Wilnis peat dike. *Géotechnique*, 55(4):319–323.

van der Zon, N. (2013). Kwaliteitsdocument AHN2. Technical report. In Dutch.

van Everdingen, R. O. (1998). *Multi-language glossary of permafrost and related ground-ice terms in Chinese, English, French, German, Icelandic, Italian, Norwegian, Polish, Romanian, Russian, Spanish, and Swedish*. International Permafrost Association, Terminology Working Group.

van Leijen, F. and Hanssen, R. (2008). Ground water management and its consequences in Delft, the Netherlands as observed by persistent scatterer interferometry. In *Fifth International Workshop on ERS/Envisat SAR Interferometry, 'FRINGE07', Frascati, Italy, 26 Nov-30 Nov 2007*.

van Leijen, F. J. (2014). *Persistent Scatterer Interferometry based on geodetic estimation theory*. Number 86. Netherlands Geodetic Commission.

van Leijen, F. J. and Hanssen, R. F. (2007). Persistent scatterer density improvement using adaptive deformation models. In *International Geoscience and Remote Sensing Symposium, Barcelona, Spain, 23–27 July 2007*.

van Leijen, F. J., Hanssen, R. F., Marinkovic, P. S., and M, B. (2006). Spatio-temporal phase unwrapping using integer least-squares. In *Fourth International Workshop on ERS/Envisat SAR Interferometry, 'FRINGE05', Frascati, Italy, 28 Nov-2 Dec 2005*.

van Zyl, J. J. (2001). The Shuttle Radar Topography Mission (SRTM): a breakthrough in remote sensing of topography. *Acta Astronautica*, 48(5):559–565.

Varandas, J. N., Hölscher, P., and Silva, M. A. (2014). Settlement of ballasted track under traffic loading: Application to transition zones. *Proceedings of the Institution of Mechanical Engineers, Part F: Journal of Rail and Rapid Transit*, 228(3):242–259.

Verruijt, A. and Van Baars, S. (2007). *Soil mechanics*. VSSD.

Wackernagel, H. (1995). *Multivariate Geostatistics: An Introduction with Applications*. Springer-Verlag, Berlin.

Wang, S., Jin, H., Li, S., and Zhao, L. (2000). Permafrost degradation on the Qinghai-Tibet Plateau and its environmental impacts. *Permafrost and Periglacial Processes*, 11(1):43–53.

Wang, Z. (2008). A preliminary report on the great Wenchuan earthquake. *Earthquake Engineering and Engineering Vibration*, 7(2):225–234.

Weisstein, E. W. (2008). Heaviside step function. *From MathWorld–A Wolfram Web Resource. http://mathworld. wolfram. com/HeavisideStepFunction. html*.

Welk, J. E. (1997). *Railway crossing collision avoidance system*. Google Patents, US5699986 A.

Westen, J. M. J. (1971). Statistisch overzicht van productie, bezetting en prestaties van de limburgse steenkolenmijnen. *Geologie en Mijnbouw*, 50:311–320.

Wiley, C. A. (1954). Pulsed Doppler radar methods and apparatus. *United States Patent, No. 3196436*.

Wines, M. (2013). One Sinkhole Killed, and Many Others Opened, but Experts Counsel Not to Panic, March 16, 2013. *New York Times*, page A11.

Wright, T. J., Parsons, B. E., and Lu, Z. (2004). Towards mapping surface deformation in three dimensions using InSAR. *Geophysical Research Letters*, 31.

Wu, Q. and Liu, Y. (2004). Ground temperature monitoring and its recent change in Qinghai–Tibet Plateau. *Cold Regions Science and Technology*, 38(2):85–92.

Wu, Q., Liu, Y., Zhang, J., and Tong, C. (2002). A review of recent frozen soil engineering in permafrost regions along Qinghai-Tibet Highway, China. *Permafrost and Periglacial Processes*, 13(3):199–205.

Wu, Q., Zhang, T., and Liu, Y. (2012). Thermal state of the active layer and permafrost along the Qinghai-Xizang (Tibet) Railway from 2006 to 2010. *The Cryosphere*, 6(3):607–612.

Wust-Bloch, G. H. and Joswig, M. (2006). Pre-collapse identification of sinkholes in unconsolidated media at Dead Sea area by 'nanoseismic monitoring'(graphical jackknife location of weak sources by few, low-SNR records). *Geophysical Journal International*, 167(3):1220–1232.

Yoon, Y., Eineder, M., Yague-Martinez, N., and Montenbruck, O. (2009). TerraSAR-X precise trajectory estimation and quality assessment. *IEEE Transactions on Geoscience and Remote Sensing*, 47(6):1859–1868.

Yu, S., Jianming, Z., Yongzhi, L., and Jingmin, W. (2002). Thermal regime in the embankment of Qinghai–Tibetan Highway in permafrost regions. *Cold Regions Science and Technology*, 35(1):35–44.

Zebker, H., Werner, C., Rosen, P., and Hensley, S. (1994a). Accuracy of topographic maps derived from ERS-1 interferometric radar. *IEEE Transactions on Geoscience and Remote Sensing*, 32(4):823–836.

Zebker, H. A., Rosen, P. A., Goldstein, R. M., Gabriel, A., and Werner, C. L. (1994b). On the derivation of coseismic displacement fields using differential radar interferometry: The Landers earthquake. *Journal of Geophysical Research*, 99(B10):19617–19634.

Zebker, H. A. and Villasenor, J. (1992). Decorrelation in interferometric radar echoes. *IEEE Transactions on Geoscience and Remote Sensing*, 30(5):950–959.

About the author

Ling Chang was born in Jinzhong, Shanxi, China, on 13 May, 1984. She was a bachelor student at the School of Geodesy and Geomatics, Changchun Institute of Technology between September 2003 and June 2007. She graduated as an outstanding student and won the outstanding undergraduate thesis award in June 2007. From September 2007 to March 2010, she did her Master of Engineering in Geodesy and Survey Engineering at Tongji University, Shanghai. In May 2010, she won a four-year scholarship from the China Scholarship Council and was admitted to Delft University of Technology, the Netherlands, for pursuing a doctoral degree at the department of Geoscience and Remote Sensing. In September 2010, she started to work as a PhD researcher focusing on the monitoring of civil infrastructure by using satellite radar interferometry. Currently, she is working as a postdoctoral researcher on structural health monitoring of railway infrastructure at the department of Structural Engineering, Delft University of Technology.